MegaMorph – multiwavelength measurement of galaxy structure: complete Sérsic profile information from modern surveys

Boris Häußler,[1,2]* Steven P. Bamford,[1] Marina Vika,[2] Alex L. Rojas,[2] Marco Barden,[3] Lee S. Kelvin,[3,4,5] Mehmet Alpaslan,[4,5] Aaron S. G. Robotham,[4,5] Simon P. Driver,[4,5] I. K. Baldry,[6] Sarah Brough,[7] Andrew M. Hopkins,[7] Jochen Liske,[8] Robert C. Nichol,[9] Cristina. C. Popescu[10] and Richard J. Tuffs[11]

[1]*School of Physics and Astronomy, University of Nottingham, University Park, Nottingham NG7 2RD, UK*
[2]*Carnegie Mellon University in Qatar, Education City, PO Box 24866, Doha, Qatar*
[3]*Institute of Astro- and Particle Physics, University of Innsbruck, Technikerstraße 25, A-6020 Innsbruck, Austria*
[4]*School of Physics and Astronomy, University of St Andrews, North Haugh, St Andrews, Fife KY16 9SS, UK*
[5]*International Centre for Radio Astronomy Research, 7 Fairway, The University of Western Australia, Crawley, Perth, WA 6009, Australia*
[6]*Astrophysics Research Institute, Liverpool John Moores University, Twelve Quays House, Egerton Wharf, Birkenhead CH41 1LD, UK*
[7]*Australian Astronomical Observatory, PO Box 915, North Ryde, NSW 1670, Australia*
[8]*European Southern Observatory, Karl-Schwarzschild-Str. 2, D-85748 Garching, Germany*
[9]*Institute of Cosmology and Gravitation (ICG), University of Portsmouth, Dennis Sciama Building, Burnaby Road, Portsmouth PO1 3FX, UK*
[10]*Jeremiah Horrocks Institute, University of Central Lancashire, Preston PR1 2HE, UK*
[11]*Max-Planck-Institut für Kernphysik, Saupfercheckweg 1, D-69117 Heidelberg, Germany*

ABSTRACT

In this paper, we demonstrate a new method for fitting galaxy profiles which makes use of the full multiwavelength data provided by modern large optical–near-infrared imaging surveys. We present a new version of GALAPAGOS, which utilizes a recently developed multiwavelength version of GALFIT, and enables the automated measurement of wavelength-dependent Sérsic profile parameters for very large samples of galaxies. Our new technique is extensively tested to assess the reliability of both pieces of software, GALFIT and GALAPAGOS on both real $ugrizYJHK$ imaging data from the Galaxy And Mass Assembly survey and simulated data made to the same specifications. We find that fitting galaxy light profiles with multiwavelength data increases the stability and accuracy of the measured parameters, and hence produces more complete and meaningful multiwavelength photometry than has been available previously. The improvement is particularly significant for magnitudes in low-S/N bands and for structural parameters like half-light radius r_e and Sérsic index n for which a prior is used by constraining these parameters to a polynomial as a function of wavelength. This allows the fitting routines to push the magnitude of galaxies for which sensible values can be derived to fainter limits. The technique utilizes a smooth transition of galaxy parameters with wavelength, creating more physically meaningful transitions than single-band fitting and allows accurate interpolation between passbands, perfect for derivation of rest-frame values.

Key words: methods: data analysis – techniques: image processing – galaxies: fundamental parameters – galaxies: structure.

1 INTRODUCTION

Studies of galaxy formation and evolution rely on accurate estimates of physical galaxy properties, such as luminosity, mass, star formation history, size and morphology. Many of these properties are obtained from imaging data, via measurements of magnitude and profile shape. Such measurements are nowadays relatively straightforward for individual objects. However, many analyses benefit from being applied to as large a sample as possible. Given the sizes of modern surveys, this typically means thousands, or even hundreds of thousands, of galaxies. For such large numbers of measurements

*E-mail: Boris.Haeussler@nottingham.ac.uk

to be feasible, they must ideally be performed in a fully automated fashion, which significantly complicates matters.[1]

Most galaxy parameters may be obtained using a variety of methods. One common approach to measuring magnitudes is aperture photometry, in which one defines the extent of a galaxy in some manner and then sums all the flux within that area. Ideally, one would choose an aperture large enough to contain effectively all the galaxy flux. However, one cannot simply use an arbitrarily large aperture, as that would introduce excessive noise from the sky and be more likely to be contaminated by flux from neighbouring objects. Typical methods employed to define photometric apertures therefore seek a reasonable compromise. As a result, aperture magnitudes necessarily miss a proportion of flux from the outer regions of each galaxy. Furthermore, the aperture defined for a given galaxy, and hence the amount of missing flux will vary between images, depending on spatial resolution, signal-to-noise (S/N) and the exact shape of the galaxy light distribution. Colour gradients within a galaxy also lead to the inferred extent of a galaxy varying with observed wavelength (as recently reported by Kelvin et al. 2012, hereafter K12, and others). Further refinements include applying convolutions to match the point spread functions (PSFs) of the images (e.g. Hill et al. 2011), and applying a minimal correction by estimating the flux that would be missed if the galaxy were a point source (e.g. Graham et al. 2005; White et al. 2005).

Varying definitions of photometric apertures can have a significant impact on the resulting science. Using a fixed surface-brightness threshold clearly misses more flux for objects that show less compact profiles. More sophisticated methods still suffer from biases, for example Petrosian magnitudes recover essentially all the flux for exponential profiles, but miss ∼20 to ∼70 per cent of the flux (Graham et al. 2005) for de Vaucouleurs profiles (de Vaucouleurs 1948). The wavelength selected to define the aperture is also important. For example, disc galaxies are typically redder in their centre, due to the presence of a bulge or dust. Defining the aperture in a red photometric band will therefore result in total fluxes that are underestimated in bluer bands, and hence total colours that are systematically biased to redder values.

For measuring galaxy sizes, one could employ methods similar to those used to define photometric apertures. These approaches obviously suffer from many of the same issues described above, and generally do not provide a consistent, physically interpretable measure of galaxy size. A more meaningful alternative is to determine the radius (or two axes of an ellipse) that contains a specified fraction of the total galaxy light. Common examples include the half-light radius, r_{50}, and r_{90}, the radius which contains 90 per cent of the total galaxy light. Of course, these measurements depend critically on a reliable measurement of the total magnitude. Sizes derived using aperture magnitudes will suffer from systematic biases with respect to galaxy profile shape, luminosity and distance. There is again the issue of wavelength; sizes measured in blue bands will tend to reflect the extent of the young stellar populations, whereas red bands will more closely reflect the distribution of stellar mass. Just as k-corrections are required to convert observed magnitudes to rest-frame values, similar corrections may be required to homogenize sizes when considering galaxies spanning a range of redshifts. Finally, it is important to note that none of these size measurements

are corrected for the effect of the PSF. They will therefore be overestimated, particularly for intrinsically small or distant galaxies.

A variety of automated proxies for morphology have been proposed, the simplest of which focus on the shape of the azimuthally averaged surface-brightness profile. One widely used parameter is the concentration index, which is defined as the ratio of the radii containing two fractions of the total flux, e.g. $C = r_{90}/r_{50}$ (Strateva et al. 2001) or $C = 5 \cdot \log (r_{80}/r_{20})$ (as defined by CAS; Conselice 2003). All of the biases which affect these size estimates will therefore result in biases in the concentration index and similar non-parametric profile measurements. In any case, even for well-resolved, bright galaxies, such simple proxies only give a very rough indication of true internal structure or morphology.

MegaMorph is a project aimed at improving our ability to measure and understand the structure of galaxies. In particular, we endeavour to make optimal use of modern multiwavelength imaging surveys. Using data from multiple bands simultaneously in the fitting process increases the S/N, without greatly increasing the number of free parameters. Importantly, combining multiwavelength imaging provides information that is not available to techniques which operate on only a single band. For example, this enables the fitting process to utilize the different wavelength dependence of each component to help separate their profiles, and produces a more physically consistent models. We expect this to be particularly crucial when performing bulge–disk decompositions. However, in this work, we first consider only fits using single-Sérsic profiles. MegaMorph and the software developed and utilized is further discussed in Sections 1.2 and 2.

1.1 Parametric methods

To avoid many of the problems that empirical (aperture-based) methods suffer from, an increasingly popular approach to measuring galaxy properties involves fitting their surface-brightness profiles with parametric models. This has a number of advantages: all the measurements are obtained in a consistent manner, varying PSFs can be easily accommodated and the issue of missing flux is, at least partly, avoided. The price is the assumption of a parametric form for the two-dimensional surface-brightness distribution, typically exponential profiles for galaxy discs, de Vaucouleurs profiles (de Vaucouleurs 1948) for bulges and ellipticals, or more generally, Sérsic profiles (Sérsic 1968). A number of software packages have been produced to perform such fits, e.g. GALFIT (Peng et al. 2002, 2010), GIM2D (Simard 1998; Simard et al. 2002), BUDDA (de Souza, Gadotti & dos Anjos 2004), 2DPHOT (La Barbera et al. 2008) and GASPHOT (Pignatelli, Fasano & Cassata 2006).

These tools can achieve good results, both when used manually to fit individual galaxies, or when applied to large surveys in a fully- or semi-automated fashion (at least when fitting single-Sérsic models to relatively bright galaxies, e.g. Häußler et al. 2007). However, while a user of this technique can successfully employ a complex combination of profiles when fitting individual galaxies by hand (e.g. nearby NGC galaxies; Vika et al. 2012), automated model fitting in large surveys is considerably more challenging. Many thousands of galaxies, each with their own individual complications, such as neighbouring objects and potentially varying sky level, PSF, imaging availability and profile complexity, must be dealt with in an automated fashion. Developing a fully automated code with sufficient complexity, accuracy, flexibility and speed to perform profile fitting in modern surveys is difficult. Nevertheless, a number of studies (Schade, Barrientos & Lopez-Cruz 1997; Lilly et al. 1998; Allen et al. 2006; Simard et al. 2011; Tasca & White 2011; K12;

---

[1] Alternatively, for suitable tasks where automated tools are insufficient, one may instead resort to using large numbers of people, via citizen science methods, e.g., Lintott et al. (2008), with their own set of complications.

Lackner & Gunn 2012) have produced catalogues of galaxy profile parameters for large samples, with recent local studies often based on imaging provided by the Sloan Digital Sky Survey (SDSS; York et al. 2000). Some of these works focus on one-component Sérsic models, although most also attempt bulge–disc decomposition.

Many existing approaches to galaxy profile fitting are primarily designed to work with only a single image, i.e. only one photometric band. If applied to a multiband data set, each band must be fitted separately. One may choose to treat all bands equally, and allow the technique to fit a completely independent model in each band (e.g. La Barbera et al. 2010; K12) . This enables one to study wavelength-dependent structural variations, e.g. due to colour gradients. However, only a fraction of the data is used to constrain the profile in each fit. Furthermore, the resulting colours may not be physically meaningful, particularly in the case of multiple components, due to unphysical variations in the structural parameters (as demonstrated later). One might naively expect many model parameters to be identical in all bands, e.g. component centres, axial ratios and position angles, or vary smoothly with wavelength, e.g. Sérsic index and size. Alternatively, therefore, one may select one dominant band in which to fit an initial profile, and then fit this profile to the other bands while holding various parameters fixed (e.g. Lackner & Gunn 2012). With the profile fixed across all bands the resulting component colours should be more meaningful, but again only one band has been used to determine that profile, wasting data. Also consider that the smooth variation of parameters with wavelength cannot be guaranteed which this method would assume to be the case.

One approach to using all the available data to constrain the profile would be to simply sum all the images together and fit a model to the resulting image. Obviously, however, this does not allow colour information to be extracted. This profile could then be fitted to the bands individually, with the structural parameters held fixed. Another solution is to fit a model to multiple images of the same object simultaneously. This is less common than fitting single images, but not a new idea. GIM2D (Simard 1998) includes an option to fit two images with two bulge+disc models constrained to have the same structural parameters. Only the flux of each component is allowed to vary independently between the two models. This approach has been used to measure bulge and disc colours for over a million SDSS galaxies (Simard et al. 2011). GIM2D also provides an ability to fit a stack of images with identical profiles, with only the centre of the model allowed to vary between images. However, we wish to (a) make use of an arbitrary number of multiwavelength images, (b) constrain parameters to vary smoothly as a function of wavelength, being neither completely fixed or free, and (c) fit a variety of models, not just bulge+disc. We would also prefer to fit neighbouring galaxies where appropriate, rather than relying on masking (Häußler et al. 2007, hereafter H07).

To understand the desire for model parameters which vary smoothly with wavelength, consider the example of fitting a single-Sérsic model to a normal disc galaxy, comprising a blue, exponential disc and a red, de Vaucouleurs bulge. In bluer bands, the disc will be dominant, and hence the profile is best represented by a low Sérsic index, while in redder bands the bulge would become more dominant, resulting in a smoothly increasing Sérsic index with observed wavelength (K12, fig. 21). Additionally, gradients in the stellar populations within spheroids (e.g. La Barbera & de Carvalho 2009; Suh et al. 2010) and discs (e.g. Bell & de Jong 2000; MacArthur et al. 2004; Tortora et al. 2010; Gonzalez-Perez, Castander & Kauffmann 2011) and centrally concentrated dust attenuation (Driver et al. 2007; Masters et al. 2010) can produce similar effects (Möllenhoff,

Popescu & Tuffs 2006; Pastrav et al. 2012). Fixing the profile shape as a function of wavelength would therefore give bad fits in some bands. Allowing it to vary freely will often result in the parameters varying wildly with wavelength as the fit uses its increased freedom to fit the image noise. This will also significantly increase the number of parameters to be fitted.

We therefore propose that the preferred solution is to fit a full wavelength-dependent model to an arbitrary set of multiband data, simultaneously. This approach can use all the available data to define the profile, while enabling the measurement of physically meaningful component colours and colour gradients. The form of the model parameters as a function of wavelength can be chosen to optimally balance consistency and flexibility. This approach should also improve the number of galaxies for which a full set of robust photometry can be determined, as the bands can 'help each other out'. For example, in a simultaneous multiband fit, low-S/N bands would not contribute much to defining structural parameters, but would benefit from the constraints on these from higher S/N bands, resulting in robust measurements of the flux in each band.

1.2 The purpose of this paper

In MegaMorph, we have developed a combination of tools in order to test our expectations regarding the benefits of multiband parametric measurements. This software is briefly described in Section 2. Details of the implementation, together with examples illustrating the advantage of this approach, appear in Bamford et al. (in preparation, hereafter Paper I). Our technique is designed to be highly flexible, but for consistency we adopt a standard configuration for most of the work in this paper. Our choices are explained in Section 3.

This paper is accompanied by another paper (Vika et al., in preparation; Paper II), which applies our technique to a sample of 168 nearby galaxies that have been artificially redshifted in order to assess its performance in fitting individual, realistic galaxies. This paper complements that study by demonstrating the application of our technique to large surveys in an automated fashion, and with greater statistical power. Using both real and artificial images, we will demonstrate how (and why) using multiband fitting has advantages over single-band fitting, in terms of stability, improved accuracy and increased sample sizes, especially for the low-S/N bands of a survey.

Most galaxies comprise multiple structural components, primarily a bulge and a disc. The most physically meaningful parameters should therefore be obtained by fitting multicomponent models. However, fitting such models is challenging, particularly on noisy, low-resolution, single-band imaging, as the parameters of the multiple components can be highly degenerate. Using multiband data to constrain the fit significantly alleviates this problem (see Paper I), as the different wavelength dependencies of the individual components (i.e. their colours) provides valuable information, which is not present in single-band fitting.

Ultimately, we aim to decompose galaxies into physically meaningful structures, and measure reliable properties for each component. However, simpler single-component fits still provide a great deal of useful information, and are less challenging to perform. We will explore multicomponent fits in future papers, but as a first step in demonstrating the advantages of multiwavelength profile fitting, in our present work we focus on fitting single-Sérsic profiles to each object.

This paper is structured in the following way: In Section 2, we introduce the idea of multiband fitting, including a brief technical

description on how this is carried out and what changes have been applied to both GALFIT (see Section 2.1) and GALAPAGOS (see Section 2.2). Section 3 explains the setup of both codes used throughout this paper. In Section 4, we show tests from applying this software to real data from the Galaxy And Mass Assembly (GAMA) survey and compare the values to show in how much multiband fitting improves the fitting results both on individual galaxies and on the galaxy population as a whole. Section 5 carries out similar tests, but uses simulated images, e.g. galaxies whose true intrinsic values are known. This comparison, while not containing any real physical meaning about galaxy populations, allows us to show the improvement by using multiband fitting in more detail. Section 6 takes other considerations than fitting accuracy into account, e.g. fitting time and disc-space required. Finally, Section 7, both as a sanity check and to further show improvements enabled by the new technique presented in this paper, discusses the colour–magnitude diagram (CMD) of galaxies. This section is aimed to be a motivation for users to apply the software developed, tested and presented in MegaMorph papers in order to improve their scientific results.

2 MULTIWAVELENGTH PROFILE FITTING

In order to evaluate the advantages of fitting wavelength-dependent models to multiband data, we have implemented software to perform such fits. For the sake of efficiency and reliability, we chose not to re-implement all the functions required for a profile fitting code ourselves. Instead we elected to build upon existing, well-tested software and make only those changes necessary to enable multiwavelength fitting. However, in the course of modifying the software, we have also added additional features where required or deemed convenient, and generally improved the efficiency of the code where possible.

We selected GALAPAGOS (Barden et al. 2012) and GALFIT3 (Peng et al. 2010) as the starting point for our development, due to their reputation for reliability, flexibility and speed, as well as the extensive experience of members of our team in using these software tools (H07). GALFIT performs the fit for each target image while taking the image PSF into account; GALAPAGOS, after initial preparation of the data, takes care of everything else required to run GALFIT in an automated manner on a large survey, including book-keeping, object detection (using SEXTRACTOR; Bertin & Arnouts 1996), cutting images of each target, masking, determination of the sky level, estimation of initial parameters, writing setup files and load-balancing. In this section, we briefly describe our choices in implementing multiwavelength fitting, and the modifications we have made to the standard versions of these codes.

2.1 GALFITM

We have adapted GALFIT3 (Peng et al. 2010) for the requirements of this project, with permission of the original developer, C. Peng. To differentiate our modified version from the standard release, we refer to it as GALFITM. For reference, all the work in this paper uses GALFITM version 0.1.2.1. The code will be publicly released in the near future. GALFITM-0.1.2.1 is based on GALFIT version 3.0.2, although the additions in GALFIT-3.0.4 (the latest standard version) will be incorporated in GALFITM before public release. Development is continuing, primarily to improve ease-of-use and incorporate the additional features mentioned above. However, the general performance of the technique is expected to remain as presented in this paper.

GALFIT constructs model images by summing one or more components, which potentially include a sky background (with optional gradient), elliptical Sérsic functions, point sources and a variety of other profiles. GALFIT fits the parameters of its model to the input data (weighted by an error map, which may be provided or internally created) by employing the widely used Levenberg–Marquardt (LM) algorithm to minimize the weighted sum of the square residuals (χ^2). In addition to the model image itself, GALFIT calculates the derivative of the model image with respect to each free parameter, as required for the LM algorithm. The model and all of its derivatives are convolved with the provided PSF for comparison with the input image. The reader is advised to consult Peng et al. (2002, 2010) for a detailed description of GALFIT.

The standard version of GALFIT3 accepts only a single input image with which to constrain the model fit. It was therefore necessary to make fairly substantial modifications to enable the use of multiband data. However, most of the original code and its structure is maintained, and we intend our modified version to be backward compatible when used with single-band data. In this subsection, we briefly describe the significant changes. For full details, we refer the reader to Paper I.

2.1.1 Wavelength-dependent model parameters

In order for GALFITM to be able to fit multiband data, we replaced every galaxy model parameter with a wavelength-dependent function,

$$M(x, y; p_1, \ldots, p_n) \rightarrow M[x, y; \ \tilde{p}_1(\lambda; q_{1,1}, \ldots, q_{1,m_1}), \ldots, \\ \tilde{p}_n(\lambda; q_{n,1}, \ldots, q_{n,m_n})], \quad (1)$$

where $M(x, y; \cdot)$ is the model (describing the surface brightness as a function of pixel coordinate, before PSF convolution), the p_i are the n original parameters of the GALFIT3 model, and each $\tilde{p}_i$ is some function, with m_i parameters $q_{i,j}$, which describes the variation of the model parameter i versus wavelength, λ. Whereas standard GALFIT fits the p_i, in GALFITM the parameters of the fit are the set of $q_{i,j}$.

In the case of a standard Sérsic profile used in this paper, these parameters are position, magnitude, half-light radius, Sérsic index, axis ratio and position angle. However, the approach is implemented in a general fashion and works for any of the model functions provided by GALFIT3. The choice of function is somewhat arbitrary, although various properties are clearly desirable, including a straightforward way of selecting the function's flexibility and independence of the function parameters. We chose to use a series of Chebyshev polynomials (of the first kind; Abramowitz & Stegun 1965), $T_j(z)$, for all of the functions:

$$\tilde{p}_i(\lambda; \{q_{i,j}\}) = \sum_{j=0}^{m_i} q_{i,j}\, T_j[z(\lambda)]. \quad (2)$$

The Chebyshev polynomials are restricted to the domain $z \in [-1, +1]$, and hence the wavelength range of the input bands is linearly mapped on to that interval. The Chebyshev polynomial $T_j(z)$ is of the order of j, i.e. $T_2(z)$ is a quadratic function of z. Cheybshev polynomials of the first kind are defined by the recurrence relation

$$T_0(z) = 1 \\ T_1(z) = z \\ T_{n+1}(z) = 2z\, T_n(z) - T_{n-1}(z). \quad (3)$$

The fitted parameters, $q_{i,j}$, are therefore the Chebyshev coefficients of the series for parameter i.

The flexibility of this function may be varied by selecting the maximum order of each series, m_i, i.e. limiting to zeroth-order implies that a parameter must be constant with wavelength, second-order allows quadratic dependence with wavelength, while choosing the order as one less than the number of bands gives the function freedom to interpolate the data precisely.

Chebyshev polynomials form an orthogonal basis set, but full orthogonality only occurs when the function is constrained at the corresponding set of Chebyshev nodes. This is possible when approximating a smooth function, but in our case we are not free to choose the position of the constraints, they are set by the locations of the available set of photometric bands on the selected wavelength scale. Nevertheless, the independence of individual Chebyshev polynomials, even if only partial, is expected to limit the degeneracies between parameters, and hence aid the stability of the fitting process.

We stress that the purpose of the functions, $p_i(\lambda)$, is to connect the parameter values in the different bands with a user-specified degree of smoothness. For example, we might choose the Sérsic index to vary quadratically, position angle constant and magnitude to be completely free as a function of wavelength.[2] The functions themselves are not intended to be physically meaningful, although they may be used to approximate parameter values at wavelengths between the observed bands, e.g. to determine rest-frame parameters. In this paper, we use the Chebyshev polynomials as a function of wavelength. However, the variable used in the polynomials need not be true wavelength. Frequency, the logarithm of wavelength or a variety of other variables may be suitable (see Paper I for a more thorough discussion). For the purpose of this paper, we have chosen to use linear scaling with wavelength.

All of the free parameters of the model, the set of $q_{i,j}$, are fitted to all the multiband data simultaneously by minimizing a single quantity, defined as

$$\chi^2 = \sum_{u,v,w} \frac{[d_{u,v,w} - M(x_u, y_v; \lambda_w, q_{i,j})]^2}{\sigma^2_{u,v,w}} \,, \tag{4}$$

where u and v index the pixels, at positions x_u and y_u, in image d_w, with wavelength λ_w, and uncertainty image σ_w. We write equation (4) in this way to emphasize that the data comprise a set of discrete measurements, while the model M is, in principle, a continuous function, evaluated at the position and wavelength of the data in order to compute χ^2. Further technical details will be presented in Paper I.

2.1.2 Parameter constraints

One side effect of our multiwavelength modifications is that the approach taken to constrain model parameters in GALFIT3 required revision. These constraints take two forms: hardcoded limits (such as ensuring that sizes cannot become negative) and user specifiable limits, but both are treated similarly. Constraints are useful to guide the fitting process, by eliminating regions of parameter space which are ruled out by other considerations. They can therefore improve the efficiency of the early stages of the fitting process. However, if the fitting process repeatedly encounters constraints, this is an indication that a good model fit to the data cannot be achieved.

Appropriate handling of constraints is particularly important when using GALFITM to fit multiple objects simultaneously (as is common with GALAPAGOS). When considering a single galaxy (possibly with multiple components), if the fitting process ends with a parameter very close to a constraint boundary, it is reasonable to discard the resulting fit from subsequent analysis. However, in the case of a target galaxy with one or more neighbours, we would not want difficulties encountered in obtaining an unconstrained fit for a neighbouring object to negatively impact the fit to the primary target, or result in a potentially good fit to the primary target being discarded.

In GALFIT3, the physical parameters, p_i, feature directly in the fitting algorithm. Constraining these physical parameters to lie on specified intervals can therefore be achieved in a straightforward manner. At each iteration of the fitting process, the LM algorithm proposes a step for each parameter. If that step would violate a constraint, GALFIT3 typically resolves the conflict by simply setting the offending parameter to the value at the constraint boundary. For multiband fits, however, constraints on the physical parameters may be violated in some bands but not others. There is also a complicated relationship between the physical parameter at a given wavelength, $\tilde{p}_i(\lambda)$, and the fitted parameters, $q_{i,j}$. An alternative approach is therefore required. We briefly outline this here. For further details and discussion see Paper I.

The LM algorithm interpolates between the Gauss–Newton (GN) algorithm and the method of gradient descent (GD), with the degree of interpolation controlled by a damping parameter, Λ. The GN algorithm will generally attempt to make relatively large steps, whereas GD is more conservative. Increasing Λ leads to dominance of GD over GN, and increasingly smaller steps. The LM algorithm includes a prescription for varying Λ to appropriately balance GN and GD as the fit progresses: if a proposed set of parameter steps successfully improves χ^2, then Λ is decreased by a factor, and the steps are accepted; otherwise it is increased by the same factor, and the steps are rejected. (This factor is 10 in the case of GALFIT.)

In GALFITM, if a proposed set of steps in the fitting parameters $q_{i,j}$ would violate a constraint on the standard parameter p_i in any of the wavelength bands, then the steps are not performed for parameters $q_{i,\cdot}$. All other (unoffending) parameters are stepped as usual and a trial value of χ^2 generated. This approach avoids the difficulty of determining how to limit the parameters $q_{i,\cdot}$ so as to avoid the resulting $\tilde{p}_i(\lambda; \{q_{i,\cdot}\})$ from violating any constraints at the wavelengths of the input bands.

For a moment assume that this is the only change. In that case a failure to improve χ^2 would result in a decrease in Λ, and rejection of the entire proposed set of parameter steps. The steps in the next proposed set would be smaller, and more likely, though far from guaranteed, to avoid violating constraints. However, often the proposed steps (without those which would cause violated constraints) will result in an improved χ^2, an acceptance of those steps and an increase in Λ. The next iteration is therefore likely to propose a step in the offending standard parameter that is similar to, or larger than, the previous. Tests have shown that this often results in that parameter remaining fixed for the entire duration of the fit, even though a small movement towards the constraint may lower χ^2 and result in a more acceptable model.

To mitigate this issue, and encourage movement of constraint-violating parameters towards (but not beyond) constraint limits, we impose a schedule for Λ. This is designed to substantially increase Λ occasionally in the case of violated constraints, resulting in the next set of proposed steps being much smaller than the previous proposal, and so more likely to avoid overstepping the constraint boundary.

---

[2] To be exact, we use 3543 Å, 4770 Å, 6231 Å, 7625 Å, 9134 Å, 10305 Å, 12483 Å, 16313 Å, 22010 Å for *ugrizYJHK* band, respectively.

This adopted schedule was developed through trial and error, but appears to do a reasonable job of meeting our requirements.

The result is that constraints can be specified in GALFITM, on both individual fitting parameters, $q_{i,j}$, and more usefully on the standard parameters, p_i, at any, or all, of the input band wavelengths. For example, in the fits in this paper the Sérsic index, n, is constrained to lie on the interval $0.2 \leq n \leq 8$ at all input wavelengths. Details of all the constraints applied in this work are given in Section 3.

2.1.3 Other modifications

While making the changes described above, we have attempted to retain backward compatibility as far as possible. While the setup is, of course, slightly more complicated for multiband data, we ensure for any original GALFIT3 start file (for single-band data) to work unaltered with GALFITM. The additional multiwavelength features are simple to enable, and any user already familiar with GALFIT should have no difficulties using GALFITM.

The output format of GALFITM is also slightly modified. In addition to the image, model and residual (which of course GALFITM provides for each band), for convenience it also stores the PSFs used and provides all the fitting information, including setup details and the full results, in FITS tables within the output file. Information is also still provided via header keywords for backward compatibility.

Several minor fixes and efficiency improvements have also been made. For example, all variables are now stored as double precision. Besides being more accurate, this also provides a modest speed improvement on modern 64-bit machines. Again, we refer interested readers to Paper I for full details of our GALFIT modifications.

As part of our MegaMorph project, we are investigating several other modifications to GALFIT, including the incorporation of non-parametric components, and alternatives to the LM algorithm. The results of these investigations will be described in future papers.

Throughout the development of GALFITM, we have compared its output on single-band data to that of GALFIT3, generally finding very close agreement. For the vast majority of galaxies, the results of GALFITM and GALFIT3 are identical. The greatest differences relate to our modified implementation of constraints. In cases where constraints are encountered during the fit, this can result in somewhat slower convergence, but this is often accompanied by a formally better fit, in terms of a slightly reduced χ^2 compared with GALFIT3.

2.2 GALAPAGOS

We have adapted the current public version of the IDL script GALAPAGOS (version 1.0) to support GALFITM, and hence utilize multiwavelength data, in close collaboration with its original developer, and coauthor of this paper, M. Barden. In the process, we have implemented a number of improvements and additional features, some for efficiency or convenience, and others that were required by the nature of our chosen data set. We refer to our new version as GALAPAGOS-2. Specifically, version 2.0.2 was used to produce most of the results shown in this paper. Section 7 uses version 2.0.3, but the two versions only differ in very minor details and should produce nearly identical fitting results. Changes became necessary in order to be able to target specific objects instead of every object that was detected, hence speeding up the analysis for Section 7, where only a subset of the detected objects are considered. In all versions of the code, we have attempted to preserve backward compatibility in the case of single-band data. The code will be publicly released in the near future. In this subsection, we will briefly explain our modifications.

Prior to this work, GALAPAGOS was designed for use with space-based imaging, specifically for surveys performed by the *Hubble Space Telescope* (*HST*). The *HST* PSF is very stable on the multidrizzled images that are usually used for fitting purposes, both temporally and across the field of view. GALAPAGOS-1 therefore only used one PSF for the entire survey. For the MegaMorph project, we wished to apply GALAPAGOS to ground-based imaging. While it is possible to approximately homogenize the PSF across an entire survey, by applying appropriate convolutions, the resulting resolution must necessarily correspond to the worst case and thus a great deal of spatial information would be discarded. Instead, we adapted GALAPAGOS to work with a spatially variable PSF.

In principle, it would be desirable for GALAPAGOS to construct an estimated PSF for each target galaxy (as was done in K12). However, this would require providing GALAPAGOS with knowledge of the survey strategy. As each survey will typically adopt a different tiling strategy, PSF creation is not trivial to generalize, particularly given the importance of the PSF in correctly modelling galaxy profiles. Sophisticated software already exists to take a set of point sources and combine them to produce an accurate PSF (e.g. PSFEX[3]) and a user of our code should use those to pre-determine a set of suitable PSFs. For the GAMA survey, PSFs had already been determined by K12 and were used throughout this analysis.

For generality, we implemented a selection of the PSF from a provided list of filenames and sky coordinates. GALAPAGOS simply selects the closest PSF to each target position. As K12 generate PSFs at the position of each galaxy with $m_r < 19.8$, the PSFs will correspond exactly for these galaxies, and the sampling is sufficiently dense that, in the vast majority of cases, fainter galaxies will be well represented by their nearest PSF. The PSF selection is performed for each band individually.

We ultimately aim for our technique to be applicable to the largest surveys available. During this proof-of-concept stage we are content to restrict ourselves to more modest data sets, but still wished to work with a single GAMA II region, of area $\sim 60 \deg^2$. We therefore improved the efficiency of the code in several places where it became apparent that, for large data sets such as ours, a major speedup was possible. Some of these changes may alter the outcome of the code very slightly (e.g. sub-scripts of GALAPAGOS now know only about the neighbouring frames at times, instead of the entire survey, potentially changing deblending decisions). However, we think that in practice this will not produce any significant differences in the results, as we were always very conservative in our modifications. Overall, we were able to speed up the code by approximately a factor of 4 in terms of CPU time. A further simple optimization was made in the loop over all objects in the survey. GALAPAGOS-1 determines whether the next object in queue is close enough to be influenced by an object currently being processed, and, if so, waits for that object to finish before starting the next. Our new code simply continues with a different object further away, thus keeping more CPUs busy at any given time.

Most importantly, of course, the code can now handle multiwavelength data sets. In addition to defining all the bands, each comprising a set of images, which are to be used for fitting (using a setup similar to GALAPAGOS-1), the user must define an additional set of images on which SEXTRACTOR is run for object detection. Of course, the detection images could simply correspond to one of the fitting bands. In our case, we chose to use a co-added image of all bands for detection, in order to detect sources with extreme colours

---

[3] http://www.astromatic.net/software/psfex

that would be missed if only one band were used for detection. In this way, we use the whole data set in order to derive an object list. Even so, the fitting bands are not all quite equal: one must be defined as the primary band, on which all deblending and masking decisions are made. We chose the *r* band in our data set, because it typically has the highest S/N. Our construction of the multiband detection image is very simple, and could admittedly be improved upon by weighting the input images more carefully (e.g. Szalay, Connolly & Szokoly 1999). Nevertheless, it suffices for the purposes of this paper.

The output returned by GALAPAGOS-2 provides much more information than previously, namely most of the details from the FITS tables in the GALFITM output file. However, GALAPAGOS-2 may continue to be used with GALFIT3, for single-band data, in which case it provides the same information as the previous version.

Further planned changes include the implementation of bulge–disc decomposition, ideally together with model selection, so that GALAPAGOS itself is able to decide whether a single-profile fit or bulge–disc decomposition provides the better representation of the imaging for each object and hence the more useful set of parameters. We also plan to adapt GALAPAGOS to run in supercomputing environments, in order to achieve the speed necessary for larger samples and/or surveys. However, the general performance of single-Sérsic profile fitting is expected to remain as presented in this paper.

3 CHOICE OF MULTIWAVELENGTH MODEL, INITIAL PARAMETER VALUES AND CONSTRAINTS

GALAPAGOS requires various choices to be made regarding its operation and the setup information it provides to GALFIT. Our generalization to multiband data adds a number of additional options. This section describes the choices we have made for the analysis described in this paper.

If GALFITM is used to fit a single-component profile with structural parameters (i.e. all except magnitude) that are constant with wavelength, this is mostly equivalent to using GALFIT3 to first fit a single co-added image to obtain these parameters, and then measuring each magnitude by fitting each band with this fixed profile. When using multiple-component profiles, this is no longer true, and retaining the multiband information throughout the fit leads to more accurate and reliable measurements (see Paper I). In the case of single-component fits, the greatest advantage of our new fitting technique comes from allowing profile structural parameters to vary systematically with wavelength; the use of co-added images would lose this information. We will quantify the benefit of our multiband fitting approach in Section 5. An important set of choices are therefore the degree of wavelength dependence we allow for each parameter.

It is critical that we obtain an accurate magnitude for each band, and hence colours. The magnitudes in each band are clearly correlated, and the variety of possible galaxy spectral energy distributions (SEDs) are very well known. These cannot be reproduced with a low-order polynomial, and so we must ensure that sufficient freedom is given to the magnitudes such that they are accurately recovered. Full freedom is implied by using a polynomial with as many coefficients as data points, in which case the function is capable of perfectly interpolating the data. To describe the wavelength dependence of magnitude, we therefore use an eighth-order polynomial (with nine free coefficients, equal to the number of bands in our data set). Note that the use of high-order interpolating polynomials is afflicted by Runge's phenomenon, whereby the function

oscillates excessively between data points, particularly at the edges of the considered interval. The entire function itself therefore does not well represent the galaxy SED and so cannot be used to estimate magnitudes at wavelengths other than those for which there are constraining data (see Section 5.2). However, the magnitudes obtained for each band in the data set remain reliable. If required, e.g. for *k*-correcting magnitudes, the resulting magnitudes may be interpolated using different codes, based on realistic SED templates (e.g. KCORRECT; Blanton & Roweis 2007). Finally, note that while we allow full freedom for magnitudes in this paper, in further work it may be appropriate to consider using slightly lower order polynomials to reduce this issue, while still retaining sufficient flexibility to recover accurate values (see Paper I).

Equally important to accurate magnitudes is the determination of physically meaningful structural parameters of the galaxies, e.g. half-light radius and Sérsic index. We chose to allow profile half-light radius and Sérsic index to vary with wavelength quadratically (i.e. second-order polynomials, with three coefficients). This was decided after examining the wavelength dependence of these quantities from single-band fits to bright galaxies. For most of these a linear function was sufficient to model the trend, but in some cases a mild curvature was seen. We therefore elected to fit a polynomial one order higher than linear, in order to examine this effect.

In our simulations (described in Section 5), we create simulated galaxies for which half-light radius and Sérsic index vary according to known second-order functions. When fitting these simulations, we allow these parameters to vary with third order, in order to investigate our ability to recover the correct higher order coefficients.

As the images for each wavelength band are accurately registered (although read K12 and Section 4.1), the centre of the profile is constant with wavelength (although the centre is allowed to vary during the fit; we do not constrain the position to that given by SEXTRACTOR). Similarly, for position angle and axis ratio we also choose to fit constant values, with no wavelength dependence. While this ignores variations that might be expected for typical spiral galaxies (red bulges are round, blue discs appear elongated), this seemed to be a reasonable approximation for our purposes in this paper.

The sky values for each band are pre-determined by GALAPAGOS and held fixed during the fit.[4] We have shown in H07 that this is the most reliable approach for single-band fits, and there is no obvious reason why this should not also be the case when using multiband data.

Largely following H07, we adopt the following constraints on the parameters in GALFITM. In the case of multiband fitting, these constraints apply to the parameter values for all bands (but not the entire polynomial).

Position (*x*, *y*): These are simply constrained to lie within the image cut-out for this object. In practice, this constraint is rarely encountered during the fit, but is retained to prevent the centre running out of the image in the case of a nearby bright source.

Magnitude (*m*): $-5 \leq m_{fit} - m_{input} \leq 5$, where m_{input} is derived by adding an empirically estimated offset to the `Mag_Best` derived by SEXTRACTOR during object detection. Additionally, we use

---

[4] At this point, it should be mentioned that the GAMA data show imperfect flat-fielding of the provided SWARPed images due to the use of large filters. These are chosen to avoid removing too much real local structure but lead to sky backgrounds not being accurately measured around small objects. As this effect would be present in both single- and multiband fitting, we ignore this effect in this paper.

$0 \leq m \leq 40$, to ensure sensible values; in practice this constraint is rarely hit.

Size (half-light radius; r_e): $0.3 \leq r_e \leq 400$ pixels. This maintains values in a physically meaningful range and prevents the code from fitting very small sizes, where, due to oversampling issues, the fitting iterations become very slow. Pixel sizes in the data used are 0.339 arcsec pixel^{-1}, hence we constrain the half-light radii to be $r_e \gtrsim 0.1$ arcsec. For reference, it should be noted that $r_e \gtrsim 0.1$ arcsec corresponds to $r_e \sim 0.3$ kpc at a typical object redshift of $z \sim 0.2$ in the GAMA survey.

Sérsic index (n): $0.2 \leq n \leq 8$. Fits with values outside these ranges rarely represent good models of a target galaxy. The upper value of 8 is a conservative choice as objects with higher Sérsic indices are rarely seen and, from earlier visual inspection, are usually associated with spurious galaxy fits or cases where the target object is a star. It should be stated that some luminous elliptical galaxies with $n > 8$ do exist (e,g, Graham et al. 2005), hence this constraint will be removed and loosened to higher values in future works.

Axis ratio (q): $0.0001 \leq q \leq 1$. Again, this ensures that the fitted value is physically meaningful, but is mostly superfluous, as GALFIT includes a hardcoded constraint on $0 \leq q \leq 1$. The main reason for this constraint being applied is that GALFIT when very small values are reached becomes very slow due to oversampling issues.

Position angle (θ): $-180° < \theta < 180°$. This constraint is hardcoded in GALFIT. Following the same definition as GALFIT, position angle defined as a major axis positioned vertically is $0°$ (nominally north if rotated to the standard orientation) and increases counterclockwise (nominally towards the east).

These constraints are implemented in order to improve and speed up the fitting process when fitting galaxies. For stars, the situation is slightly different. An unsaturated star should technically return a point source when PSF-correction is used during the fit, i.e. $r_e = 0$. However, for practical reasons, enforced by the constraints specified above, the fit is not allowed to do this. Instead, the fit results usually end up on one of these fitting constraints (typically $r_e = 0.3$[pix] and $n = 8$) and thus removes the star from the image in a slightly non-optimal way. However, when this model is subtracted from the image after PSF convolution, we generally find these constraints produce a reasonable residual image, thus not significantly influencing the galaxy fits. For saturated stars, fitting a Sérsic fitting, while masking out the saturated part of the profile, is more suitable to remove the wings of the profiles, more important in order to improve the fit of the neighbouring galaxies.

We use these constraints to remove both stars and galaxies with bad fits, from our catalogue, by identifying objects with fit results lying on one or more constraint boundaries. As just explained, the vast majority of stars result in values on one of the above constraints. This also occurs for galaxies when the object in question cannot sensibly be fitted with a Sérsic profile, and hence any returned values should not be used in a scientific context. Please read Section 4.2 for more details about the cleaning of the fitting results catalogue.

One obvious potential improvement would be to fit stars with PSF profiles (as has been done in K12) instead of Sérsic profiles. GALFIT generally does allow this, but there are two main reasons why we have chosen not to do this. First, such a procedure would require a reliable galaxy/star classifier, to make the decision of which profile to use for each object. While this feature is desirable, it is not straightforward to implement, and was not deemed to be high priority, given the low impact we expect it to have on our results. Secondly, there are bright stars present in the images, which possess significant flux at radii beyond the size of the PSF images

we use. This is especially true for very bright, highly saturated stars, for which the profile core strongly deviates from the PSF due to saturation effects. Furthermore, the wings of bright stars often vary, and are therefore not well represented by an averaged PSF. In these worst cases, it was found that fitting a Sérsic profile, rather than a PSF, results in much better residual images, particularly at large radii, as it has more flexibility to mimic and remove the outer wings of the PSF profile. In our data setup, we additionally use a masking scheme to identify saturated areas in the image. These areas are consequently (a) smoothed in the SEXTRACTOR detection image, such that star images with the internal structure typical of saturated sources in SDSS are detected as one object only and (b) masked in the images used by GALFIT, hence sufficiently removing the wings of the stars and masking out the innermost areas, so a fit to a neighbouring source should not be significantly influenced by either of these areas.

4 APPLICATION TO REAL IMAGING

We evaluate our multiband galaxy profile fitting technique on both real and simulated data sets. Our real data obviously have the advantage of showing actual galaxies, and we can compare to results from other studies. However, there is no definitive 'truth' to which we can compare. Simulated data, on the other hand, are idealized and do not capture all the subtleties of real data, and of course cannot be used to study the real Universe. However, they do provide us with a way of testing the results of our method against known values. We first present our work using the real data set.

In this section, we describe the data, and show the results of extensive tests and comparisons between single-band and multiband fitting techniques, using an otherwise identical code.

4.1 Data

For the purpose of these tests, we have chosen to use imaging data provided by the GAMA survey (Driver et al. 2011), as it comprises one of the largest multiwavelength data sets currently available, in terms of both area and wavelength. GAMA is focused around a redshift survey, but, crucially, this is supplemented by a highly homogeneous and complete set of multiwavelength data, spanning from the far-UV to radio, making it a superb tool for studying the local Universe. We plan to use the galaxy profile fits from this paper and future work to perform a variety of scientific studies for which the wealth of the GAMA data set is extremely valuable.

The present GAMA survey (phase I) covers an area of $\sim$144 deg^2, of which half is in three $\sim$48 deg^2 equatorial fields, with high spectroscopic completeness to a depth of $r < 19.4$. Current efforts (GAMA II) are focused on two additional, more southerly, fields as well as expanding the equatorial fields to $\sim$60 deg^2, increasing the depth of all fields to $r < 19.8$ and the total survey area to $\sim$290 deg^2. As we only require a relatively modest sample size for the purposes of this paper ($\sim$10^4 galaxies), and because of the computing time required to fit large samples, in this paper we limit ourselves to one region of GAMA, the equatorial field at 9 h RA, and often to only a subregion of that. In future work, we will expand our analysis to the full GAMA II survey.

GAMA has prepared its imaging data in a very convenient form for our purposes (Hill et al. 2011). These data include five-band optical (*ugriz*) imaging from SDSS plus four-band near-infrared (*YJHK*) imaging from the Large Area Survey component of the UKIRT Infrared Deep Sky Survey (Lawrence et al. 2007). All of these bands have a depth and resolution amenable to Sérsic-profile
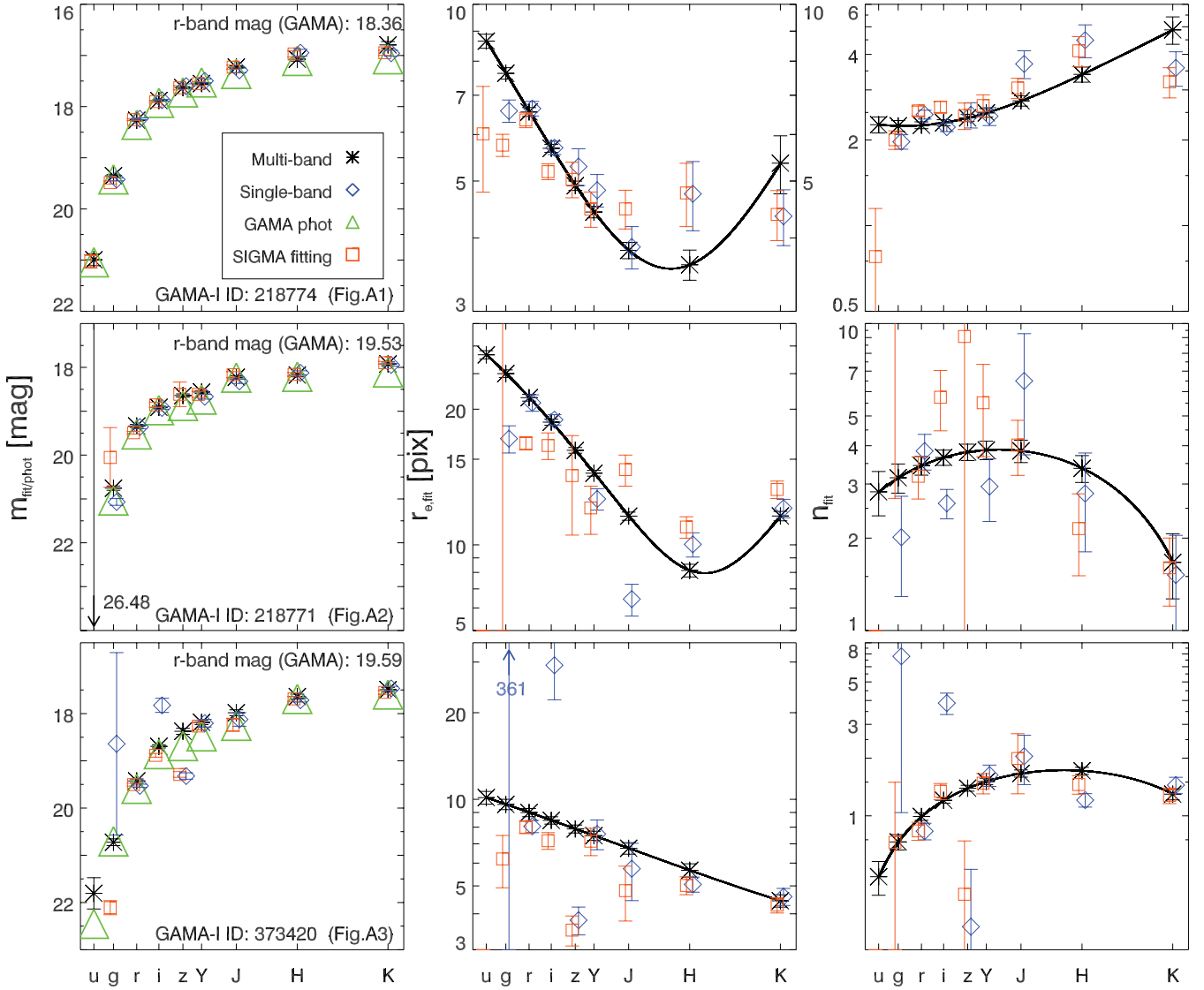
Figure 1. Example fitting results for three individual galaxies as a function of wavelength. The images, models and fitting residuals of both single-band (Mode_S1) and multiband fitting (Mode_M) are shown in Figs A1–A3 in the Appendix. We show recovered magnitudes on the left, where we compare to both GAMA (SEXTRACTOR MAG_AUTO from catalogue ApMatchedCatv03; green triangles) values and single-band fits by (K12, orange boxes). The black asterisks show multiband results, the blue diamonds show results from single-band fits (please note that single-band values have been slightly offset to the right, values from K12 slightly to the left, in order to make the error bars more visible). The error bars shown in all panels are parameter uncertainties as returned by GALFIT. It is clear that single-band fitting introduces larger scatter than multiband fitting, particularly for fainter objects. In the middle column, we show the same comparison for galaxy sizes. For comparison, we show the r_e from the Sérsic fits of K12. Here, by design, the multiband fitting returns sizes which vary as a polynomial of second order with wavelength, indicated by the black line. In the right-hand column, we show similar figures for Sérsic index. Again, by design, multiband fitting returns a smooth dependence over wavelengths. Multiband fitting generally follows similar trends, but largely reduces the scatter and the error bars. In all panels, please note that missing single-band points (both in our own analysis and in the values by K12) indicate that these fits were unsuccessful, and so no sensible value is available, e.g. all three of these objects have no single-band fit for the *u* band in our own analysis and only the first object has a value by K12. Please see the text for more details.

fitting. Importantly, the images for all nine bands have been 'micro-registered' on to the same pixel grid, using SWARP (Bertin et al. 2002).[5] This procedure also homogenizes the photometric zero-points and sky background in order to produce an artefact-free mosaic.

K12 has presented the results of single-band Sérsic-profile fitting for all GAMA spectroscopic targets ($r < 19.8$) in the GAMA I fields.

This catalogue has provided a very useful comparison data set, enabling us to carry out initial tests and aiding the early development of our code. We have used our own software to perform single-band fits, to ensure a fair comparison with our multiband results, and so fitted parameters from K12 are not shown in this paper other than in Fig. 1. A more complete comparison between the two different single-band codes used here and in K12 is beyond the scope of this paper and requires a detailed discussion about minor details in the two codes. However, we have made detailed comparisons between our single-band results and those of K12, finding generally excellent agreement. The PSFs used in this paper are those obtained by K12

---

[5] Note that small systematic sub-pixel offsets between the bands have been reported in K12, but we ignore these here.

Table 1. Summary of the three different fitting modes used in this paper.

Mode	#GALAPAGOS runs	Method of detection	Method of fitting
Mode_S1	9 (1 run each band)	Individual bands	Single-band
Mode_S2	9 (1 run each band)	Co-added image	Single-band
Mode_M	1	Co-added image	Multiband

with GALAPAGOS choosing the closest PSF to the targeted object for the fit.

The imaging data used in this analysis will be made public in GAMA data release 2. Compared to the already public DR1 images, these images cover a larger area with a slightly different pixel scale to better match forthcoming GAMA data sets. The only modifications we make to these imaging data is the addition of a background pedestal so that GALFIT can construct correct sigma images. For each band, we simply use a typical background value from the original SDSS imaging.[6] We also cut the images into overlapping tiles, which makes the data easier to handle in GALAPAGOS.

A second set of images is used within GAMA to carry out the aperture photometry used in Section 7. In order to derive aperture matched photometry, all images have been blurred to a common PSF size of 2 arcsec FWHM, creating a homogeneous data set and avoiding artificial colour biases that would be introduced by the individual seeings in the nine observed bands.

4.2 Profile fitting

We used our multiband version of GALAPAGOS (itself utilizing GALFITM), to create several catalogues for all objects detected in a small subregion ($\sim 1.3° \times 1.3°$) of the 9 h GAMA field (G09) using the same versions of our codes to ensure maximum compatibility of the results. In all runs on the data, we have used the same setup as closely as possible, including SEXTRACTOR setup. However, the imaging data used for object detection vary. For each single-band fitting run, we have used the same single-band image for object detection, using an identical SEXTRACTOR setup for each (Mode_S1 in Table 1 and throughout this paper). For our multiband fitting run (Mode_M), we used a co-added image that was created by simply adding all individual images without further normalization.[7] Given the background level and noise of the data, this creates a slightly biased image towards red bands (e.g. faint, *u*-band-only detections may vanish in the noise from the *K*-band image), but by adding up the images, we increase the S/N for each pixel in the image, allowing for a very deep and detailed object detection. Most very blue objects that would not be detected in red bands are bright enough to still be detected in the co-added image. Again, the same SEXTRACTOR setup is used for this co-added image. However, the number of detected objects increases dramatically compared to all individual bands (see numbers in Table 2).

Using this arrangement, we run the new codes on each single band (*ugrizYJHK*) individually (Mode_S1) and one multiband data set (Mode_M). Bear in mind that, in the multiband approach, only the detection uses a co-added image, the fitting process utilizes all nine bands individually, though simultaneously. The resulting 10 catalogues (nine single band, one multiband) from these runs are then

matched using a simple RA/Dec. source correlation and all parameters are copied into the one single catalogue that is used throughout this section. For consistency checks and to check whether pre-existing knowledge about additional neighbouring objects gives Mode_M fitting an unfair advantage over Mode_S1 fitting, we have also run all nine single-band fits using detection on co-added images (Mode_S2). The results of this test are discussed in Sections 4.3 and 5.2.

Along with additional information, the resulting catalogue contains, for each mode:

(i) all SEXTRACTOR output
(ii) all setup values for GALFIT
(iii) all fitting values, including χ^2 values and fitting times
(iv) all uncertainties for the fitting values
(v) file names and folders
(vi) flags for neighbours, fitting status, constraints hit during the fitting process
(vii) software versions.

Please note that all magnitudes in the catalogue and used throughout this paper are total-Sérsic magnitudes as directly returned by GALFIT, i.e. integrating the light profiles to infinity. It is perhaps more physically meaningful to consider magnitudes based on integrating the Sérsic profile to some finite radius, e.g. $10r_e$, but this is not done in this work. We refer the reader to K12 for further discussion of this issue.

As our sample contains all detected objects instead of objects with $r < 19.8$ for which spectra have been obtained, redshifts are only known for the minority of objects in our sample. Requiring these would reduce our sample dramatically and restrict the analysis to a much smaller number of bright objects. Instead, for the majority of this paper, we work with apparent magnitudes and sizes, giving r_e and other sizes in pixels. This allows us to consider all objects measured by GALAPAGOS. Physical values are only used in the last sections of this paper where we restrict our consideration to those objects with known spectroscopic redshifts, but use a much larger area to create a catalogue for a sufficient number of galaxies.

Before examining the parameters from our GALAPAGOS catalogue, it must first be cleaned in order to select only the objects that have been successfully fitted by GALFITM. In particular, we wish to identify and discard fits with one or more parameters lying on (or very close to) a fitting constraint, as described in Section 3. Such a fit is unlikely to have found a true minimum in χ^2 space and is indicative of a serious mismatch between the model profile and the object in question. This also serves to remove stars from the catalogue, as explained in Section 3. We keep all objects which meet the following criteria:

(i) $m_{\text{input}} - 5 < m < m_{\text{input}} + 5$,
(ii) $0 < m < 40$,
(iii) $0.201 < n < 7.99$,
(iv) $0.301\ [\text{pix}] < r_e < 399.0\ [\text{pix}]$.
(v) $0.001 < q \leq 1.0$,
(vi) $95 - 5 * mag\_best < fwhm\_image$ and $fwhm\_image < 1\ [\text{pix}]$. These relations were found in the magnitude–size diagram to well separate saturated stars (unsaturated stars) from galaxies and is used within GALAPAGOS for this purpose.
(vii) flag $= 2$.

The magnitude input, m_{input}, is the SEXTRACTOR *mag_best* for each object, with offsets where the multiband detection image is used. This offset was empirically determined using previous results, to adjust (on average) magnitudes measured on the multiband

---

[6] For reference, the values added for *ugrizYJHK* band were 6646, 2833, 3951, 5610, 25338, 5315, 13620, 59374 and 65015 counts, respectively.

[7] All GAMA data provided are normalized in the AB system; co-adding the images is the correct way of combining the different images in an energy driven fashion.

Table 2. The number of objects in the real data set that are detected and successfully fitted, and the corresponding success rate, for each single-band image (only Mode_S1), for the Mode_S1 results combined and for the multiband (Mode_M) technique. 'Combined' in this context does not mean detection on the co-added image (Mode_S2), but combination of all the single-band detections and fit results to create a sample of all detections and successful fits when using *ugrizY JHK* bands or *griYHK* bands, respectively. The reader should take care in interpreting this success rate as a true success rate. Of the order of 50 per cent, detected objects in SDSS/GAMA imaging are stars that are thrown out during the cleaning of the catalogue. This lowers the success rate dramatically, even if all galaxies had valid fitting results. An interpretation of these rates in an absolute sense should take this effect into account, but is not given in this analysis. The fraction of stars in the detections is possibly higher in the shallower bands due to their higher detectability, which would partly explain the lower success rates in these band. As a reliable star/galaxy classification is difficult in order to correct these numbers, we instead show the same values on the right-hand side, but restrict the sample to targeted GAMA galaxies, e.g. no stars and only galaxies with $r < 19.8$. Success rates are indeed much higher when only this bright galaxy sample is considered. Comparing the numbers at the bottom of the table, we can successfully derive all fitting values for 885 GAMA objects out of the 1251 GAMA objects that were detected when using multiband fitting. Requiring all *ugrizY JHK* fitting results from single-band fitting reduces this sample to 75 objects.

Band	All objects			GAMA objects		
	No. of objects fitted	No. of objects detected	Success rate (per cent)	No. of fits	No. of detected	Success rate (per cent)
u	209	3773	5.5	108	281	38.4
g	3276	13 547	24.2	827	1229	67.3
r	5802	19 169	30.3	896	1237	72.4
i	6804	22 059	30.8	907	1235	73.4
z	2117	12 496	16.9	725	1178	61.5
Y	3912	16 200	24.1	859	1221	70.4
J	2530	13 289	19.0	686	1150	59.7
H	5432	17 750	30.6	885	1212	73.0
K	5190	16 117	32.2	770	1171	65.8
Combined single band (*ugrizY JHK*)	**87**	**24 995**	**0.35**	**75**	**1251**	**6.0**
Combined single band (*griYHK*)	**992**	**24 866**	**4.0**	**544**	**1251**	**43.5**
Multiband	**15 666**	**29 205**	**53.6**	**885**	**1251**	**70.7**

detection image to those for individual bands. The (iii)–(v) criteria are slightly more restrictive versions of the fitting constraints used, the next criterion is aimed at separating stars from galaxies in the magnitude–size plane and the last uses a flag that is returned by GALAPAGOS. This flag is used to keep track of the fitting status of objects and is initially set 0 if the fit has not started/tried, 1 if fit has been started – e.g. it stays at 1 if the fit failed for some reason – and 2 if GALFIT finished the fit and returned a result.

This cleaning is done on a band-by-band basis, i.e. the decision for each band is entirely independent of the others. For the multiband catalogue, however, we apply these criteria to all bands simultaneously, i.e. if values of the fit fail to meet the above criteria for any band, the entire fit is considered unsuccessful (but not the entire polynomial is checked, e.g. interpolated values could in places violate these criteria). Hereafter, we refer to the objects in this cleaned catalogue as 'successfully fit' or as having a 'valid fit result', to distinguish them from objects that were detected by SEXTRACTOR, but for which GALFITM 'failed' to find a valid fit (flag = 1 and the objects violating the above criteria), and, in the case of simulated data, galaxies that were too faint to be detected at all. Tables 2 and 3 summarize the numbers of objects and success rates. The reader should be advised here to be careful in interpreting this success rate as a true success rate (especially when comparing to success rates in K12). Of the order of half, the detected objects in SDSS/GAMA imaging are stars, e.g. we would both want and expect those to be filtered out by our catalogue cleaning, e.g. lowering the success rate to 50 per cent, although every single galaxy could have valid fitting results. Whereas K12 applies techniques to recover fitting values for objects that initially failed (e.g. by using different settings and re-running the fit), such a scheme is not present in our software. Although this could be introduced, it creates a less homogenous data set and for the purpose of the single- to multiband comparison in the context of MegaMorph, we avoided this by simply ignoring these failed fits in our analysis.

4.3 Results

After running GALAPAGOS in both Mode_S1 and Mode_M, cleaning the catalogues and correlating the objects, using the same codes, same procedures and with a setup as similar as possible, we are now in a position to compare the single- and multiband techniques. Some example images, fits and fitting residuals for all bands are shown in the Appendix.

Fig. 1 shows some fitting results as a function of wavelength for three of the objects in our real GAMA sample (top to bottom panels). The left-hand column shows recovered magnitudes, as a function of wavelength, from both single- and multiband fitting, in comparison to GAMA photometric data and single-band fits performed by K12. The middle column shows the sizes recovered for the same galaxies, the right-hand column shows Sérsic indices. Please note that the *x*-axis in this figure – and all figures throughout this paper – shows linear scaling with wavelength. Although $\log(\lambda)$ might be physically more meaningful, the scaling parameter in the fitting process was chosen to be linear with wavelength in this work and this should be resembled in the figures, e.g. a linear polynomial would only then appear linear in the figures. Similarly, the slightly distorted shape in the plots for size and Sérsic results from the logarithmic scaling of the *y*-axis.

One visible effect is that the magnitudes recovered by both fitting techniques are nearly always brighter than those from aperture photometry. This offset is expected, as aperture photometry always misses some fraction of the light, whereas the magnitudes from GALFIT integrate the profile out to infinity.[8]

It also becomes clear that even in the case of bright galaxies, some of the single-band fits (e.g. *u* and *z* band in the second

---

[8] For a more detailed discussion of this effect of Sérsic profiles, please see the external literature, e.g. Graham & Driver (2005).

example), fail to return a valid result (with 'valid' being defined in Section 4.2). For fainter galaxies (e.g. the lowermost example), the success rate for single-band fitting decreases and the scatter increases with respect to multiband and aperture-based results. Bear in mind that for magnitudes, we do not constrain the fitting values directly; the smoothness of the recovered SED is an indirect result of constraining the profile structural parameters, and not forced by direct constraints on the magnitudes themselves.

For multiband size measurements, by design, the multiband fitting results lie on smooth curves, which greatly reduces the scatter in this parameter. Especially in the lowermost example, the single-band values vary strongly (and arguably un-physically, with a size difference between *g* and *z* band of nearly a factor of 100). Generally, for these relatively bright galaxies (chosen to be GAMA spectroscopic targets, with $r < 19.8$), the sizes from multiband fitting follow the trends of the single-band results, but with a more physically realistic smoothness. Even for relatively bright galaxies, single-band sizes vary greatly from one band to the next, often by a factor of a few. Please keep in mind that the error bars shown in all these plots are parameter uncertainties as returned by GALFIT, which have been shown to underestimate the true values (H07) and should be interpreted as a lower limit of the true uncertainty. While we do not believe these error bars to be realistic, they do allow a comparison between single- and multiband fitting. However, we would possibly not consider the upturn towards K-band sizes real. Especially these galaxies show only individual examples and do not represent the population as a whole. An upturn in the K-band sizes in the entire population is not found, see e.g. Fig. 5.

A comparison for Sérsic indices is shown in the right-hand column of this figure, including a comparison to values of K12 where they exist. A comparison to other values from the literature is difficult because no such values exist for most of our objects. Generally, a trend from lower *n* in blue bands to higher *n* in red bands is visible for most objects in our sample. We will investigate the recoverability of Sérsic indices more in Section 5, where a true value is known and an analysis is both easier and more thorough.

In the figures of size and Sérsic index *n* versus wavelength (middle and right column of Fig. 1), we not only show the individual band sizes for the GALFITM multiband fit results, but we also show the full polynomial function ($\tilde{p}_i(\lambda; \{q_{i,\cdot}\})$; cf. Section 2.1.1) as a black line. An elegant side-effect of fitting these polynomials, rather than values specific to the wavelength of each band, is that it allows easy estimation of sizes (as well as other parameters) at intermediate wavelengths. For scientific analyses, one often wishes to compare rest-frame parameter values. The polynomial parameter functions, inherent to our multiband approach, provide a simple way to determine these, with greater accuracy than could be obtained by interpolating between single-band values. However, as discussed in Section 3, we cannot take the same approach with magnitudes, because the high-order polynomials used for these suffer from Runge's phenomenon. This issue, and ways around it, are discussed in Paper I. In this work, we take the conventional approach and treat the magnitudes as discrete values, and determine rest-frame values via SED template fitting using KCORRECT (Blanton & Roweis 2007).

In a similar manner to the individual examples shown in Fig. 1, in Fig. 2 we show trends for magnitudes recovered using both single- (both Mode_S1 and Mode_S2) and multiband fitting for our entire sample of real galaxies. Lacking 'true' values, we cannot show the offset and scatter of the two methods, instead we consider the average SED. All the individual galaxy SEDs were normalized to an *r*-band magnitude of zero before averaging, to minimize the scatter due to different galaxy brightnesses. As a comparison, we
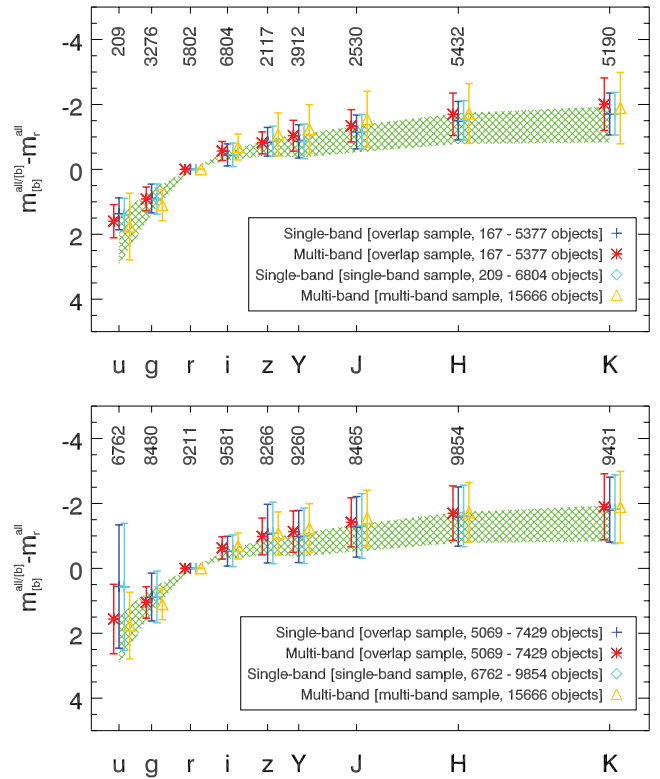

Figure 2. Average normalized SED for various methods and samples. The upper figure shows Mode_S1 as blue data points, the lower figure uses Mode_S2 (increasing sample sizes, but introducing additional scatter), please see text for discussion. All input SEDs are normalized to zero magnitude in the *r* band. The dark blue crosses and the red asterisks indicate the average SED from single- and multiband fits to an overlapping sample, in which each galaxy has valid fitting results from both techniques. The light blue diamonds display the same trend for all single-band fits, irrespective of whether the multiband fitting result and especially the other single-band fits in the other bands were valid. Conversely, the orange triangles show the SED for all multiband fits, irrespective of whether the single-band fit returned a valid result. Points other than dark blue are slightly offset in wavelength for readability of the figure. The error bars on each point show the rms scatter of the normalized SEDs (resistant mean, iteratively clipped at 3 sigma). The numbers above the points for each band refer to the number of valid single-band fits for that band (light blue sample). The numbers in the legend give the ranges of the other samples. Note that multiband fits are either valid for all bands or for none at all, so the multiband sample contains the same number of objects in each band. For comparison, the green shaded area shows the normalized SED, and its rms scatter, for GAMA aperture photometry of 972 GAMA objects that were identified in the same survey area, e.g. they would be a subset of galaxies in our total sample. As our samples do contain fainter objects, not targeted by GAMA, no perfect match is expected. In the lower panel, we can see that the improvement of Mode_M versus Mode_S2 appears very large. However, please see the text for further discussion.

show the average SED for a bright galaxy sample based on aperture photometry from the GAMA survey, normalized in the same way. This comparison, while not being perfect due to differences in the samples shown, gives an indication of the intrinsic scatter in galaxy SEDs.

In the upper panel of Fig. 2, we show the comparison between Mode_S1 fitting (e.g. only using single-band data for the entire process, including object detection) and multiband fitting. In the lower figure, we show what happens when *multi*band detection is used for *single*-band fitting (Mode_S2).

First, we will discuss the upper figure here. Overall, both single- and multiband fitting show the same trend. Both results show slight offsets with respect to the general GAMA SED (as determined by aperture photometry, see discussion below), as derived from 972 GAMA objects identified in the region. Most of the scatter in the normalized SEDs is due to intrinsic variation between the galaxies. Lacking a 'true' comparison value makes it difficult to make more stringent tests, but there are hints that the scatter (for the same sample please compare dark blue and red data points in Fig. 2) is slightly reduced in most bands when multiband fitting is used (especially in low-S/N bands, *u* and *z*). The normalized SEDs for the entire multiband sample (orange) shows larger scatter and offsets even when compared to the full single-band sample (light blue). This is a result of the multiband sample containing fainter galaxies than the others. Using real data, it is not clear whether the increased scatter compared to the general GAMA SED is a result of worse fitting results, or real variations that are not reflected in aperture photometry. However, this effect will be examined using simulated data without such scatter in Section 5.

The most dramatic advantage of multiband fitting becomes apparent when comparing the sample sizes of galaxies for which parameter values can be derived. Whereas the single-band fits return valid results for between 209 (*u*-band) and 6804 (*i*-band) galaxies, the multiband fitting returns valid values in *all* bands for 15 666 objects. However, there are two effects at work here; the number of valid fits in each band depends upon both the number of objects detected and the fitting success rate. The former is a result of the chosen detection image and SExtractor setup. The Mode_S1 results in this figure use single-band detections, while the multiband results are based on detections on a co-added (and hence deeper) image. Table 2 gives the number of objects detected in the imaging for each band, and the number of those objects which are successfully fitted by single-band GALAPAGOS. It also shows the resulting numbers of objects with valid single-band measurements for every band (*ugrizY JHK*), or just the six highest S/N bands (*griYHK*). Finally, Table 2 gives the number of objects detected in the co-added multiband detection image, and the number of these with valid multiband fits (and hence meaningful measurements in all *ugrizY JHK* bands). While the number of detections plays an important role (e.g. the number of *u*-band-detected sources is 20 per cent of that for *r* band), the fit success rate is significantly higher for multiband than for any of the individual single-band fits, and much greater when one requires complete multiband data. While of course benefiting from detecting more objects, this shows that the multiband approach is more stable and thus more often returns valid measurements that are more likely to resemble the true parameters of the galaxy.

The substantial difference in the number of objects returned by Mode_S1 and Mode_M methods is partly due to the initial object detection. The multiband fits are based on a multiband detection image, and hence fits are attempted for many objects which are undetected in some of the single-band images, especially *u* band. It is possible that single-band fitting may be able to return meaningful values for these objects, if it were to be aware of their presence. To investigate this, we have repeated the above analysis, but using the multiband detection image even when fitting single-band data (Mode_S2). In addition to making the single-band method attempt to fit more targets, the additional objects will result in differences in deblending, masking and starting parameters. This potentially gives single-band fitting a better chance of measuring reliable galaxy parameters.

We will discuss this test in more detail in Section 5 where performance comparison is easier. Here, we only show an example for magnitude, in the lower panel of Fig. 2. Two effects are strikingly evident. First, Mode_S2 fitting now indeed does return valid fitting results for many more objects (as apparent from the numbers at the top of the figure). The samples are still smaller than for multiband fitting, indicating that GALFIT still fails to return a valid fit more often than for multiband fitting. Secondly, those objects that the code does succeed in have a much larger scatter than the multiband results (compare dark blue to red error bars, which show the scatter for an identical sample of objects). While the use of multiband detections does greatly increase the sample sizes, the scatter in the single-band fitting results has increased dramatically as well, especially in the *u* and *z* bands. This confirms that the improvement in fitting quality and sample size when using multiband fitting does indeed result from the strength of the multiband fitting approach presented in this paper, and not simply due to the advantage of using a multiband detection image. Our multiband fitting technique can recover reliable measurements in bands where the objects are too faint to be reliably fitted (using a single-band method) or even detected.

The relatively poor behaviour of the single-band fits to multiband detections can be attributed to a number of potential causes. The simplest explanation is that without the constraints on the size and shape of the profile, which naturally come from higher S/N bands in multiband fitting, single-band fits produce more uncertain results in the low-S/N bands. However, there are two additional effects that may be at work. First, given that the fitting position of the profiles is only constrained to be within the postage stamp, potentially one or more neighbouring (secondary) objects may 'wander off', away from their intended targets (which may be undetectable in the single band) and on to the (primary) target object. Such behaviour would lead to a fainter magnitude being returned for the primary, as its flux is distributed between multiple profiles. Secondly, the opposite is possible. When the primary source is much fainter than any of the secondaries, or even invisible in the single-band image that is being fitted, the primary profile may 'wander off' to settle on a secondary object. While the stacked profiles would split the secondary flux, the resulting magnitude might be brighter than that of the true primary source. We did not further investigate which of these effects dominates, as GALAPAGOS does not return the fitting values of secondaries and this investigation is beyond the scope of this paper. In the case of multiband fitting, these issues becomes much less significant as the profile position is effectively constrained using information from all the bands.

Our Mode_S2 fitting results could hence potentially be improved either by imposing tighter constraints on the positions, thus preventing profiles from 'wandering off' their intended target, or by using profile information from one fit (e.g. on the *r* band) to constrain or fix parameters in a subsequent fit on a lower S/N band. However, this is not as natural nor effective a solution as the multiband approach we advocate in this paper.

The last thing to note from our detection-image test is that some of the objects that are missing from our Mode_S1 fit results, but which are recovered in Mode_S2 fits, have relatively bright magnitudes. These may be objects with low surface brightness, which are undetected in some of the single-band images, particularly *u* band, despite their integrated brightness. Furthermore, even when single-band fits are aware of these objects in Mode_S2, these fits frequently fail to extract meaningful information, in contrast to multiband fitting. The implication of this is that, without taking the multiband approach, we preferentially lose information about galaxies with less-peaky profiles, i.e. discs.

Fig. 3 is similar to Fig. 2, but only considers two stringently defined subsets: 84 galaxies for which *all* single-band fits returned a
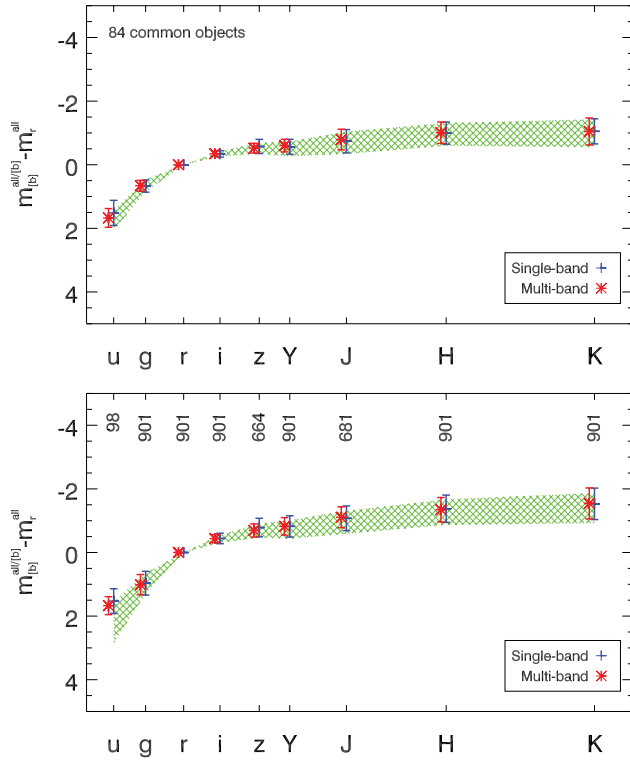
Figure 3. Similar to Fig. 2, these figures show the average normalized SED and the scatter around that average. Both figures use Mode_S1 data, but now for a small sample of 84 galaxies for which *all* single-band and multiband fits return a valid results (top panel) and a sample of 901 galaxies for which the *griYHK* bands return valid results (bottom panel). All points within each figure therefore incorporate the same objects (unless numbers indicate differently in the lower panel). The shaded green areas in each figure show normalized SEDs based on GAMA aperture photometry, using the galaxies in our samples for which these values exist. This sample hence forms a very similar sample to the ones used in the plotting symbols, which explains the much better agreement between points and shaded green area compared to Fig 2.

valid result, and 901 galaxies for which we obtained valid values in the six highest S/N (*griYHK*) bands. This makes the comparison between the codes much easier and cleaner, as the same sample of galaxies is compared at all times. Both the Mode_S1 and Mode_M fitting results closely agree with one another and the GAMA aperture photometry. However, while subtle, it is also apparent that multiband fitting slightly reduces the scatter for most bands. This is shown more clearly using simulations in Section 5.2.

We do not explicitly show a figure similar to Fig. 3 for Mode_S2 results. However, we can show from our analysis discussed above, that, while again the sample size increases when multiband detection is used, the scatter of the single-band fitting results increases dramatically.

The sample sizes in Fig. 3 highlight an important problem with single-band fitting, at least in the simplest case of treating each band completely independently, as we do here. As detailed in Table 2, we only obtain meaningful parameter values in *all* bands for 87 objects (992 objects in the case that only *griYHK* values are needed). With multiband fitting, we derive valid parameters in all bands for 15 666 objects, an increase in sample size of a factor of ∼180 (∼16), and obviously a valuable advantage. As mentioned above, this is partly due to the use of a multiband detection image (which can only be reliably used with multiband fitting), and partly due to an increase
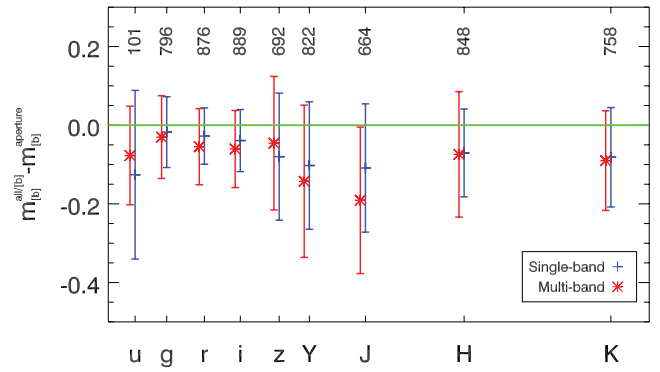
Figure 4. Difference between magnitudes obtained from GALFIT (blue crosses: Mode_S1, red asterisks: Mode_M) and aperture photometry measured by the GAMA survey, using SEXTRACTOR. We show the figure for a sample of galaxies with $r < 19.8$ for which, for each filter band, all of these measurements exist. We recover fainter magnitudes below the green line, and brighter magnitudes above. At first glance, the multiband fitting results seem slightly worse, returning significantly brighter magnitudes. We will demonstrate, however, in Section 5, specifically Fig. 12, that SEXTRACTOR magnitudes are bad proxies for this kind of test and that the multiband fits are better at recovering true total magnitudes.

in the fitting success rate, thanks to the stability achieved by constraining the profile shape across multiple bands. The advantage of the multiband approach becomes especially evident in science cases where parameter values are required in several bands, which, in the case of single-band fitting, decreases the sample size dramatically. While multiband fits derive valid values for ∼54 per cent of detected objects (∼71 per cent of galaxies considering only a sample of bright GAMA galaxies), a combined single-band approach only recovers valid parameters for <0.4 per cent of these objects (6.0 per cent of bright galaxies) and ∼4 (∼44) per cent when only values in the higher S/N bands (*griYHK*) are needed. Such a science case is discussed in Section 7.

The normalized SEDs, given in Figs 2 and 3 allow us to evaluate the band-to-band variation of our measurements, and compare these to aperture photometry. However, the scatter in these SEDs are dominated by intrinsic variations in the galaxy population. We therefore perform a further comparison of our GALFIT magnitudes directly against GAMA aperture photometry, a test that would be carried out by most authors as performance tests of profile fitting codes. The results of this test are shown in Fig. 4.[9]

This comparison in Fig. 4 is only possible for a subset of galaxies in each band, those which have valid fitting results for the method in question. As previously mentioned, some offset is expected as aperture photometry will always miss some fraction of the light from the outskirts of the galaxies. On the other hand, integrating galaxy light profiles out to infinity can add fictional flux particularly for high-*n* systems, making the definition of a true value difficult. The GALFIT magnitudes are indeed systematically brighter than aperture photometry by 0.1–0.2 mag. The scatter between GALFIT and aperture magnitudes is also 0.1–0.2 mag, depending on typical S/N of the band, suggesting that much of this scatter could result from variations in the flux missed by aperture photometry for galaxies of different profile shapes. The single- and multiband fitting results appear quite similar, although the multiband magnitudes generally

---

[9] This figure looks very similar if we use magnitudes from the individual SEXTRACTOR runs performed for object detection in GALAPAGOS.
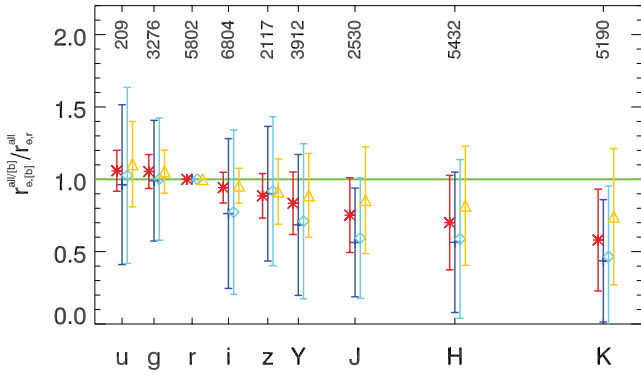
Figure 5. Comparison of the trend in measured half-light radius versus wavelength for single- and multiband fitting. Symbols and colours indicate the same samples as in Fig. 2. The half-light radii for each galaxy are normalized using the *r* band, and the average variation in relative size versus wavelength is shown by the points. We recover larger half-light radii above the line, and smaller below. The rms scatter around this trend is indicated by the error bars. Both single- and multiband approaches reproduce no significant average trends, but clearly the multiband technique reduces the scatter substantially.

display slightly greater offsets. However, from this figure, it is difficult to determine which magnitudes best represent the total light and colours of the target galaxies. We explore this in a more satisfactory manner in Section 5, with the use of simulations.

Magnitudes are integrated quantities, and are therefore generally the easiest galaxy properties to extract from imaging. Another important galaxy property is size. Size is a natural, direct product of Sérsic profile fitting. It may be defined in many ways, but a convenient and commonly used value is the half-light radius. This is the size measure returned by GALFIT.

We follow the same approach as for magnitudes (cf. Figs 2 and 3). Figs 5 and 6 show the trend in galaxy half-light radii, normalized to the *r* band, as a function of wavelength (similar trends have been reported by K12, see Fig. 6). Error bars indicate the scatter in these normalized sizes. Fig. 5 compares the Mode_S1 and Mode_M results using samples of valid objects for each technique, and an overlap sample, containing only objects with valid results in both techniques (dark blue and red data points). Fig. 6 limits the comparison sample further to those for which single-band fits for *all* bands, or the six highest S/N (*griYHK*) bands, returned a valid result. In contrast to magnitudes, for which the scatter is only slightly improved, the scatter on the recovered sizes are hugely improved by multiband fitting. These figures also display an average trend, recovered by both techniques, such that galaxies appear smaller in redder bands. This can be explained by two processes. First, blue band galaxy light is typically dominated by galaxy discs, whereas in red bands bulges, which are usually smaller than discs, contribute a greater fraction of the light (see magenta and orange lines in Fig. 6). Secondly, a combination of dust and stellar populations in pure disc galaxies can create a similar effect (Möllenhoff et al. 2006; Pastrav et al. 2012; Pastrav et al., in preparation; see dashed line in Fig. 6 for the effects of dust on the measured half-light radius).

The reduction in scatter we see in Figs 5 and 6 is at least partly by design, as the half-light radii are constrained to lie on a second-order polynomial as a function of wavelength. Such a reduction in scatter would therefore be seen even if the real sizes of galaxies did vary wildly with wavelength. However, from inspection of the single-band fits, i.e. figures like Fig. 1 for many more examples, we see that sizes do show a smooth, and nearly linear, trend with
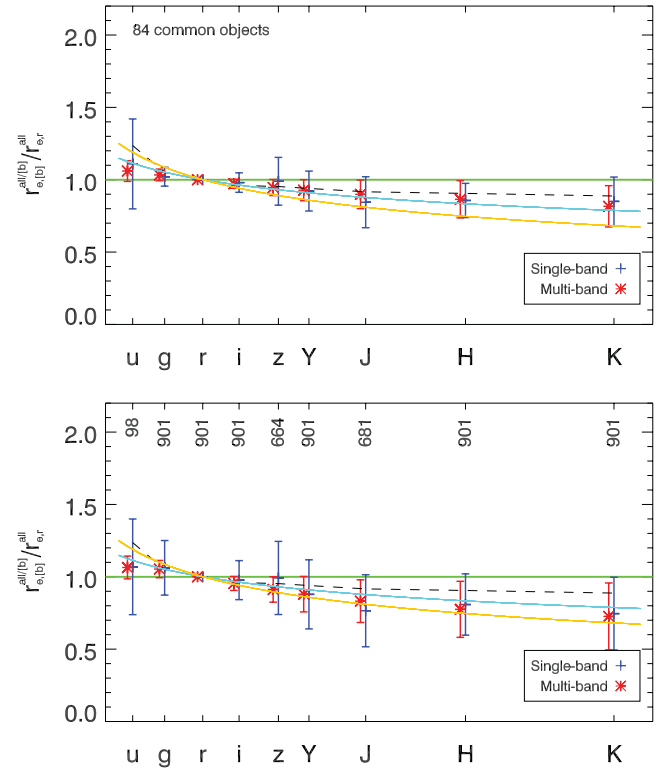

Figure 6. Similar to Fig. 5, these figures compare trends of half-light radius versus wavelength, but now for (top panel) a small sample of 87 galaxies for which all Mode_S1 and Mode_S1 fits return a valid results and (bottom panel) a sample of 901 galaxies for which the *griYHK* bands return valid results in Mode_S1. All the points within each figure therefore correspond to the same objects. The improvement in scatter when using multiband fitting is especially evident in this figure. For comparison, we show the relations described in K12 for spheroid-dominated galaxies (orange) and disc-dominated galaxies (light blue) which describe the same trends found in our data. The black dashed line shows the effect of dust content in the galaxy on the size measurements (while ignoring intrinsic stellar population gradients) from Pastrav et al (in preparation), based on the radiation transfer model of Popescu et al. (2011).

wavelength. Consideration of physically realistic stellar populations also supports smooth variations in half-light radius with wavelength. Such was our justification for using second-order polynomials in the first place. As we lack an independent estimate for the 'true' sizes of the objects, we cannot investigate this further with real data. However, in the following section we use simulations to demonstrate that the multiband approach results in significantly improved size measurements, suggesting that the reduced scatter in Figs 5 and 6 corresponds more closely to the true variation in relative size with wavelength.

For comparison, we illustrate the trends described in K12 for both spheroid-dominated and disc-dominated galaxies in Fig. 6. Given the clean sample in this figure, which mostly consists of bright galaxies that would also be targeted by K12, we can confirm to find very similar trends of r_e with wavelength.

Determining galaxy size may be thought of as finding a radius for which the integrated flux within and without corresponds to a given ratio. The behaviour of the profile within each of those two regions does not matter, and there is no ambiguity in the definition for any arbitrary monotonic profile. Determining Sérsic index requires further information, particularly regarding the behaviour of the profile at its peak and in its tail. Higher Sérsic indices imply a
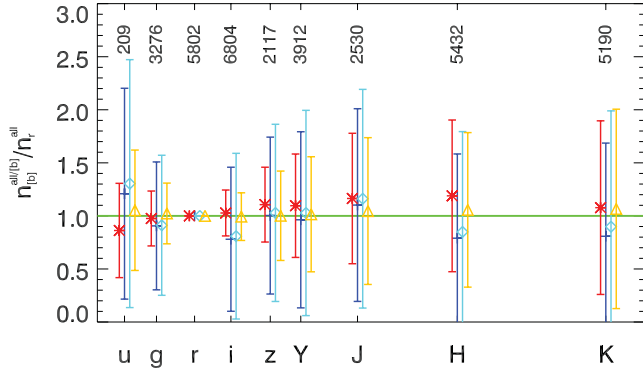
Figure 7. Comparison of the trend in Sérsic index versus wavelength for Mode_S1 and Mode_M fitting. This figure includes all galaxies, e.g. no 'morphology' selection has been done. Symbols and colours indicate the same samples as in Fig. 2. The Sérsic indices for each galaxy are normalized using the *r* band, and the average variation in *n* versus wavelength is shown by the points. We recover larger Sérsic indices above the line, and smaller below. The rms scatter around the observed trend is indicated by the error bars. Single- and multiband approaches reproduce similar average trends, but the multiband technique reduces the scatter substantially.

greater shift of flux from around the half-light radius and into both the centre and outskirts of the profile. However, these pieces of information need not be consistent for an arbitrary monotonic profile. The Sérsic index is therefore more difficult to measure accurately and consistently.

In Figs 7 and 8, we present a comparison of Mode_S1 single band and Mode_M multiband fitting results for Sérsic index along the same lines as for half-light radii, again, slightly arbitrarily, normalizing all objects to the *r*-band Sérsic index. Again, a general trend in *n* with wavelength, similar to the ones reported in K12, is recovered by both single- and multiband fitting, although, given the scatter in single band, it is much more visible in multiband results. This trend confirms our argument that in blue bands one fits a light profile dominated by a galaxy disc (low *n*) whereas in red bands, the bulge dominates the light profile (high *n*). The same effects regarding the scatter of the fitting values are seen, multiband fitting hugely reduces the scatter in *n* and increases fitting quality. As expected, the scatter in both single- and multiband fitting is larger for *n* than for r_e, strengthening the argument that Sérsic indices are indeed the hardest values to measure.

We can compare our data to the trends described in K12, which we show as lines in Fig. 8. We generally find a qualitatively similar trend, but find it to be stronger than discovered in K12. The reason for this is that the sample in K12 has been split up into disc-dominated and spheroid-dominated samples using a cut in the (UV)–n_k plane. This split and the normalization to the *r*-band Sérsic index in Fig. 8 suppress the trend found in our work and lead to shallower trends. This effect can be confirmed in Fig. 8. As splitting up the sample into disc and spheroid-dominated sample is beyond the scope of this paper, this effect is expected in this comparison.

In a similar manner to half-light radius, the reduction in scatter for Sérsic index is partly by design, as we constrain the values to lie on a second-order polynomial as a function of wavelength with the caveats discussed above. Again, from inspection of the single-band result, we decided that fitting a second-order polynomial to the Sérsic index as a function of wavelength generally provides sufficient flexibility to fit most real objects. Again, we refer to Section 5.2 for a more detailed and normalization-independent evaluation of the fitting accuracy of the Sérsic parameter.
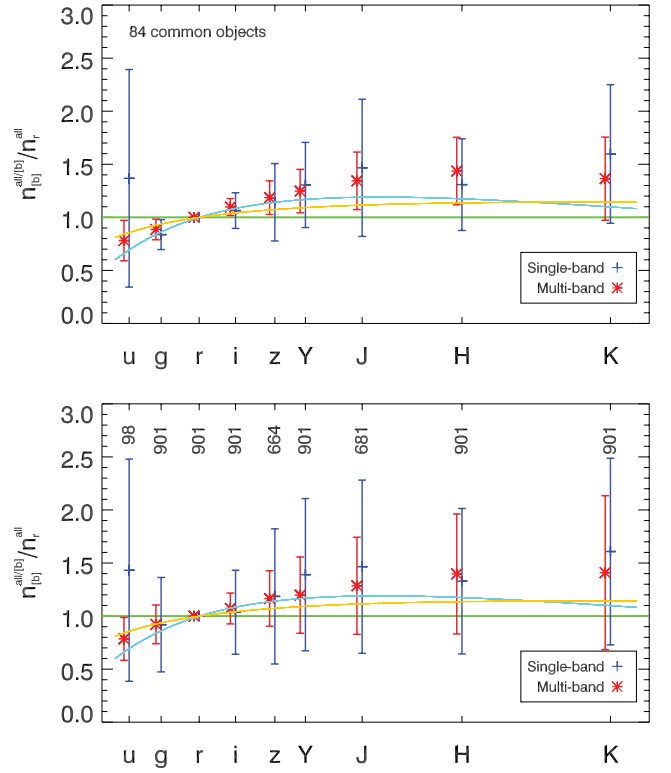

Figure 8. Similar to Fig. 3, these figures compare trends of Sérsic index versus wavelength, but for a small sample of 87 galaxies for which all single-band and multiband fits return a valid results (top panel) and a sample of 901 galaxies for which the *griYHK* bands return valid results (bottom panel). All the points within each figure therefore correspond to the same objects. The improvement in scatter when using multiband fitting is very evident in this figure.

5 APPLICATION TO SIMULATED IMAGING

Unlike observed data, which have the advantage that the galaxies in the data truly are real and include internal galaxy structures, such as spiral arms, star-forming regions and asymmetries, simulated data have the advantage that one knows the input galaxy parameters. This allows for a direct comparison of recovered magnitudes, half-light radii and Sérsic indices to their true values, instead of being limited to comparing to alternative estimators, such as aperture photometry or Petrosian radii, or similar Sérsic profile measurements from other studies. The results are therefore much cleaner and free of the intrinsic scatter which dominates most figures in the previous section. Additionally, one can examine in more detail the ability of multiband fitting to recover the variation of galaxy sizes and Sérsic indices with wavelength.

On the other hand, simulations have the disadvantage that the objects now all possess the smooth, symmetric profiles for which we know that Sérsic profiles (with some polynomial wavelength dependence of their parameters, and convolved by a known PSF) will precisely fit the data. Our simulation can only test the fitting routines under the assumption that galaxies are intrinsically representable by perfect Sérsic profiles. We know that for some galaxies, and for all galaxies observed in sufficient detail, this is not true. In this sense, simulations are an idealized case and, while allowing a good comparison of single-band to multiband fitting, they can only give a lower limit on the error bars for real data.

5.1 Creating the simulations

To create our simulated data, we follow the methodology of H07, making adaptations to the scripts as necessary to enable the simulation of a multiwavelength data set.

As in H07, we started from a catalogue of results from fitting profiles to real data, in order to get the distribution of galaxy parameters in the simulated images as close to that of a real sample as possible. We decided to start from the sample used in Section 4 and 'cleaned' as described above. We first divide the r-band $m-\log(r_e)$ plane into bins of width 0.4 in m and 0.1 in $\log(r_e)$. Following H07, to create the parameters for each simulated galaxy we select an r-band $m-r_e$ bin, and use the centre of this bin as our starting value for r-band magnitude. We then pick a real galaxy at random from that bin, from which we obtain realistic values for r-band effective radius, Sérsic index and axis ratio, as well as the wavelength variation for each parameter, including colours. The centre position and position angle were chosen randomly for each object.

To produce a simulated data set with the same magnitude and effective radius distribution as the real data, we selected r-band $m-r_e$ bins with a probability weighted by the distribution of real galaxies in this plane. However, in order to test the code at the detection limits we extend the faint side of the magnitude distribution. This was achieved by finding the peak in the number density of galaxies versus magnitude, for each r_e bin, and extending this peak level two magnitudes fainter (as was done in H07).

As in H07, we slightly varied the galaxy parameters produced by the above procedure, in order to create a smooth distribution, instead of simply re-simulating the same few galaxies over and over. These applied variations are as follows.

Position: the x and y centre coordinates in the simulated field are randomly chosen (although of course neighbouring tiles are consistent in their overlap regions), but are identical for all bands (no statistical or systematic offsets are applied).

Magnitude: starting from the initially chosen r-band magnitude, we first apply an offset, drawn from a Gaussian distribution with standard deviation of 0.4 mag. To define the magnitudes in the other bands, colours (as differences of the other bands to r band) are directly taken from a real galaxy within the corresponding $m-r_e$ bin and added to the r-band magnitude. The magnitudes in the individual bands are finally modified by adding Gaussian noise with a 0.1 standard deviation. The magnitudes were allowed to vary freely as a function of wavelength in the fitting process applied to the real galaxies, so there are no smoothness constraints on magnitude in the simulated data set.

Half-light radius: the fits to the real data were carried out using a polynomial of second order to describe the wavelength dependence of r_e. We start with the function taken from a real galaxy in the selected $m-r_e$ bin. We then add an additional linear slope, drawn from a Gaussian distribution with standard deviation corresponding to a 10 per cent change in r_e over the full wavelength range. No noise is added to the individual bands, so that simulated values follow a second-order polynomial exactly.

Sérsic indices: similar to r_e, in the fits to the real data the wavelength dependence of n was described by a second order polynomial. For most of the simulated galaxies, starting values are taken from the same real galaxy as before, but in this case we simply modify the values in all bands by a factor drawn from a Gaussian with mean 1 and standard deviation of 0.3. This offsets the values, but preserves the linear and quadratic coefficients. The simulated values therefore follow a second-order polynomial exactly. However, for 5 per cent of objects we instead randomly chose n uniformly from the range 0.2–8, with a linear slope as a function of wavelength. This was done in order to cover areas of parameter space that are not covered by the cleaned catalogue of real galaxies, either because no such galaxies exist or such galaxies defy reliable detection or modelling. As these areas are of particular interest to us, we simulate some galaxies to cover them.

Axis ratio: this is simply taken from the chosen real galaxy and offset by a Gaussian random variable with standard deviation 0.1 (subject to the allowed 0–1 range of this variable). The same value is adopted by all bands, and no additional noise is added to the simulated images.

Position angle: this is randomly chosen, with the same value applied to all bands, with no further noise added.

Following H07, we added Poisson noise to the simulated images and then added them into an image that is made up of empty sky patches from the real GAMA imaging. This means that sky noise is present in the simulated images with the same properties as in the real data.

The result of this procedure is a realistic-looking set of images with thousands of galaxies that mostly show the same parameter distributions as the real galaxies, and for which we know the true parameter values. It should be noted that these images do not contain any stars, due to the cleaning of the catalogue prior to parameter selection. A fraction of real galaxy images are contaminated by stars, which must be masked or deblended by GALAPAGOS, potentially leading to additional uncertainties which are neglected by our simulations. However, blended galaxies are naturally included by our simulation method, and so the effects of blending are included in our results.

5.2 Results

In this section, we examine the single- and multiband fitting results by comparing the recovered parameter values to the true, simulated values directly. Where possible, we recreate figures similar to those in Section 4, but we are able to examine issues in more detail and add a set of figures which could not be created using real data.

When running the codes we use exactly the same setup and procedures as were used for real data in the previous section. In particular, we use the same versions of our codes (GALFITM version 0.1.2.1, GALAPAGOS version 2.0.2). We run the same three scenarios, i.e. Mode_S1, Mode_S2 and Mode_M, and carry out the same procedure to combine the individual catalogues (nine single band, one multiband) in order to create one single catalogue which is used throughout this section. This catalogue is additionally correlated to the simulated catalogue using RA and Dec., so that true values for all objects are known (disregarding the potential for rare misidentifications).

We show some fits of individual simulated galaxies in Fig. 9. As for real galaxies, it is apparent that multiband fitting returns values for more bands, making studies using multiple sets of values (e.g. colours) possible for a larger sample of galaxies. It also reduces the scatter on all the values that are measured. Whereas the single-band magnitudes (and even sizes in the brighter galaxies) generally return sensible values, the r_e and Sérsic indices recovered are typically much noisier in single-band fitting compared to multiband fitting. Multiband fitting generally recovers the shape of the wavelength dependence well, but this is of course a function of magnitude, where fainter galaxies are generally less well recovered.

In addition to returning more accurate values at the specific wavelengths of the input images, multiband fitting also provides the entire polynomial over the wavelength region. Estimations of
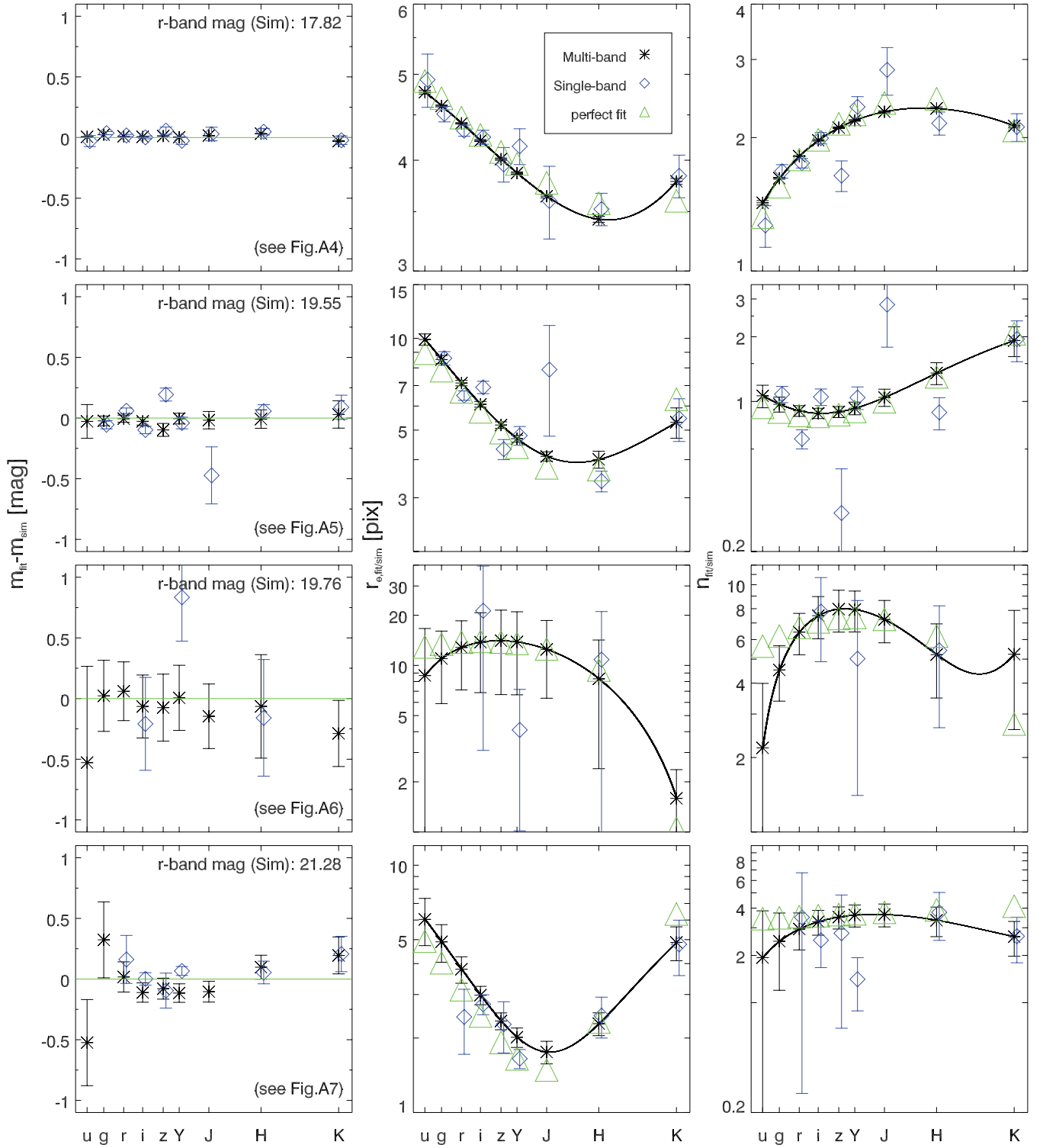
Figure 9. Fits for individual simulated galaxies, similar to Fig. 1 in the case of real galaxies. The images of these objects, together with models and fitting residuals from both Mode_S1 and Mode_M fitting, are shown in Figs A4–A7 in the Appendix. The left-hand column shows the magnitude difference between fitted and simulated values. The green line/values indicates an ideal fit (no offset between fit and simulated values), the blue diamonds show Mode_S1 fitting results, the black asterisks show Mode_M results. The middle column shows both simulated and recovered half-light radii in all bands. The black line shows the entire polynomial that is fitted to the data for Mode_M; in contrast to single-band fitting, where only some of the individual values exist, we derive the entire function in the case of multiband fitting. The right-hand column shows the simulated and fitting values for Sérsic indices. The *r*-band magnitude of the objects is indicated in the leftmost figure. See further discussion in the text.

values at intermediate wavelengths, e.g. rest-frame values, therefore become trivial. As long as they are within the wavelength range covered by the input images, they can simply be obtained from the polynomial. As mentioned in Section 3, this interpolation is not sensible for magnitudes, for which we use a higher order polynomial, due to Runge's phenomenon. In any case, we have a better understanding of galaxy SEDs, and so it is wise to use this knowledge, e.g. via template spectra, to estimate accurate magnitude *k*-corrections.

After visually inspecting a large fraction of individual fits, we found that multiband fitting was able to successfully outperform single-band fitting in all cases when the multiband fit was not rejected due to proximity to a fitting constraint. The opposite case – objects where multiband fails but single-band fits return results for at least some bands – does occur, but is less common. Numbers to illustrate this are included in Fig. 13. As expected, we also find that for very faint galaxies (*r*-band magnitude ∼23, close to the SDSS detection limit), the wavelength dependence of the sizes and Sérsic indices do not match that simulated, and the magnitudes are very noisy. On most of these objects single-band fitting is not able to recover many, if any, values. However, parameter estimates from the Mode_M fits, though noisy, were generally still in agreement with the simulated values, given the big error bars.

In Fig. 10, we illustrate the performance of single- and multiband techniques for recovering the magnitudes of our simulated galaxies. This is an equivalent figure to Fig. 2, but compares directly to the simulated parameter values, rather than arbitrarily normalizing the SED to the *r* band. The intrinsic scatter in galaxy colours, which obscured improvements in scatter in Fig. 2, is not present in this figure. The offset and scatter in this figure represent the true bias and uncertainty in our ability to recover object parameters. As in Fig. 2, one can see that the scatter is significantly reduced in most bands when using multiband fitting. Multiband fitting also somewhat reduces the small offset that is apparent in low-S/N bands (mainly *u* and *z* band).

The scatter and bias for the complete multiband sample (shown in yellow) are significantly larger. This is largely due to the inclusion of large numbers of faint objects in this sample and will be examined in detail later (in Fig. 13).

The lower panel in Fig. 10 shows the same figure as the upper panel, but for Mode_S2 results. Similar to what was seen using real galaxies, the improvement from Mode_S2 to Mode_M fitting is more dramatic than from Mode_S1 to Mode_M. Our arguments for this are similar to the ones presented in Section 4.3. The results of Mode_S2 fitting are worse largely because the effect of neighbouring galaxies. Either the primary object wanders off to fit a secondary (in which case the fit would likely appear to be too bright), or a secondary can centre on the primary (in which case the fit would appear to be too faint). Multiband fitting is largely immune to such issues, as the higher S/N images naturally constrain the position of the target in the lower S/N bands. Table 3 presents the fitting success rates for the simulated galaxy sample, in a similar manner to those shown in Table 2 for the real data. The fitting success rate here is much higher than in the case of real galaxies. There are two distinct effects responsible for this. First, the simulated images do not contain stars, due to the cleaning of the fitting catalogue prior to parameter selection. As stars typically result in 'failed' fits, by design, their absence from the simulations naturally means that the resulting success rate is boosted. The remaining improvement is largely due to the fact that all the simulated galaxies actually resemble smooth Sérsic profiles, which makes the fitting process much more stable, even in single-band fitting and in low-S/N bands.
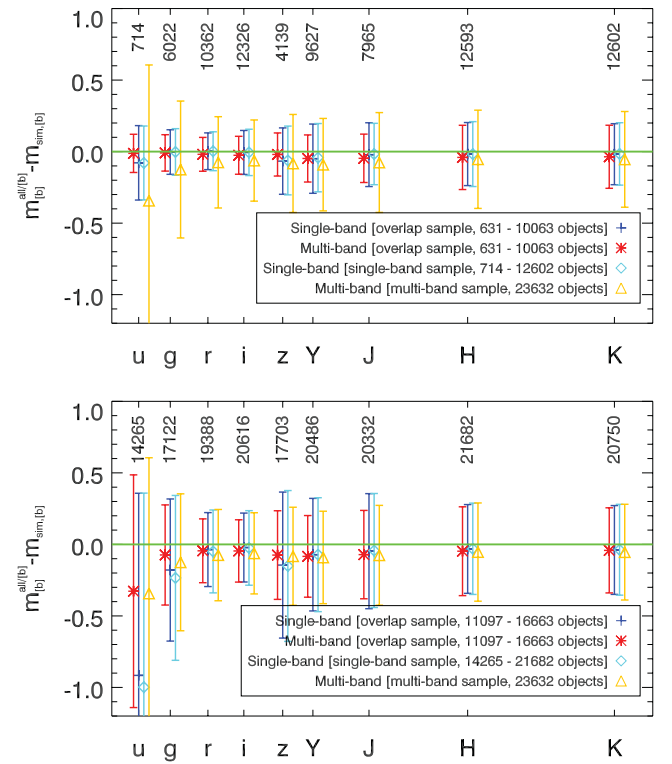

Figure 10. Magnitude recoverability for simulated galaxies (Mode_M and Mode_S1 in the top panel, Mode_M and Mode_S2 in the bottom panel). Note especially the change of quantity on the *y*-axis compared to Fig. 2; for simulated galaxies we are able to demonstrate the difference between simulated and measured values. This means that the measurement uncertainties are no longer convolved with the intrinsic scatter on the colours, permitting a more stringent comparison between techniques. For example, while on real galaxies the scatter in the *u* band is around 0.5 mag, it is only about 0.2 mag here. Multiband fitting produces a smaller scatter in comparison to single-band results. Systematics are very small, although both techniques do display a bias to recover brighter magnitudes by <0.05 mag. The sample size is enlarged by the multiband approach from 714 (*u* band) or 12 602 (*K* band) in single-band fitting to 23 632 objects in multiband fitting, nearly a factor of 2 more objects even for the best single bands. These numbers are compared in more detail in Table 3). In the bottom panel, the bias introduced by combining multiband detection with single-band fitting (Mode_S2) becomes very apparent. This is simply a result of attempting to model objects that are below the noise limit.

The multiband technique is not the one with the highest success rate on simulated data. Due to a more sensitive detection in Mode_M compared to Mode_S1, the sample includes many more faint galaxies which are harder to fit and decrease the success rate. The overall number of objects for which parameters can be derived is still higher. When comparing the overlap of the samples of single band with each other and the sample in multiband fitting, the increase is still substantial, effectively providing fits for seven times more galaxies in a sample that is only twice the size to start with. This emphasises how dramatically the size of scientific samples can be increased by using multiband fitting.

To emphasize the effect on sample sizes, and ensure a consistent comparison. Fig. 11 again shows the recoverability of magnitude by both single- and multiband fitting, but for matched subsamples for which all, or most, Mode_S1 results return valid fitting values. In both cases, the reductions in both scatter and offsets are clearly visible for most bands. Low-S/N bands particularly benefit from the multiband approach. The values from the top panel in Fig. 11

Table 3. Object numbers in the simulated data set and fraction with successful fits for Mode_S1 and Mode_M. Please note that the success rate in this simulated sample resembles an actual success rate and does not include stars that are purposefully excluded from the final analysis, but which suppress the apparent success rate in Table 2. In that respect, the success rates in this table are more comparable to those presented for the GAMA galaxy sample in Table 2.

Band	No. of objects fitted	No. of objects detected	Success rate (per cent)
u	714	1213	58.9
g	6022	8839	68.1
r	10 362	13 739	75.4
i	12 326	16 490	74.7
z	4139	6196	66.8
Y	9627	13 123	73.4
J	7965	11 068	72.0
H	12 593	16 992	74.1
K	12 602	17 755	71.0
Combined single band (*ugrizYJHK*)	**305**	**26 308**	**1.2**
Combined single band (*griYHK*)	**2560**	**25 631**	**10.0**
mwl	**23 632**	**31 798**	**74.3**

Table 4. Mean and scatter of the magnitude offsets for Mode_S1 and Mode_M for a sample of objects with complete Mode_S1 measurements, as shown in the top panel of Fig. 11.

Band	offset $\pm\sigma$ Mode_S1	offset $\pm\sigma$ Mode_M
u	-0.06 ± 0.17	0.00 ± 0.09
g	0.02 ± 0.04	0.01 ± 0.04
r	0.01 ± 0.03	0.01 ± 0.03
i	0.00 ± 0.04	-0.01 ± 0.04
z	-0.05 ± 0.12	-0.02 ± 0.12
Y	-0.03 ± 0.11	-0.03 ± 0.07
J	-0.03 ± 0.14	-0.03 ± 0.09
H	-0.02 ± 0.11	-0.05 ± 0.11
K	-0.03 ± 0.13	-0.04 ± 0.17
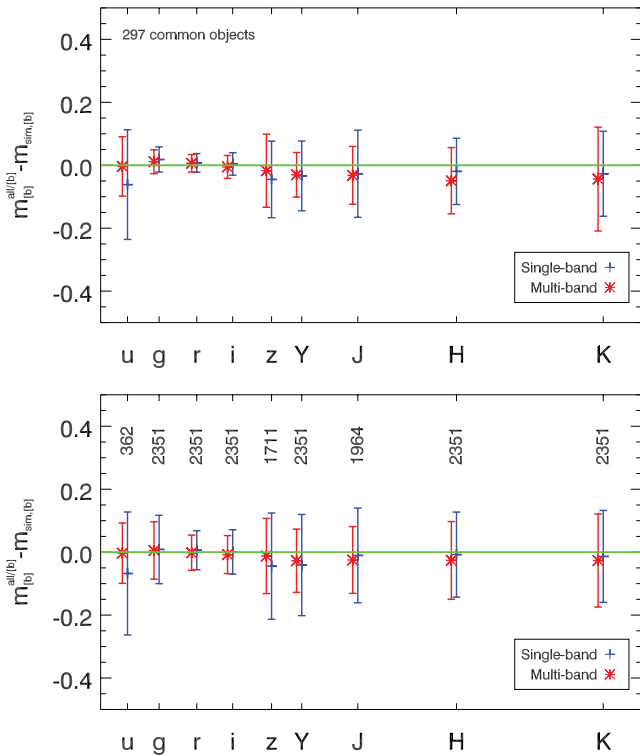
Figure 11. Magnitude recoverability in simulated data for galaxies with complete sets of single-band fits. These figures are the same as the top panel of Fig. 10, but show only a common sample of 297 galaxies for which all Mode_S1 fits return a result (top) or 2351 galaxies that have fits in *griYHK* (bottom). For these common samples, multiband fitting clearly increases the accuracy and precision for magnitude measurements. For reference, the values shown in the top panel are given in Table 4.

are also given in Table 4. Biases are somewhat reduced at most wavelengths, while scatter is reduced significantly in the low-S/N bands and slightly in the other bands.

In Fig. 4, we compared magnitudes derived by GALFIT with those obtained using aperture photometry, finding a consistent offset of ~0.1 mag, which appeared greater when using the multiband

technique. In Fig. 12, we follow up on this by comparing magnitudes from Mode_S1 and Mode_M fits, as well as SEXTRACTOR '*mag-best*' aperture magnitudes, to their simulated values. The GALFIT results are the same as those shown in the top panel of Fig. 10. It is obvious that the offset in Fig. 4 is a result of SEXTRACTOR underestimating the total flux. Both single- and multiband fitting provide better estimates of total magnitude. Fig. 4 therefore does not show which method recovers the better values. However, as Fig. 4, together with Fig. 10, serves as a simple illustration of the issues in comparing aperture and model photometry, we retain it. Note that our simulated magnitudes are based on Sérsic models integrated to infinity, as are the magnitudes recovered by GALFIT. Aperture magnitudes necessarily do not measure the flux in the distant tails of the profile, and it is arguable whether this flux actually exists, as much of it is at surface brightnesses fainter than can possibly be measured. This is discussed in much more detail by K12, who advocate using magnitudes obtained from truncated Sérsic profiles for all science analyses.

A more complete presentation of the results from fitting simulated data is presented in Fig. 13. For each band (*u*, *g*, *r*, *i*, *z*, *Y*, *J*, *H*, *K* from top to bottom), we show the magnitude offset from the fitting values, but instead of putting everything into one bin as in the previous figures, we show them as a function of simulated (true) galaxy
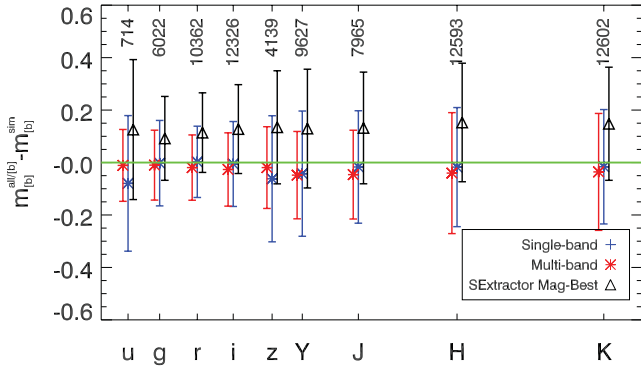
Figure 12. Equivalent to Fig. 4 we show here the deviations of recovered magnitudes for both Mode_M (red) and Mode_S1 fits (blue) compared to SEXTRACTOR '*mag-best*'. For comparison, we show the deviations of the SEXTRACTOR magnitudes from the simulated values as black data points. Clearly visible, SEXTRACTOR magnitudes produce a much larger offset to simulated magnitudes and are not a good proxy for 'real' magnitude. Either multi- or single-band fitting recover the simulated magnitudes better. This puts Fig. 4 and the offsets of Mode_S1 and Mode_M values in this figure in perspective.

magnitude.[10] The left-hand column shows results from Mode_S1 fits with the mean offset and rms scatter overlaid in light blue (dotted lines indicate the $\pm 1\sigma$ scatter); the right-hand column shows the same for Mode_M fits, with the mean offset and rms scatter for the whole object sample in light blue. Black numbers in the top-right corner of each panel show the number of objects appearing in the figure, i.e. simulated objects which have been detected and successfully fit by the method in question. Additionally, in both columns, we overplot the sample of objects for which both Mode_S1 and Mode_M fits return a valid result in yellow. Yellow numbers in the top-right corner of the left-column panels give the number of objects in these samples. One can see that not all objects with single-band fits have successful multiband fits, but the fraction is much higher than the other way around. We show the mean trends and rms scatter for this overlap sample for Mode_S1 fits in blue in the left-hand column and, to aid comparison, for Mode_M fits in red in both columns.

For an ideal fitting code, the mean and scatter lines should be close to zero at all input magnitudes, indicating that no systematic or statistical biases exist in the fitting routines. As one can see, both single-band and multiband fitting values are not significantly biased for most galaxies, but the multiwavelength fitting reduces the scatter somewhat, particularly in lower S/N bands. The improvement is not significant for the overlap sample of galaxies in some higher S/N bands, but even in these cases the multiband approach significantly improves the completeness of the sample.

At this point, we would like to remind the reader that before creating these figures we cleaned our catalogue of objects that ended up close to fitting constraints. As mentioned above, the total number of successfully fitted objects is indicated by the black number in the corner of each panel. As one can see, the numbers of objects for which we can get valid results is much larger in the case of multiband fitting, confirming our findings from Section 4. Whereas in *r* and *i* band the sample size only doubles, we can obtain fitting parameters for 30 times more galaxies in the *u* band. In most bands,

---

[10] We note that when using observed surface brightness on the *x*-axis, the figures look qualitatively very similar.

we can also recover values for fainter galaxies. As these are harder to fit and result in larger error bars, they also lead to a large 'scatter' in Figs 10–12 (orange symbols). This is expected and does not imply that Mode_M fits are less accurate than Mode_S1 fits, as could be wrongly interpreted from the error bars in those figures.

For reference, we show, as a vertical purple line in the *r*-band panels in Fig. 13, the $m_r = 19.8$ magnitude limit of the spectroscopic survey carried out as part of the GAMA project. For galaxies brighter than this limit, both single-band fitting and multiband fitting do a similar job of returning good fitting values. However, the accuracy and precision of the recovered parameters are clearly improved by the multiband method, particularly for lower S/N bands and, as we shall see, size and Sérsic index. One distinct advantage of the multiband technique is its ability to obtain valid results for fainter objects. However, if one is only interested in bright galaxies, e.g. for which spectroscopy has been obtained, then the difference in terms of sample size is less clear. To examine this, we estimate fitting limits from the single-band data, indicated by the vertical green lines in each panel of Fig. 13. These lines are defined as being 0.5 mag fainter than the peak in the magnitude histogram for Mode_S1 detections. The blue number in the right-hand column shows the number of galaxies brighter than this limit that returned valid results in Mode_S1 fitting, the red number shows the corresponding number using Mode_M fitting. As one can see, the multiband fitting returns useful results for appreciably more galaxies, even in this bright sample of objects. This illustrates that the increase in overall sample size is not only due to adding fainter galaxies, but also due to deriving valid fitting results more often for bright galaxies.

To investigate this topic further, we print two fractions in each panel in green. The top number shows the fraction of galaxies simulated brighter than the single-band fitting limit (vertical green lines) for which we obtained valid fits. However, this fraction includes the issue of single-band versus multiband detection completeness and is therefore not a direct comparison of the robustness of the fitting techniques. In order to take out the detection issue, we determine the fraction of objects detected in each band (and above the fitting limits) for which we obtained valid fitting results. These are given by the lower green percentage in each panel. These fractions are higher and correspond more closely to the numbers given in Table 3 for the full sample. They are also similar between single- and multiband techniques, indicating that for bright samples, at least in the case of single-Sérsic fitting, the multiband technique does not make large differences to the number of objects which can be successfully fit. In some bands this success fraction is actually higher for single-band fitting than for multiband fitting. This probably reflects the fact that the cleaning process for multiband is more stringent than that for single band: proximity to a single constraint in any band results in rejection of that multiband fit. Note that even though the individual band success rates are comparable between single- and multiband methods, when one desires a sample with a complete set of measurements across all bands, the single-band method suffers dramatically. This is clearly demonstrated in the final three rows of Table 3. It is also important to remember, as shown throughout this paper, that the accuracy of the recovered parameters, particularly in lower S/N bands, is significantly improved by adopting the multiband technique.

One effective approach to improving the fractions of detections and valid fits is to repeat attempts. In the case of detection, if one knows an object is present in one band, one can attempt to detect it in other bands by varying detection thresholds and deblending parameters. For fitting, whenever a fit ends up on a constraint, one can restart the fit with slightly different initial conditions or
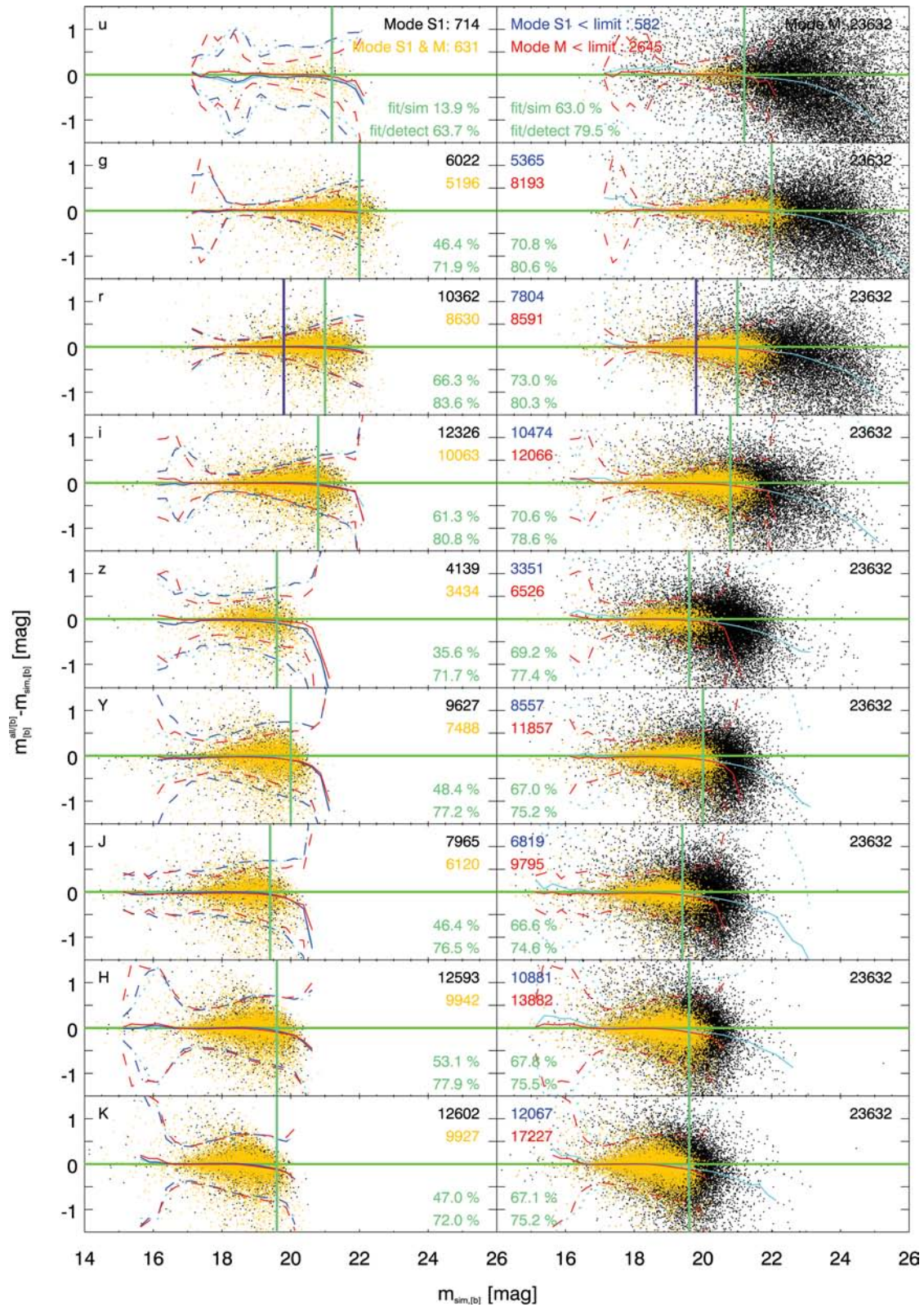
Figure 13. Magnitude fitting accuracy as a function of simulated magnitude. The blue and red dashed lines show the median scatter of the distribution as a function of magnitude for single- and multiband fits for a common sample of objects for direct comparison. The vertical lines show magnitude limits used in the analysis and to derive the objects numbers shown in the different panels. These object counts show the sizes of different samples for which useful values can be derived. Detailed description and discussion of these numbers and this figure can be found in the text in Section 5.2.
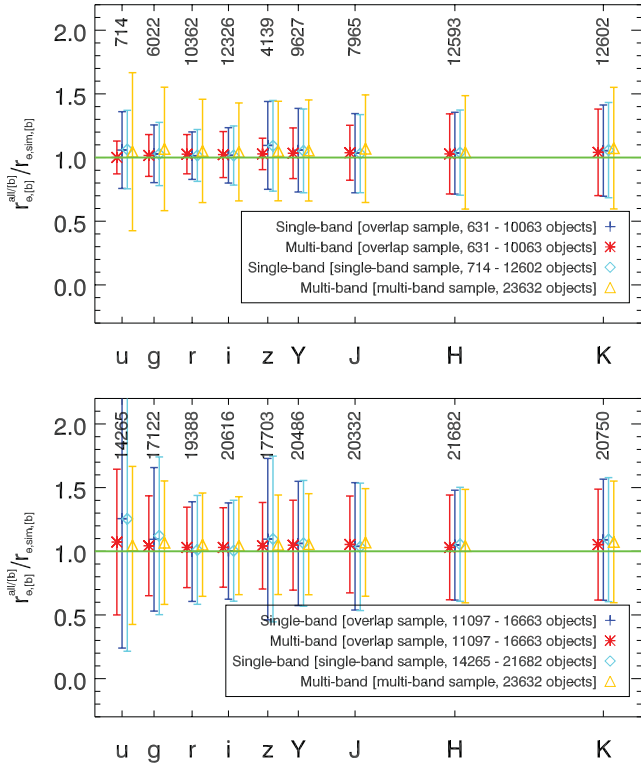
Figure 14. Size recoverability for simulated data (top panel: Mode_S1 and Mode_M, bottom panel: Mode_S2 and Mode_M). Fitting results are improved when using multiband fitting. The increased error bars in the case of the entire multiband sample (in orange), largely come from adding in much fainter galaxies, see Fig. 16 and discussion in the text. Only a very small systematic offset is visible, even when including the faintest galaxies.

Figure 15. Size recoverability for simulated data, similar to Fig. 14, but only for the subset of galaxies where all Mode_S1 fits (top) or *griYHK* band fits (bottom) return valid results. It is evident that multiband fitting, when comparing the same sample of galaxies, decreases the scatter and thus hugely improves the recoverability of galaxy sizes.

masks, hoping that one of these repeats will produce acceptable values. Both of these approaches are adopted by K12, with the result that their fractions of valid fits are significantly higher than ours. However, the fact that restarting GALFIT with slightly different parameters can produce different final results is concerning, and it is uncertain whether parameter values obtained after several attempts are reliable. In our case, we take constraint violations as a signal that reliable results cannot be obtained for the object in question. It is not yet clear which approach is most appropriate, although we aim to investigate this question further in future work.

In Figs 14–16, we show the equivalent analysis to that presented above, but now considering the recoverability of effective radii in the simulated data. This complements the similar analysis that was performed using the results of fitting real data in Section 4.3. As was seen in Section 4, our multiband fitting technique dramatically improves the fitting accuracy for galaxy sizes. This is true in all bands (but especially those with low S/N), and at all magnitudes. In Figs 14–16, we qualitatively confirm the result that we found for real galaxies. However, using the simulations we can make more quantitative statements. Fig. 15, in particular, shows that galaxy half-light radius can be measured with much higher precision in the case of Mode_M compared to Mode_S1. The values from the top panel in Fig. 15 are given in Table 5. Fig. 16 shows that multiband fitting can measure reasonably accurate sizes even for very faint objects, even in bands where the object may be below the single-band detection limit.

Figs 17–19 repeat the same analysis for Sérsic indices. Similar to half-light radii, the improvement in fitting quality is much clearer
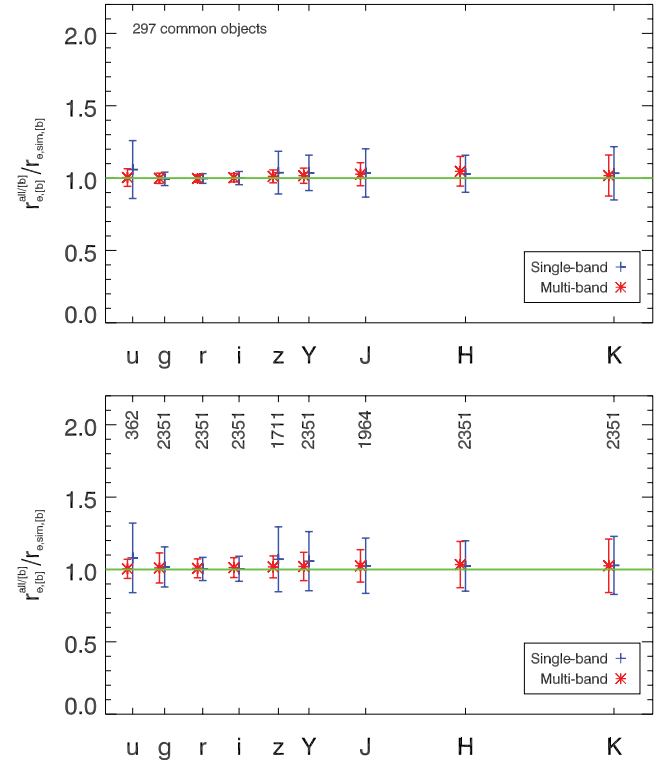
than for magnitudes. Be aware that the error bars in all figures are relative errors, but they combine values from galaxies with different Sérsic indices. A galaxy with $n = 4$ is much harder to fit than a galaxy with $n = 1$, mostly due to uncertainties in the sky estimation (H07), so this way of plotting reduces this effect. Values from the top panel in Fig. 18 are shown in Table 6, showing that the measurements of Sérsic index are significantly improved when multiband fitting is used. In Fig. 19, we show the effect as a function of simulated magnitude. While small systematic effects are visible for fainter galaxies, the improvement in fitting quality when using multiband fitting is evident, especially in the lower S/N bands.

We have shown that using multiple band images simultaneously, with structural parameters that are required to vary smoothly as a function of wavelength, can dramatically improve both the robustness of fits to faint galaxies and the accuracy of recovered parameters for objects of all brightnesses. The examples in Figs 1 and 9 indicate that the recovered wavelength dependencies do reflect the intrinsic variations of the structural parameters between wavebands. We now examine the meaning we can ascribe to the measured Chebyshev coefficients more closely.

The simulated galaxies were created such that the simulated values for r_e and n follow second-order polynomials, e.g. making a second-order polynomial the perfect fit to the simulated data. We have intentionally allowed more freedom, using third-order polynomials in both r_e and n, when fitting these data with the multiband technique, in order to test how well we can recover the correct trends. In Fig. 20, we show histograms of the Chebyshev coefficients for r_e: q_1 (black), q_2 (green) and q_3 (red). There are several things to mention about this figure. First, the histogram for q_1 is clearly offset
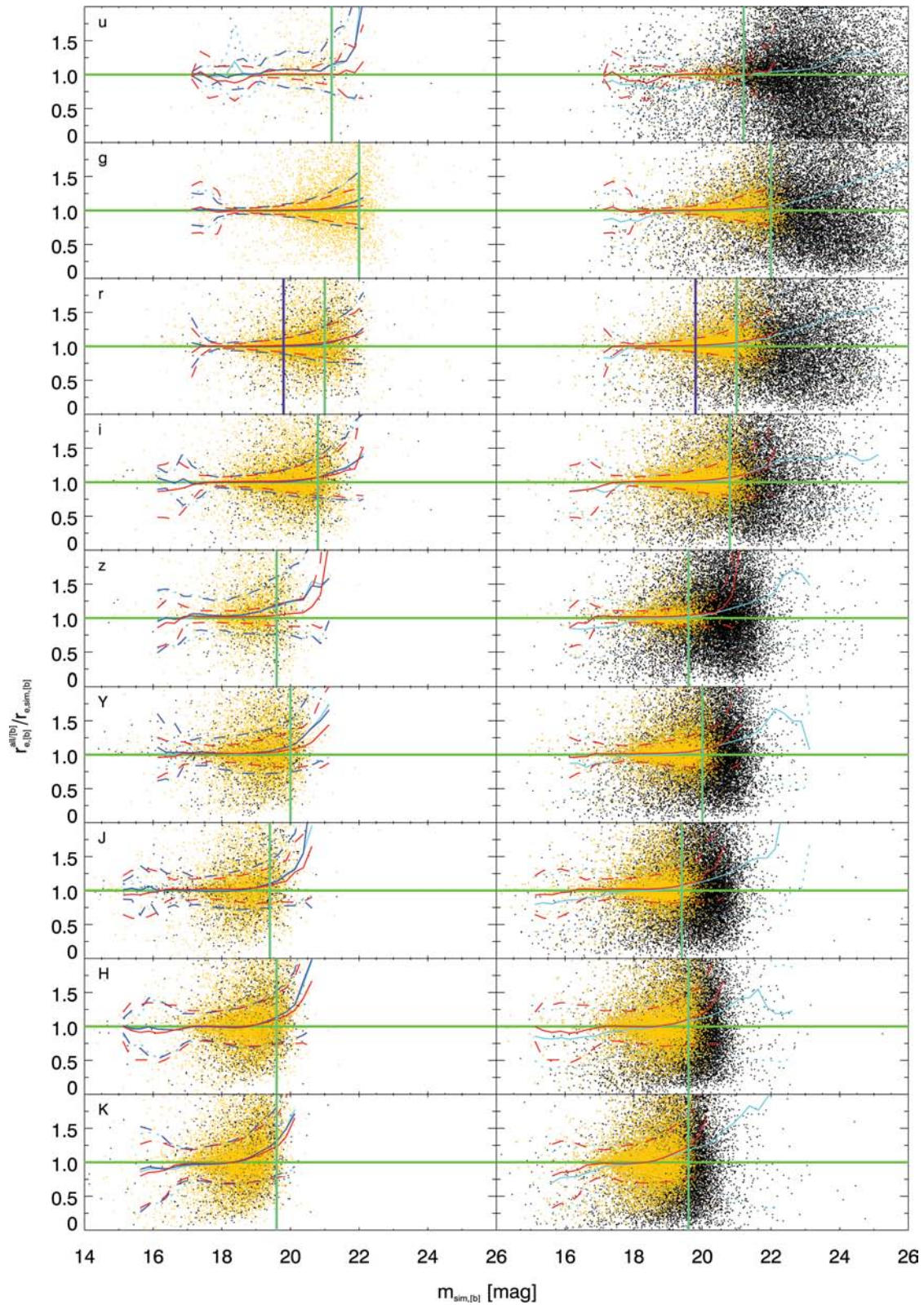
Figure 16. Simulation results showing the recoverability of effective radius for each band as a function of simulated magnitude. Single-band fitting results are shown on the left, multiband results on the right. The points and lines are the same as for Fig. 13. The multiband technique, while only slightly improving on magnitude fitting, greatly improves the fitting accuracy for galaxy size.

Table 5. Mean and scatter of the effective radius offsets for Mode_S1 and Mode_M for a sample of objects with complete Mode_S1 measurements, as shown in the top panel of Fig. 15.

Band	Mean $\pm\sigma$ Mode_S1	Mean $\pm\sigma$ Mode_M
u	1.06 ± 0.20	1.00 ± 0.06
g	0.99 ± 0.05	1.00 ± 0.04
r	1.00 ± 0.03	1.00 ± 0.03
i	1.00 ± 0.05	1.00 ± 0.03
z	1.04 ± 0.15	1.01 ± 0.04
Y	1.04 ± 0.12	1.02 ± 0.05
J	1.04 ± 0.17	1.03 ± 0.08
H	1.03 ± 0.13	1.05 ± 0.10
K	1.03 ± 0.18	1.02 ± 0.14
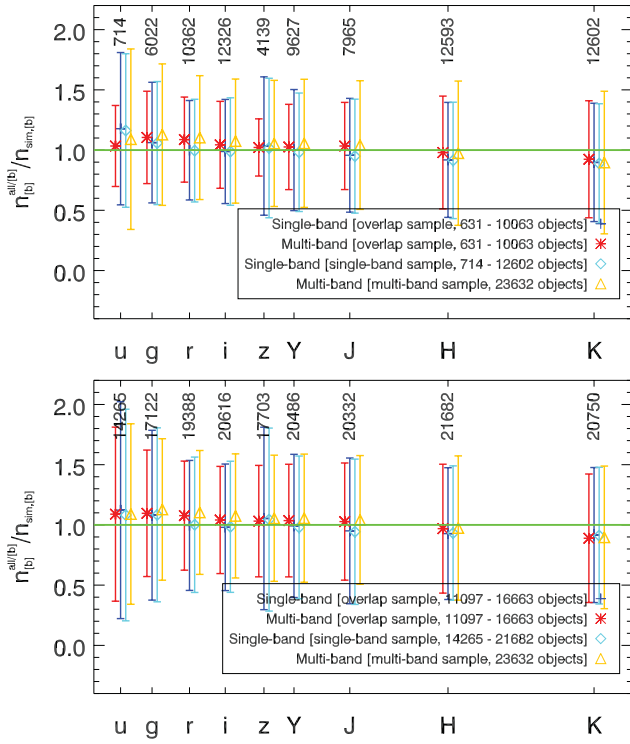
Figure 17. Sérsic index recoverability for the individual bands (top panel: Mode_S1 and Mode_M, bottom panel: Mode_S2 and Mode_M). As for effective radius, multiband fitting reduces the scatter on recovered parameters substantially, without introducing significant systematic effects.

from 0. As q_1 describes the linear terms of the Chebyshev polynomials, this means that statistically a non-flat linear trend (in this case a negative trend) of r_e with wavelength is visible. Galaxies in redder bands generally appear smaller. This effect has already been shown in Fig. 5 for real galaxies. As the simulations were created following this catalogue, the same trend is apparent in the simulated data, but it is pleasing that we can see this directly in the Chebyshev coefficients. Secondly, the histograms for both q_2 and q_3 are not significantly offset from 0, so no systematic trend is visible in the population. This does not, however, mean that individual objects do not significantly show second-order polynomials. Thirdly, and most importantly, the width – and hence the importance – of the third-order term q_3 is significantly smaller than for q_2. Ideally, we
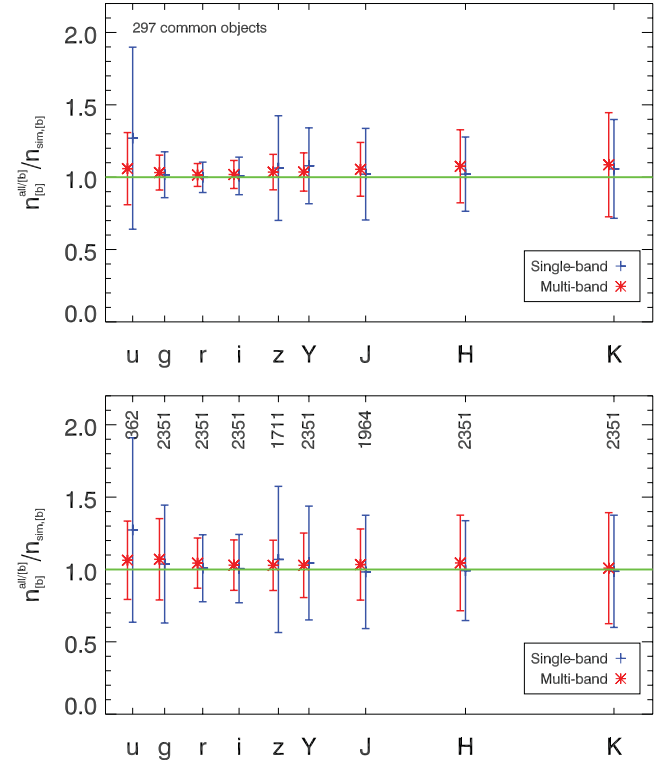
Figure 18. This is the same figure as the top panel of Fig. 17, but now for the subset of galaxies for which all (top) or most (bottom) single-band fits return a valid result. Again, the reduction in scatter for Mode_M is significant.

would want $q_3 = 0$ for all galaxies, but given the noise properties of the image, this was not expected.

A more sensitive way to show this is via the histogram of $\log(|q_3/q_2|)$ in Fig. 21. Plotted this way, the second-order term 'dominates' the shape of the polynomial compared to the third-order term in all galaxies that show $\log(|q_3/q_2|) < 0$, or equivalently $|q_3| < |q_2|$. This is important in order to justify whether the polynomial order fitted to the real data is the correct order to use – e.g. if one fits a third-order polynomial and finds that $|q_3| < |q_2|$ for most galaxies, it is a justifiable assumption that second-order polynomials are appropriate for most objects. In previous tests this is what we have found, hence our decision to fit real galaxies with second-order polynomials and creating simulations to this specification.

6 COMPUTATIONAL CONSIDERATIONS

Other than fitting accuracy, there are also other issues to be considered. In this section, we will discuss some of these issues and compare the single- and multiband fitting procedures.

6.1 Fitting time

Potentially, multiband fitting may require less computing time to produce useful fits for large samples of galaxies, when compared with the single-band approach, as in principle we have fewer free parameters being constrained by the same data set. As we have fitted samples using both methods, we can directly make this comparison. Here, we consider only the fitting time, i.e. the processing time required to process the galaxy with GALFITM. We ignore the time it takes for the fit to be initially set up, as this is similar for both methods. GALAPAGOS does most jobs on a band-by-band basis, so the
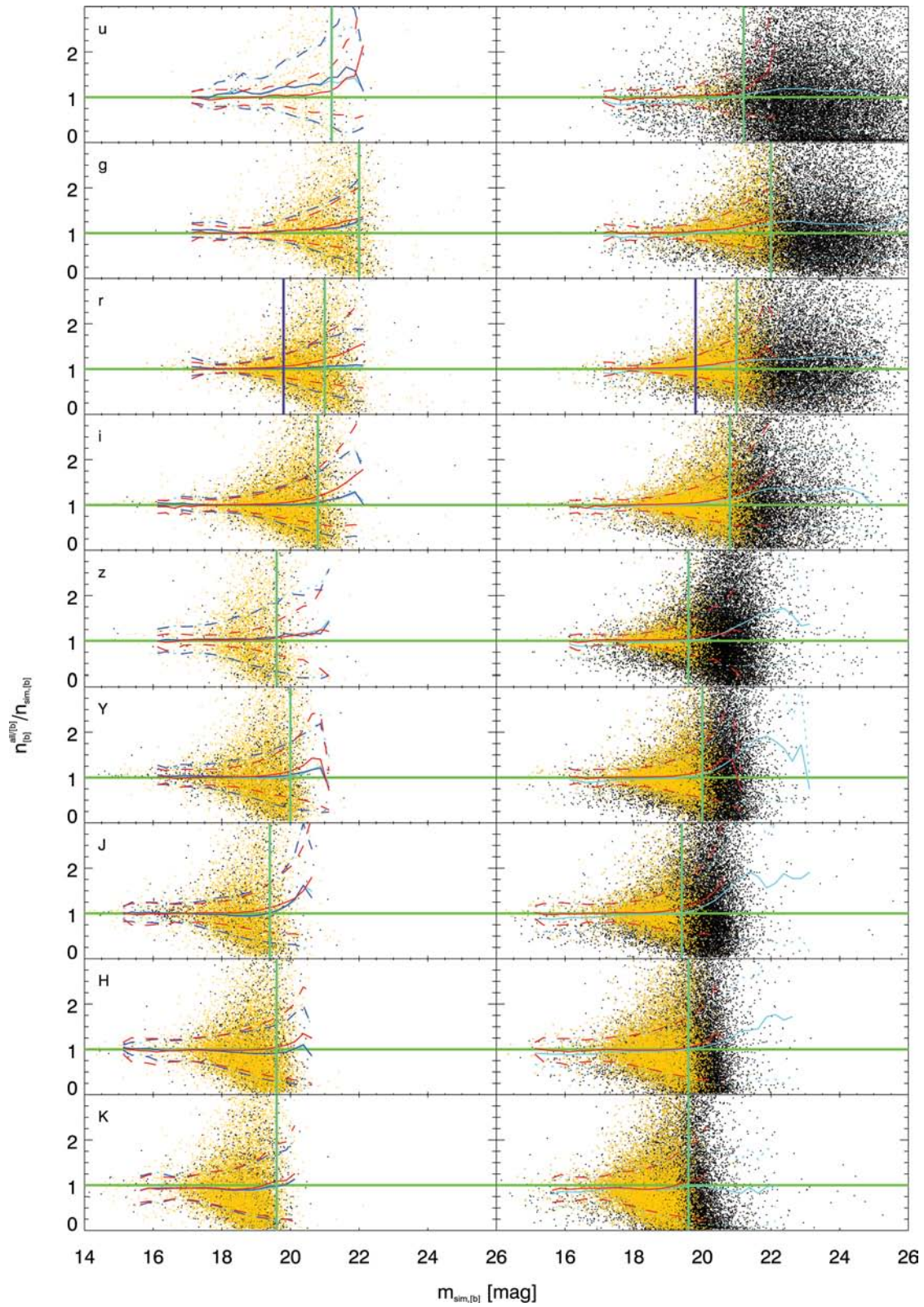
Figure 19. Simulation results for each band: Mode_S1 versus Mode_M. Multiband fitting, while improving the results for simulated galaxies in most bands, multiplies the sample size without increasing the scatter more than would be expected by adding fainter galaxies. The points and lines are the same as for Figs 13 and 16.

Table 6. Mean and scatter of Sérsic index offsets for Mode_S1 and Mode_M for a sample of objects with complete Mode_S1 measurements, as shown in the top panel of Fig. 18.

Band	Mean $\pm\sigma$ Mode_S1	Mean $\pm\sigma$ Mode_M
u	1.27 ± 0.63	1.06 ± 0.25
g	1.02 ± 0.16	1.03 ± 0.12
r	1.00 ± 0.11	1.02 ± 0.08
i	1.01 ± 0.13	1.02 ± 0.10
z	1.06 ± 0.36	1.04 ± 0.12
Y	1.08 ± 0.26	1.04 ± 0.13
J	1.02 ± 0.32	1.05 ± 0.19
H	1.02 ± 0.26	1.08 ± 0.25
K	1.06 ± 0.34	1.09 ± 0.36
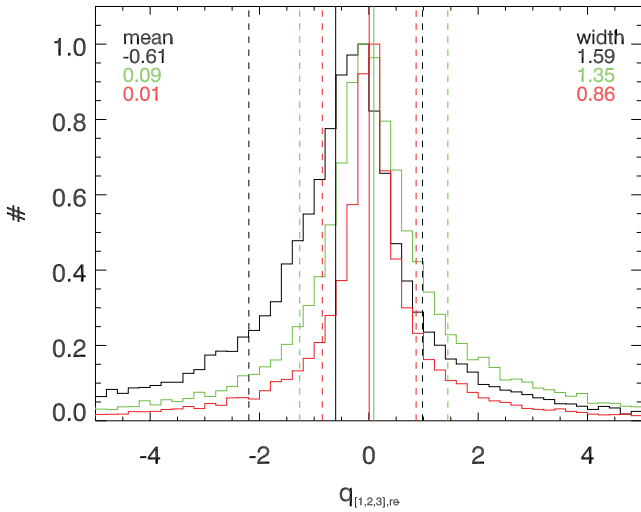
Figure 20. Histogram of the Chebyshev coefficients describing the wavelength dependence of r_e: q_1 (black), q_2 (green) and q_3 (red), obtained from GALFITM multiband fits to our simulated data set. The mean and rms scatter of each distribution are indicated by vertical solid and dashed lines, respectively, and the values printed in the corners of the figure. Histograms have been normalized to unit maximum. As expected, the distribution of q_3 in our simulated sample is narrower than the distribution of q_2.

required set up time should generally be the same. However, for the multiband method not all steps in the code are repeated for all bands; e.g. deblending/masking decisions are common for all bands and only decided once, whereas Mode_S1 makes these decisions on each band independently. Some further optimization of this part of GALAPAGOS-2 is also possible in the future.

When comparing the pure fitting time for the simulated objects, we find that the multiband fits are in fact slower than the nine individual band fits combined. The top panel of Fig. 22 shows a histogram of the overall fitting time for a small subset of objects for which we have all nine individual band fits, and for which such a comparison is possible. The fitting time will depend on how many secondary objects with free parameters, i.e. those fainter than the primary, are included in the fits. The number of secondaries depends upon the deblending, and is greater for multiband detection. To compare fitting times fairly, we therefore plot results for Mode_S2 and Mode_M. While the combined single-band fits take around 74 s per object, the multiband fits take about 106 s per object.

The most time consuming part of the GALFITM algorithm is producing the model derivatives, which describe how the model images
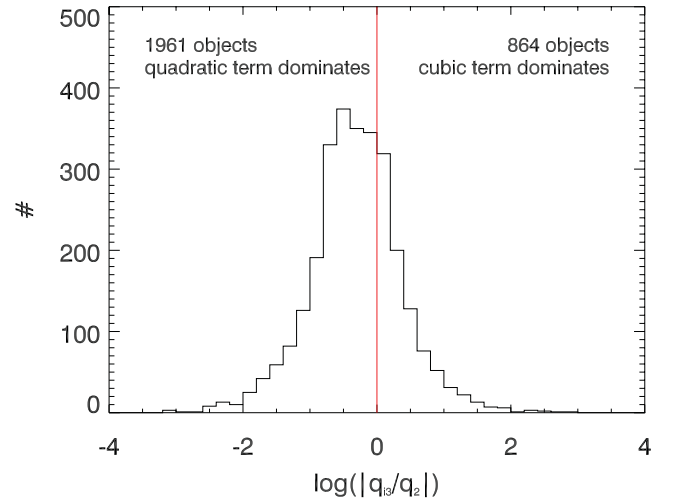

Figure 21. Histogram of $\log(|q_3/q_2|)$ for galaxies with $\mathrm{mag}_{sim} < 19.8$. This figure compares the importance of the second-order and third-order terms of the Chebyshev polynomials for r_e. As the simulations were done to second-order specifications, one would expect to see that the second-order term dominates in most cases. The histogram is clearly offset to the left, confirmed by the values printed in the figure, which give the numbers either side of zero.

would change for small variations in each of the parameters. The derivatives must be calculated for every pixel and convolved with the PSF, which is an expensive operation. The LM algorithm requires these derivative images, one set for each band being used in the fit, to be calculated with respect to each parameter, at every iteration step. We would therefore naively assume that the fitting time per iteration should be roughly proportional to the number of free parameters.

For instance, a single-band, single-Sérsic fit has seven free parameters (magnitude, x-centre, y-centre, half-light radius, Sérsic index, axis ratio and position angle), and hence seven derivative images must be calculated by GALFITM each iteration. However, this is done independently for the nine input images. The multiband fits carried out for this work use 19 free parameters (nine for magnitude, one x-centre, one y-centre, three for half-light radius, three for Sérsic index, one position angle and one axis ratio), and derivatives must be calculated for nine bands. Hence, $19 \times 9 = 171$ derivatives must to be calculated for each iteration. By this estimate, each multiband iteration should take $171/7 \approx 24$ times longer than each single-band iteration (this factor should be the same for any number of secondary objects included in the fit). In reality, from the middle panel of Fig. 22, we see that the difference is somewhat less: a factor of $\sim$13. This is probably because the derivatives of higher order Chebyshev parameters are less expensive to calculate than the zeroth-order parameters and, similarly, the standard parameters in single-band fitting.

When one accounts for the fact that the single-band fit must be run for each of the bands, the multiband method gains by a factor of 9. If the number of iterations required for each method were the same, the multiband method would take 13/9 times as long and hence would be $\sim$40 per cent slower. Indeed, the number of iterations required for each fit are very similar, with the single-band approach requiring about nine times more iterations, as the fit must be performed for each band (as shown in the lower panel of Fig. 22). For these bright galaxies, with complete sets of single-band fits, the multiband method therefore takes roughly 40 per cent more fitting time as compared to the Mode_S2 single-band fits. Note that, for
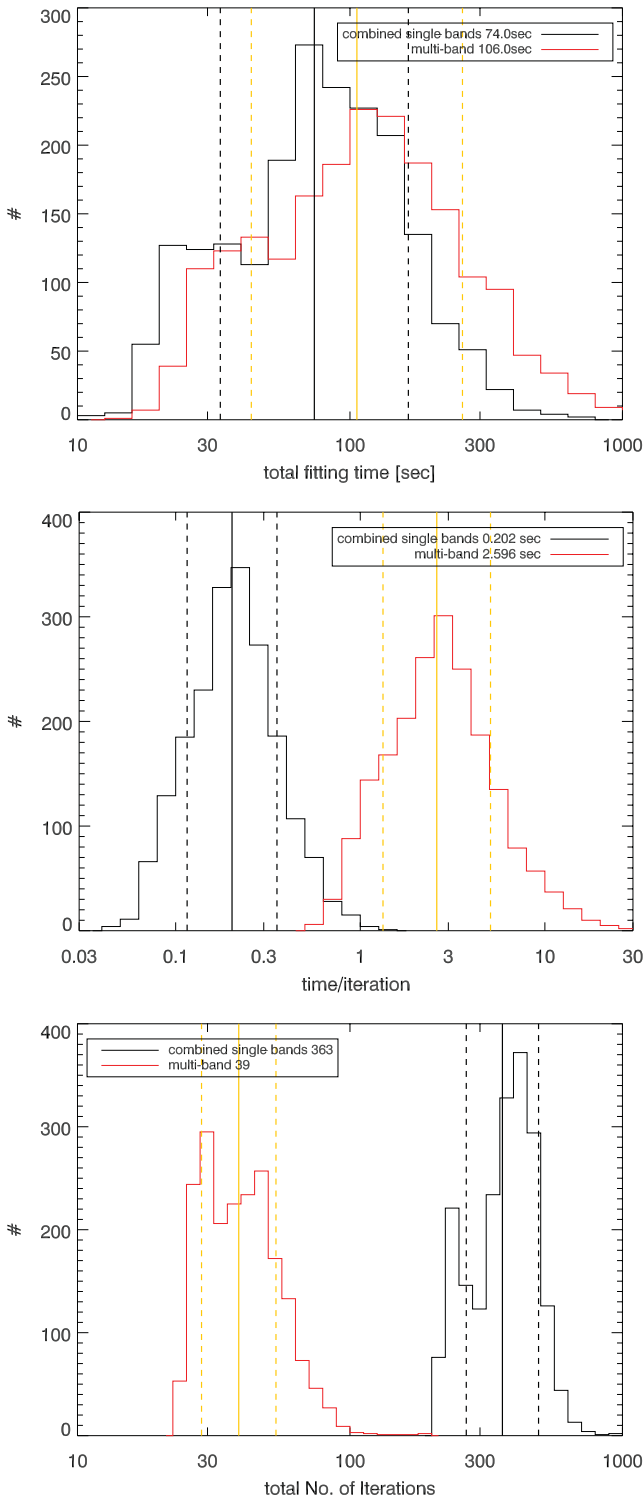
Figure 22. CPU time histograms. The red histograms represent times for Mode_M fitting, the black histograms give the sum of the times for the nine Mode_S1 fits. This figure only contains values from objects where all nine Mode_S2 and Mode_M fits exist, to allow a fair comparison between the methods. The vertical lines show the mean and rms scatter for both histograms. The top panel shows the total fitting time as returned by GALFITM. Multiband fits take longer than single-band fits. The main reason for this is seen in the second panel, every individual iteration takes substantially longer in Mode_M compared to Mode_S2. This effect is nearly, but not entirely, cancelled out by the smaller total number of iterations needed to derive all nine band fits (lower panel).

single-band detection, the number of secondaries that are fitted is reduced, and hence the combined time of the Mode_S1 fits take only ∼39 s compared to ∼81 s for the same sample of galaxies in Mode_M. The multiband Mode_M method therefore takes roughly twice the time of Mode_S1.

The number of successfully fitted objects is much higher in the case of multiband fitting (see Table 3). From the above arguments, this should result in a much larger number of galaxies with a complete set of multiband measurements per unit processing time. However, the above speed comparisons are limited to the cases where we obtain successful fits in all nine single-band fits and the multiband fit. For these, the number of iterations are similar, but for the majority of galaxies, with lower S/N, the single-band fits (many of which fail) appear to require significantly fewer iterations than the multiband fits. To get an overall impression of the speed of single- versus multiband, we divide the number of galaxies with a complete set of multiband measurements by the total time taken to fit the entire sample, to produce a 'complete success' rate. For Mode_S2 this is ∼2.4 'complete successes' per hour (if one requires all *ugrizY JHK* band values; 23.5 requiring just the *griYHK* bands), while for Mode_M it is 29.3 'complete successes' per hour (full *ugrizY JHK*). In single-band fitting, much more CPU time is spent on objects that are later discarded as unreliable by the cleaning process. So in terms of useful fits per unit time, multiband fitting compares very favourably.

6.2 Storage requirements

Another practical aspect to take into account, especially for large data sets, is the disc space used. If a data set uses less disc space it is easier to handle and less space will be needed for big surveys. For the sample of 29 205 real objects, we use

(i) 51 GB for the Mode_M fitting,

(ii) 78 GB for the Mode_S1 fitting. The difference is largely down to having SEXTRACTOR files for each band instead of one set for the whole process. In comparison, the single-band fitting does save some disc space because not as many galaxy postage stamps have to be made for the individual bands as less objects are detected.

(iii) In Mode_S2, cutting all postage stamps when running the object detection on a multiwavelength image increases the disc space required to a total of 100 GB, so a reduction of disc space ∼50 per cent is achieved when changing from single-band to multiband fitting.

Multiwavelength fitting has the smallest space-to-result ratio, especially when taking into account that one gets usable results for a much bigger sample. We get valid results (fits that did not run into fitting constraints) for 15 566 objects, compared to 209 galaxies with valid fits in *u* band, and 3276 (*g* band), 5802 (*r* band), 6804 (*i* band), 2117 (*z* band), 3912 (*Y* band), 2530 (*J* band), 5432 (*H* band) and 5190 (*K* band), respectively. The overlap of all these samples is a mere 87 galaxies (or 992 when only *griYHK* are taken into account).

For the set of simulated galaxies, we find a similar result: For a total of 42 229 simulated objects, the disc space needed is

(i) 64 GB for Mode_M fitting,

(ii) 73 GB for Mode_S1 fitting,

(iii) 114 GB for Mode_S2 fitting.

Object numbers with useful values here are: 714 (*u* band), 6022 (*g* band), 10 362 (*r* band), 12 326 (*i* band), 4139 (*z* band), 9627 (*Y* band), 7965 (*J* band), 12 593 (*H* band) and 12 602 (*K* band) with

an overlap of 305 objects (2560 objects). This compares to 23 632 objects for which we get a valid result in all bands when using multiband fitting. Overall, our multiband fitting procedure can help to save nearly 50 per cent of disc space required.

7 COLOUR–MAGNITUDE DIAGRAM FROM MULTIBAND FITTING

The multiwavelength Mode_M technique that we have presented and tested, both above and in accompanying MegaMorph papers, has subsequently been applied to a larger sample of galaxies from the GAMA survey. Here we use this sample to present preliminary CMD and size–magnitude diagram. This is done for two purposes: as a consistency check of the fitting results, and to demonstrate where the multiband technique offers scope for quickly improving science results.

Single-band single-Sérsic fits, in *ugrizYJHK*, have been performed by K12 for all spectroscopic targets in the GAMA sample, using their own code, SIGMA, to run GALFIT3. However, a detailed comparison between our single-band fits and those conducted in K12 is beyond the scope of this paper. We therefore decided that comparing their single-band fitting results to our multiband results could potentially lead to wrong conclusions regarding single- versus multiband fitting, due to the use of different wrapper scripts. However, in earlier tests, we have established that both procedures, SIGMA (K12) and our own method based on GALAPAGOS (Barden et al. 2012) generally return very similar results when used on single-band data, and comparable values when used on multiband data in our setup. In order to show the strength of our code, we avoid using any additional information about the objects other than GALAPAGOS fitting results and spectroscopic redshifts. The latter are provided by GAMA, and used only to calculate physically meaningful parameters such as absolute magnitudes and sizes, for both our single- and multiband fitting results. For these transformations, a cosmological model of $\Omega_\Lambda = 0.7$, $\Omega_m = 0.3$ and $H_0 = 70\,h_{70}\,\mathrm{km\,s^{-1}\,Mpc^{-1}}$ is assumed.

In Section 4, we have carried out both single- and multiband fits on a small subarea of the GAMA survey field. Compared to the GALAPAGOS version used and tested above, we use a minimally changed version in this section. The main change was the introduction of a feature that allows the code to only target certain objects instead of targeting all detections in a survey. For this section, we applied (using Mode_M) multiband version of GALAPAGOS-2 and GALFITM to all objects that have both full wavelength coverage in the GAMA 9 h (G09) field and redshifts provided by the GAMA team (Driver et al. 2011; Liske, in preparation). Additionally, we include all objects within 66 arcsec ($\sim$200 pixels) to one of these GAMA objects and brighter than the said object, as GALAPAGOS works on objects in brightness order from bright to faint.[11] A good fraction of these neighbouring objects are bright stars. Given the brightness of the objects targeted, this slightly changed code should not influence fitting results significantly but allows the code to only target 144 261 objects instead of the total 1401 969 detections in the field, reducing the sample size by $\sim$90 per cent and saving a huge amount of fitting time.

Of these 144 261 objects, we have spectroscopic redshifts for 43 617 objects. GALAPAGOS returned a result for 43 572 (99.9 per cent), and 33 696 (77.3 per cent) have useful fits and a full set of multiwavelength parameters is provided. The fraction of galaxies with valid fits is significantly higher in this sample of galaxies compared to the samples used earlier in this paper (e.g. the left part of Table 2), mostly because for this section bright galaxies – that are potentially easier to fit – have been primarily targeted, whereas in the previous sections, we had targeted all detected objects. Also, as stars have no redshifts assigned, they are removed when deriving these numbers, boosting the success rate.

The resulting catalogue of this procedure is used in both Vulcani et al (in preparation) and this section, in which we briefly examine the CMD of galaxies.

In Fig. 23, we show $g-i$ versus M_i CMDs as they would be recovered by the different techniques, colour coded by Sérsic index n_z. The top-left panel shows values from aperture photometry, for which we use matched-aperture photometry obtained in a manner similar to Hill et al. (2011) and to be described in Liske et al. (in preparation). The points in this panel have not been colour coded as this information would have to be provided by a second code, aperture photometry itself does not give an estimate for galaxy 'morphology'. The top-right figure shows the CMD as given entirely by Mode_S1 fitting, e.g. the colour coding according to n_z as provided by single-band fitting. High-n and low-n galaxies show mixed colours in this figure, a separation, although indicated, is weak. The bottom-left figure shows the same single-band values, but colour coded using multiband n_z. In this figure, the separation between low-n and high-n galaxies is better. The reader should keep in mind that Sérsic index is not a robust value to be used for classifying galaxies in a morphological sense, especially early-type galaxies are known to show a wide range of Sérsic indices, e.g. they are following a magnitude–n relation (see e.g. Graham 2011). Additionally, Sérsic indices are sensitive to measurement errors. For example, a faint AGN or bright star cluster in the centre of a galaxy would boost n to show a high value instead of the intrinsic value of the underlying host galaxy. We use n_z only as a very crude estimator in this analysis and would strongly discourage users to use it for more than that. Especially, it cannot replace a visual classification of morphology.

In the bottom-right panel of the figure, we show the CMD as recovered entirely by multiband fitting. The division between low-n and high-n galaxies becomes much stronger, and the scatter in the figure gets reduced, with high-n galaxies showing significantly redder colours than low-n galaxies. This is expected by simple morphology–stellar-population arguments. It should be stated here that galaxies are plotted in random order, not by increasing Sérsic index, the lack of blue points on the red sequence and red points in the blue cloud, even when using n_z as colour index, is real and not due to plotting procedure.

Please note that the number of points in the single-band panels (727 objects) is only slightly smaller than the one in the multiband panel (795 objects). This is true as long as no u- or z-band data is used and only bright galaxies which were targeted for spectroscopic redshifts are considered ($m_r < 19.8$). Given that this completeness effect has already been discussed in detail above, we decided to not use u- or z-band data here, although it might show a better separation of the red sequence and the blue cloud. Instead, we concentrate on the fitting accuracy itself.

Given the overall shape of this figure, it should be emphasized that this figure shows purely observed colours, e.g. no k-corrections or dust-corrections have been applied. The main reason for this

---

[11] During the development of the code, it proved useful for fitting stability if results for brighter neighbouring objects are already known at the time they have to be used as neighbours. This issue is discussed in detail in Barden et al. (2012).
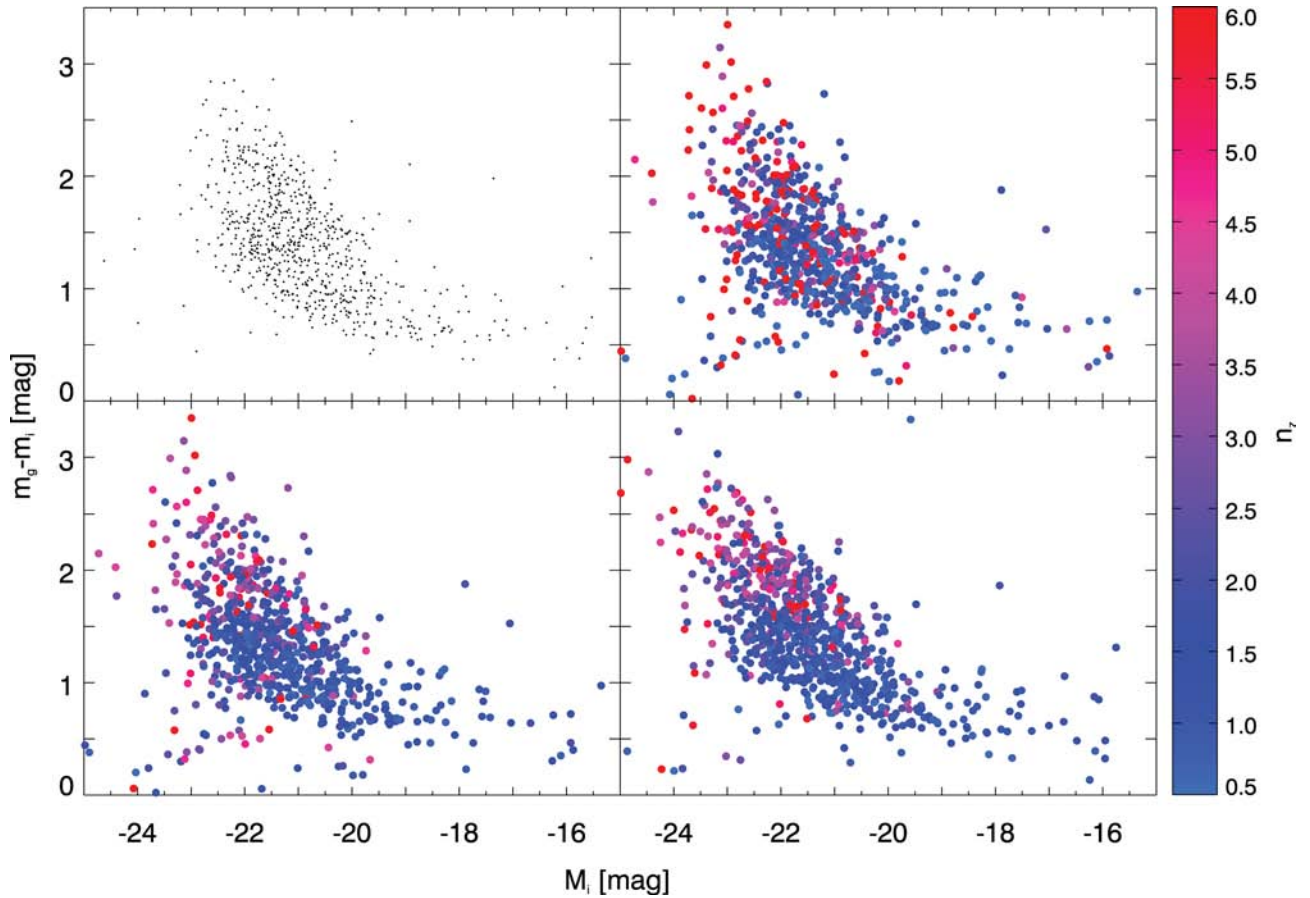
Figure 23. Colour–magnitude diagram (*y*-axis shows purely observed colours). Top-left: when using aperture photometry (GAMA SEXTRACTOR *mag_auto* from catalogue ApMatchedCatv03); top-right: when using single-band fitting (Mode_S1), colour-coding using single-band n_z values; bottom-left: Mode_S1 fitting results, colour coding using Mode_M n_z values. Bottom-right: using only Mode_M multiband fitting, colour coded by *z*-band Sérsic index from multiband fitting [blue=low (<0.5), red=high (>6)]. n_z is assumed to be the best separator and we argue in this paper for multiband to be a more reliable value than single-band Sérsic indices. A separation between 'early-type' (high-*n*) and 'late-type' (low-*n*) galaxies becomes much clearer when Mode_M n_z values are used for colour coding. Please be reminded that the number of points in this analysis is mostly defined by the number of redshifts available, and *not* by the number of successful fits. As a consequence, single- and multiband figures contain a very similar number of points.

is that we want to show the difference between the techniques, not sample sizes. Robust *k*-corrections would require magnitude measurements in many bands which are automatically provided by multiband fitting. Single-band fitting, however, can produce results in some bands, not in the others, providing reliable *k*-correction only for a subset of galaxies. We will apply *k*-correction to all multiband fits in Fig. 24.

In Fig. 24, we show the CMD for the 28 737 GAMA galaxies in the G09 field for which we were able to recover useful fitting values using multiband fitting procedures (Mode_M). In contrast to Fig. 23, values in this figure have been *k*-corrected to show rest-frame values, using KCORRECT (Blanton & Roweis 2007), version 4_2. This is possible here because the multiband fitting procedure returns magnitudes for all *ugrizYJHK* bands, whereas any single-band routine could have some magnitude values missing in certain bands, making *k*-correction both harder and less accurate. The middle panel shows contours of the same distribution for all objects. An indication for a bimodality and galaxy separation can be seen. The right-hand panel shows the same, but galaxies have been split up into broad n_z-value bins, each with a large number of galaxies (7000–12 000 galaxies), in order to show the separation between the different Sérsic index populations more clearly. The bimodality becomes very visible here, although the red sequence is not as

tight as one would hope when a clean classification scheme is used instead of n_z values.

A few remarks should be made on these findings as follows.

(i) The solid line in the rightmost panel of Fig. 24 indicates not a fit to a red sequence, but a separator, a fit to the 'green valley', as determined by Gavazzi et al. (2010) from a sample of 4100 galaxies using visual classification. Gavazzi et al. (2010) use SDSS DR7 Petrosian magnitudes for their analysis. Due to the nature of these – the *r* band alone defines the size of the aperture in which the magnitude is measured – we would expect a widening of our red sequence due to the ability of our method to vary galaxy size with wavelength, hence measuring a slightly different magnitude at other wavelengths than the ones provided by Gavazzi et al. (2010). We argue that our magnitudes more closely resemble the true magnitudes at these wavelengths in comparison with SDSS Petrosian magnitudes which should be bulge dominated given that the aperture size is defined in a reddish (*r*) band (please also see Graham et al. 2005). Unfortunately for this comparison, this bulge domination of the magnitudes measured helps to get a tight colour–magnitude relation and a better separation from the blue cloud.

(ii) It is very interesting to see that the contours for galaxies with intermediate n_z (1.5 < *n* < 3; shown in green) seem to have a peak
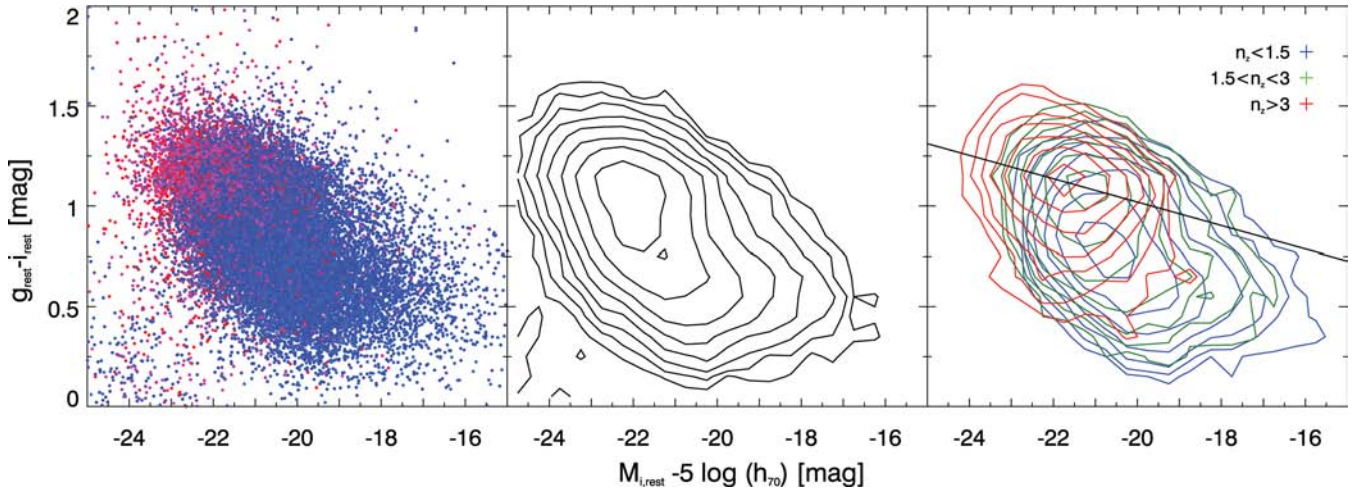
Figure 24. Colour–magnitude diagram (both axes rest frame and *k*-corrected). Left: all GAMA G09 galaxies with redshifts; middle: contours for all galaxies in the left figure; right: contours for samples split by Sérsic index. The points are colour coded by *z*-band Sérsic index [blue=low (<0.5), red=high (>6)]. A clear separation between low-*n* and high-*n* galaxies is visible (please note that the points are plotted in random order, not by increasing Sérsic index), especially when plotting three *n* bins ($n < 1.5$, $1.5 < n < 3$, $4 < n$) as contours (right figure). Even in the contours for all galaxies (Center), the shape of the contours indicate two overlapping sequences, which is what one expects. The solid line in the right figure indicates a separator between the red sequence and the blue cloud as empirically determined by Gavazzi et al. (2010).
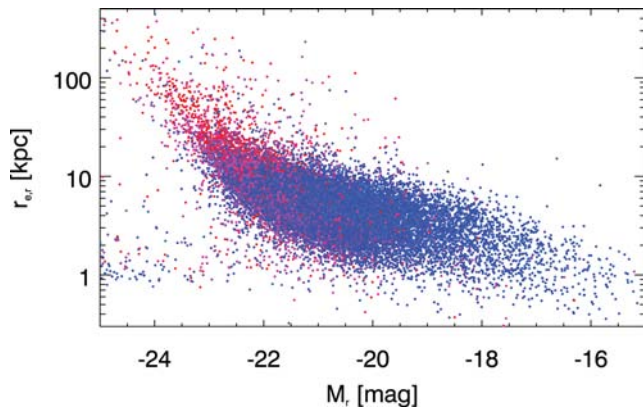
Figure 25. Magnitude–size relation. The points are colour coded by n_z matching the previous figure (blue=low (<0.5), red=high (>6)). As discussed in the text, there is a visible population of very bright galaxies with increased n_z and very small sizes, visible as a cloud of red points at the lower-left edge of the cloud of blue points.

on the red sequence and a long 'tail' towards the blue cloud. This is exactly what would be expected for a transition population.

(iii) Our galaxy 'separator' n_z should only give a very rough estimation of the galaxy 'morphology' as it is easily biased and boosted by central light sources such as faint AGN and/or bright star clusters. Hence the high-*n* sample will include some of these objects, although they would visually be classified as discs, suggesting a place in or closer to the blue cloud. A way to test this hypothesis is to look at the magnitude–size relation of all objects. When a single-Sérsic profile is used to fit an object which contains both a disc and a point source, one would expect to fit both a high Sérsic index and a small size, as well as a bright magnitude as this would include the flux of the nuclear source. When plotting the magnitude–size relation of all the objects in our sample (see Fig. 25), we can see that indeed many of these high-*n* galaxies are the brightest and smallest galaxies, seen as a purple/red cloud of points, in what

would traditionally be called the 'blue cloud' of disc-dominated galaxies.

(iv) Even using perfect classifications, one would always find both blue ellipticals in the blue cloud and discs that show red colours given their dust properties and possibly seen edge-on (e.g. Wolf et al. 2009; Rowlands et al. 2012). An entirely clean separation is impossible to achieve.

(v) Please again bear in mind that no other correction (e.g. for dust content) than *k*-correction has been applied to any of the values in Fig. 24. This preliminary analysis is intended only as a demonstration of the advantages of multiband fitting.

Our simple analysis, using no other information than redshifts and colours as directly measured by our multiband fitting code, clearly shows the known separation between the red sequence and the blue cloud of galaxies, even when using a crude and inaccurate proxy for 'galaxy morphology' such as Sérsic index n_z. Although a separation of the two galaxy populations by using Sérsic index as a 'classifier' will never be ideal, it proves a powerful statistical tool in this example.

We assume that most of the outliers in Fig. 24 are due to an unflagged error/uncertainty in our fitting pipeline and our quick and rough analysis. Especially, we are not (yet) running bulge–disk decomposition on our data, and fitting single-Sérsic profiles to B/D composite galaxies is known to be non-ideal. We assume that the fitting process went wrong in these examples in a way that we were unable to detect in a simple automated fashion. Statistically, these ∼100–200 outliers become insignificant in a sample of 28 737 galaxies.

8 SUMMARY

In this paper, we have presented new versions of both GALFIT (which we call GALFITM) and GALAPAGOS (GALAPAGOS-2) to automate the process of fitting two-dimensional, single-Sérsic models to large samples of galaxies. Our novel approach uses multiple images taken at different wavelengths simultaneously, instead of single-band data, as used by the current published versions of these codes. We have

tested our multiband modifications extensively, both on real and simulated data and compared their performance to the single-band versions of the codes. For real data, we have selected nine-band (*ugrizY JHK*) data from the GAMA survey (Driver et al. 2011). Simulations were created following H07 to largely reproduce the parameter distributions of the real data. This creates a data set as realistic as necessary, while taking out the issues of image confusion by nearby stars and internal galaxy structure, as well as providing a truth value for comparison against those recovered by the fitting process.

From both real and simulated data, we can draw very similar conclusions.

(i) Multiband fitting significantly improves the recovery of galaxy magnitudes, at least in the lower S/N bands (particularly *u* and *z* band in this analysis, see e.g. Fig. 10 and Table 4). The improvement for both sizes (see e.g. Fig. 14 and Table 5) and Sérsic indices (see e.g. Fig. 17 and Table 6) is significant over the entire wavelength range tested in this paper. The multiband approach returns more accurate results than treating the bands independently, and is able to make useful measurements for very faint galaxies. In our analysis, multiband fitting is able to derive reliable values for ∼75 times more galaxies in SDSS *u*-band data than the single-band approach.

(ii) The multiband version of our code is more stable, in terms of providing fitting results for objects where single-band fits fail to return a result. This is because the single-band fits occasionally return results which are affected by the constraints that are provided by GALAPAGOS and used by GALFITM during the fitting process. GALFITM more frequently returns valid results when multiband data are used. This is always the case for real galaxy images, while in our simulations this is true when fits in several bands are required, e.g. for SED modelling.

(iii) Physically meaningful variations of galaxy parameters with observed wavelength are used in the fitting method presented in this paper. They enable accurate wavelength interpolation, useful to derive rest-frame galaxy parameters, and provide the user with a full set of parameters at all wavelengths. Single-band fits on the other hand are more likely to fail in at least individual bands, while returning a result in other wavelengths, thus leaving a less complete sample from which to interpolate values.

(iv) While running single-band fits returns more or less equivalent results for bright galaxies, multiband fitting provides a more homogenous data set as decisions about object detection, deblending and masking are necessarily the same. Single-band fits can vary these decisions between different bands.

(v) In addition to providing results for a higher fraction of galaxies, the multiband code can be run on fainter objects, as the object detection can be sensibly carried out on a co-added image. The number of galaxies that can be used for scientific purposes is increased by a factor of ∼2 if only single-band values are needed, up to ∼16 if multiband data (*griYHK*) values are required – a factor of ∼180 is achieved when a full set of parameters in *ugrizY JHK* data are needed.

Overall, we conclude that using multiband fitting instead of single-band fitting improves both quality and quantity of galaxy fits on survey data. It therefore provides an excellent tool for modern surveys and enables a step forward in many areas of astronomy, especially where sample size and magnitude constraints limit current work.

9 PROSPECTS

In this paper, we have exclusively tested GALFITM and GALAPAGOS-2 on single-Sérsic profiles. Further plans most importantly include implementation of bulge–disc decomposition into GALAPAGOS-2. As some of the conclusions in this paper might change due to both the additional flexibility and the more challenging fits even on bright objects, we will discuss these changes in detail in a follow-up paper. The intention is to separate galaxy bulges and discs more accurately than previously possible by using the information provided by the different colours of the respective components.

The colour gradients (variations of *n* and r_e with wavelength) seen in this paper come from a combination of both mixing the bulge and disc stellar populations when fitting them with a single-Sérsic profile and the effects of dust (e.g. Möllenhoff et al. 2006; Pastrav et al. 2012). Fully understanding the observed trends will require careful consideration of both multiwavelength bulge–disc decompositions and spatially resolved models of dust attenuation (e.g. Popescu et al. 2011), constrained by spaceborne UV and FIR/submm photometry.

Another issue, which we have tried to encompass by testing with both real and simulated data in this work, but which has otherwise been neglected, is the performance of multiband GALFITM (and profile fitting in general) in the presence of morphological features, such as bars and spiral arms. We aim to investigate this in future by drawing on the data and resources of Galaxy Zoo (Lintott et al. 2011; Masters et al. 2011)

Although GALFITM already supports multiple components, an adapted version of GALAPAGOS-2 will be needed for this work. This version will be presented in a different paper (Häußler et al., in preparation). It is currently under development and testing, and we aim for it to be ready for public release in ∼6 months. We will publish our codes and tools in a follow-up paper when bulge–disc decomposition is successfully incorporated into the code and encourage astronomers to use these tools on their data.

REFERENCES

Abramowitz M., Stegun I., 1965, Applied mathematics series: Handbook of Mathematical Functions: With Formulas, Graphs, and Mathematical Tables. Dover Publications

Allen P. D., Driver S. P., Graham A. W., Cameron E., Liske J., de Propris R., 2006, MNRAS, 371, 2

Barden M., Häußler B., Peng C. Y., McIntosh D. H., Guo Y., 2012, MNRAS, 422, 449

Bell E. F., de Jong R. S., 2000, MNRAS, 312, 497

Bertin E., Arnouts S., 1996, A&AS, 117, 393

Bertin E., Mellier Y., Radovich M., Missonnier G., Didelon P., Morin B., 2002, in Bohlender D. A., Durand D., Handley T. H., eds, ASP Conf. Ser. Vol. 281, The TERAPIX Pipeline. Astron. Soc. Pac., San Francisco, p. 228

Blanton M. R., Roweis S., 2007, AJ, 133, 734

Conselice C. J., 2003, ApJS, 147, 1

de Souza R. E., Gadotti D. A., dos Anjos S., 2004, ApJS, 153, 411

de Vaucouleurs G., 1948, Ann. Astrophys., 11, 247

Driver S. P., Popescu C. C., Tuffs R. J., Liske J., Graham A. W., Allen P. D., de Propris R., 2007, MNRAS, 379, 1022

Driver S. P. et al., 2011, MNRAS, 413, 971

Gavazzi G., Fumagalli M., Cucciati O., Boselli A., 2010, A&A, 517, A73

Gonzalez-Perez V., Castander F. J., Kauffmann G., 2011, MNRAS, 411, 1151

Graham A. W., 2011, arXiv:1108.0997

Graham A. W., Driver S. P., 2005, PASA, 22, 118

Graham A. W., Driver S. P., Petrosian V., Conselice C. J., Bershady M. A., Crawford S. M., Goto T., 2005, AJ, 130, 1535

Häußler B. et al., 2007, ApJS, 172, 615 (H07)

Hill D. T. et al., 2011, MNRAS, 412, 765

Kelvin L. S. et al., 2012, MNRAS, 421, 1007 (K12)

La Barbera F., de Carvalho R. R., 2009, ApJ, 699, L76

La Barbera F., de Carvalho R. R., Kohl-Moreira J. L., Gal R. R., Soares-Santos M., Capaccioli M., Santos R., Sant'anna N., 2008, PASP, 120, 681

La Barbera F., de Carvalho R. R., de La Rosa I. G., Lopes P. A. A., Kohl-Moreira J. L., Capelato H. V., 2010, MNRAS, 408, 1313

Lackner C. N., Gunn J. E., 2012, MNRAS, 421, 2277

Lawrence A. et al., 2007, MNRAS, 379, 1599

Lilly S. et al., 1998, ApJ, 500, 75

Lintott C. J. et al., 2008, MNRAS, 389, 1179

Lintott C. et al., 2011, MNRAS, 410, 166

MacArthur L. A., Courteau S., Bell E., Holtzman J. A., 2004, ApJS, 152, 175

Masters K. L. et al., 2010, MNRAS, 404, 792

Masters K. L. et al., 2011, MNRAS, 411, 2026

Möllenhoff C., Popescu C. C., Tuffs R. J., 2006, A&A, 456, 941

Pastrav B. A., Popescu C. C., Tuffs R. J., Sansom A. E., 2012, in Tuffs R. J., Popescu C. C., eds, Proc. IAU Symp. 284, Dust effects on the derived Sérsic indexes of disks and bulges in spiral galaxies. p. 306

Peng C. Y., Ho L. C., Impey C. D., Rix H., 2002, AJ, 124, 266

Peng C. Y., Ho L. C., Impey C. D., Rix H.-W., 2010, AJ, 139, 2097

Pignatelli E., Fasano G., Cassata P., 2006, A&A, 446, 373

Popescu C. C., Tuffs R. J., Dopita M. A., Fischera J., Kylafis N. D., Madore B. F., 2011, A&A, 527, A109

Rowlands K. et al., 2012, MNRAS, 419, 2545

Schade D., Barrientos L. F., Lopez-Cruz O., 1997, ApJ, 477, L17

Sérsic J. L., 1968, Atlas de galaxias australes. Observatorio Astronomico, Cordoba, Argentina

Simard L., 1998, in Albrecht R., Hook R. N., Bushouse H. A., eds, ASP Conf. Ser. Vol. 145, Astronomical Data Analysis Software and Systems VII GIM2D: an IRAF package for the Quantitative Morphology Analysis of Distant Galaxies. Astron. Soc. Pac., San Francisco, p. 108

Simard L. et al., 2002, ApJS, 142, 1

Simard L., Mendel J. T., Patton D. R., Ellison S. L., McConnachie A. W., 2011, ApJS, 196, 11

Strateva I. et al., 2001, AJ, 122, 1861

Suh H., Jeong H., Oh K., Yi S. K., Ferreras I., Schawinski K., 2010, ApJS, 187, 374

Szalay A. S., Connolly A. J., Szokoly G. P., 1999, AJ, 117, 68

Tasca L. A. M., White S. D. M., 2011, A&A, 530, A106

Tortora C., Napolitano N. R., Cardone V. F., Capaccioli M., Jetzer P., Molinaro R., 2010, MNRAS, 407, 144

Vika M., Driver S. P., Cameron E., Kelvin L., Robotham A., 2012, MNRAS, 419, 2264

White S. D. M. et al., 2005, A&A, 444, 365

Wolf C. et al., 2009, MNRAS, 393, 1302

York D. G. et al., 2000, AJ, 120, 1579

APPENDIX A: EXAMPLE IMAGES AND FIT RESULTS

In this appendix, we show some sample images of simulated galaxies, their fitting models (if applicable) and their fitting residuals in all nine bands for both multiband and single-band fitting. These galaxies are not randomly chosen, but rather chosen to show typical difficulties and effects that separate single-band and multiband fitting. In particular, the objects shown are the same objects shown in Figs 2 and 9.
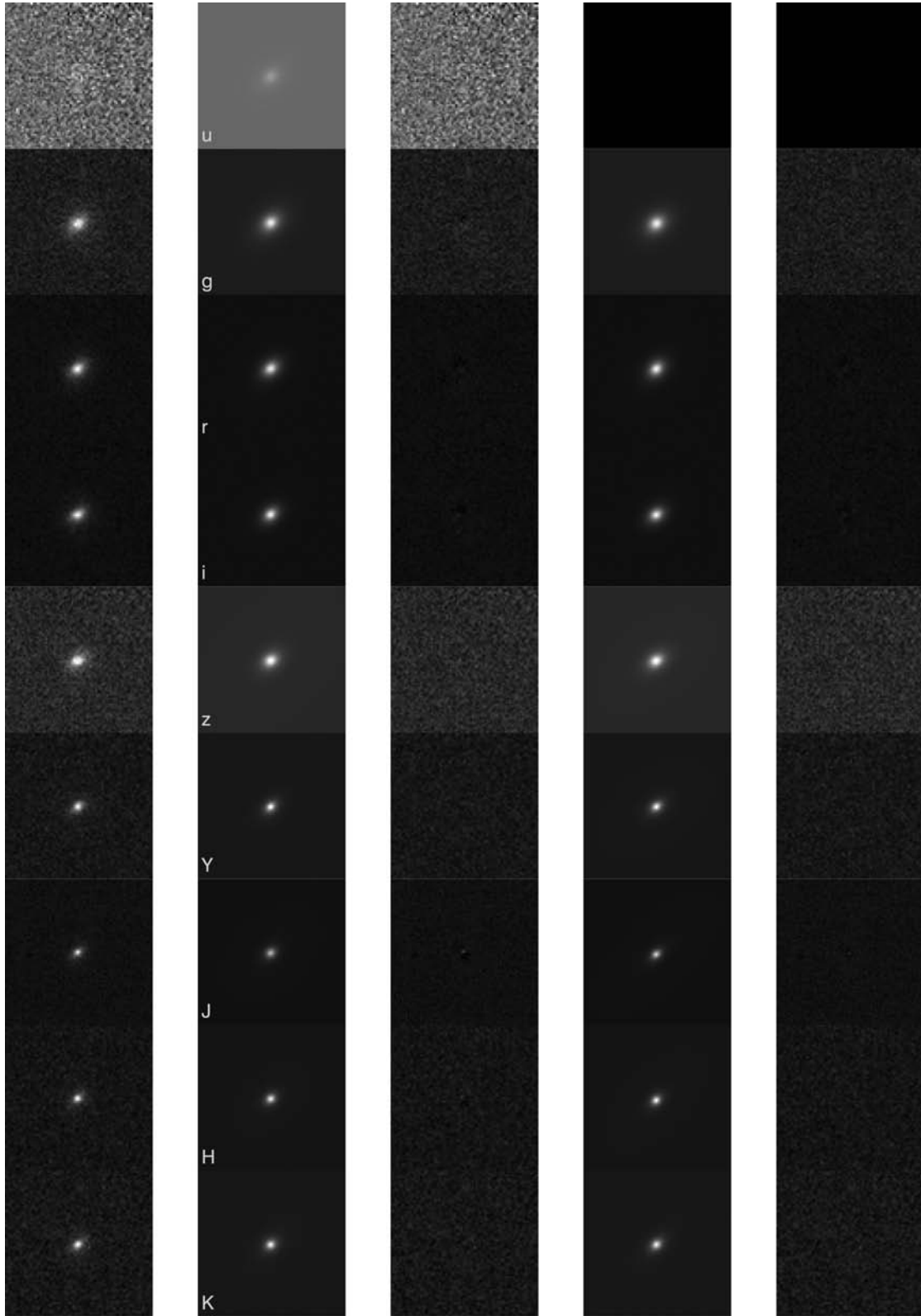
Figure A1. Example real object. From left to right: input image, model and residual multiband fit, model and residual single-band fit. The black images in the case of single-band fitting indicate where no GALFITM results exist (while ignoring constraints and cleaning of the catalogue).
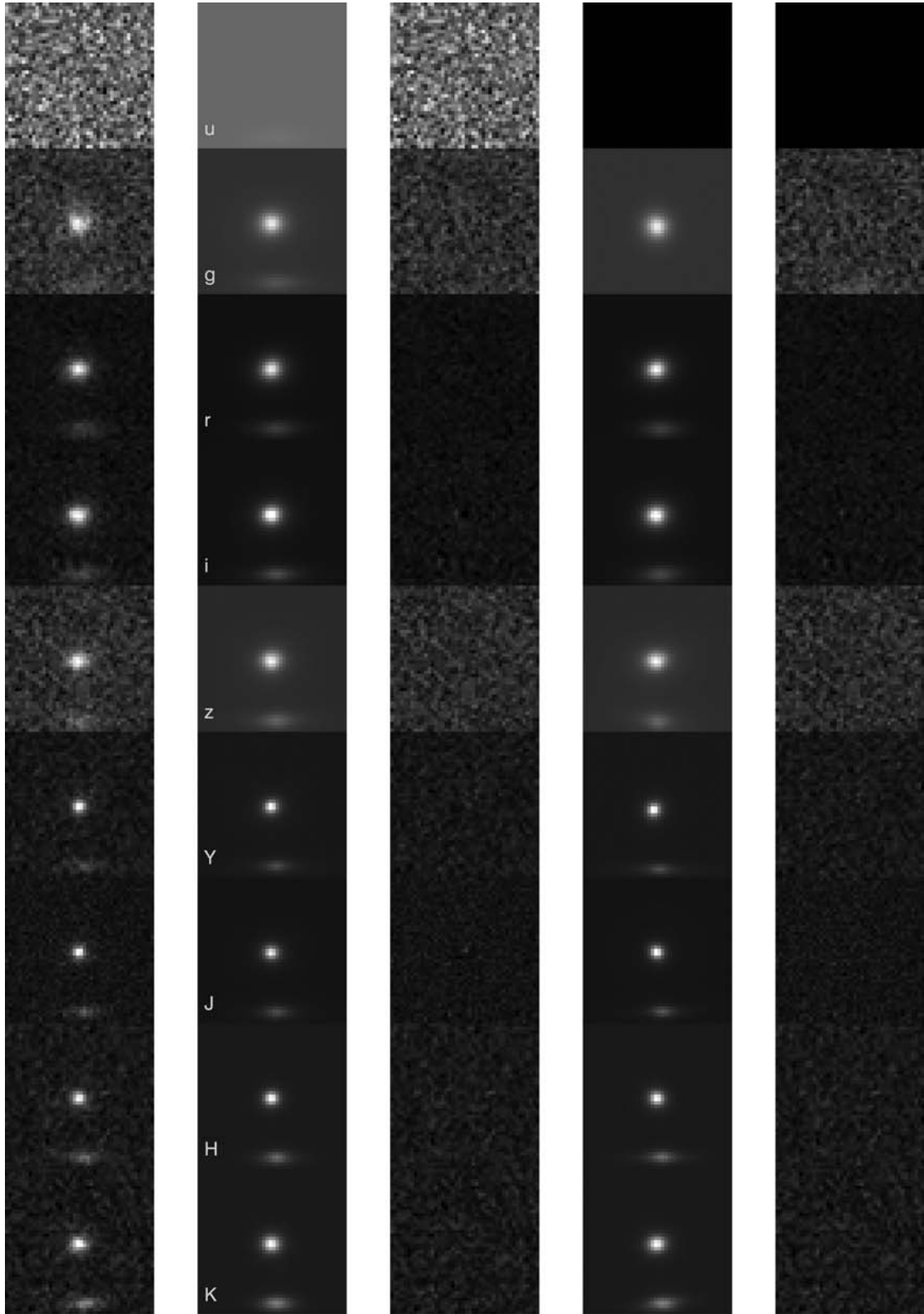
Figure A2. Example real object, similar to Fig. A1: This example shows a galaxy that has not been detected in single-band *u*-band. The neighbouring galaxy has also not been detected in the single-band *g*-band, potentially biasing the fit.
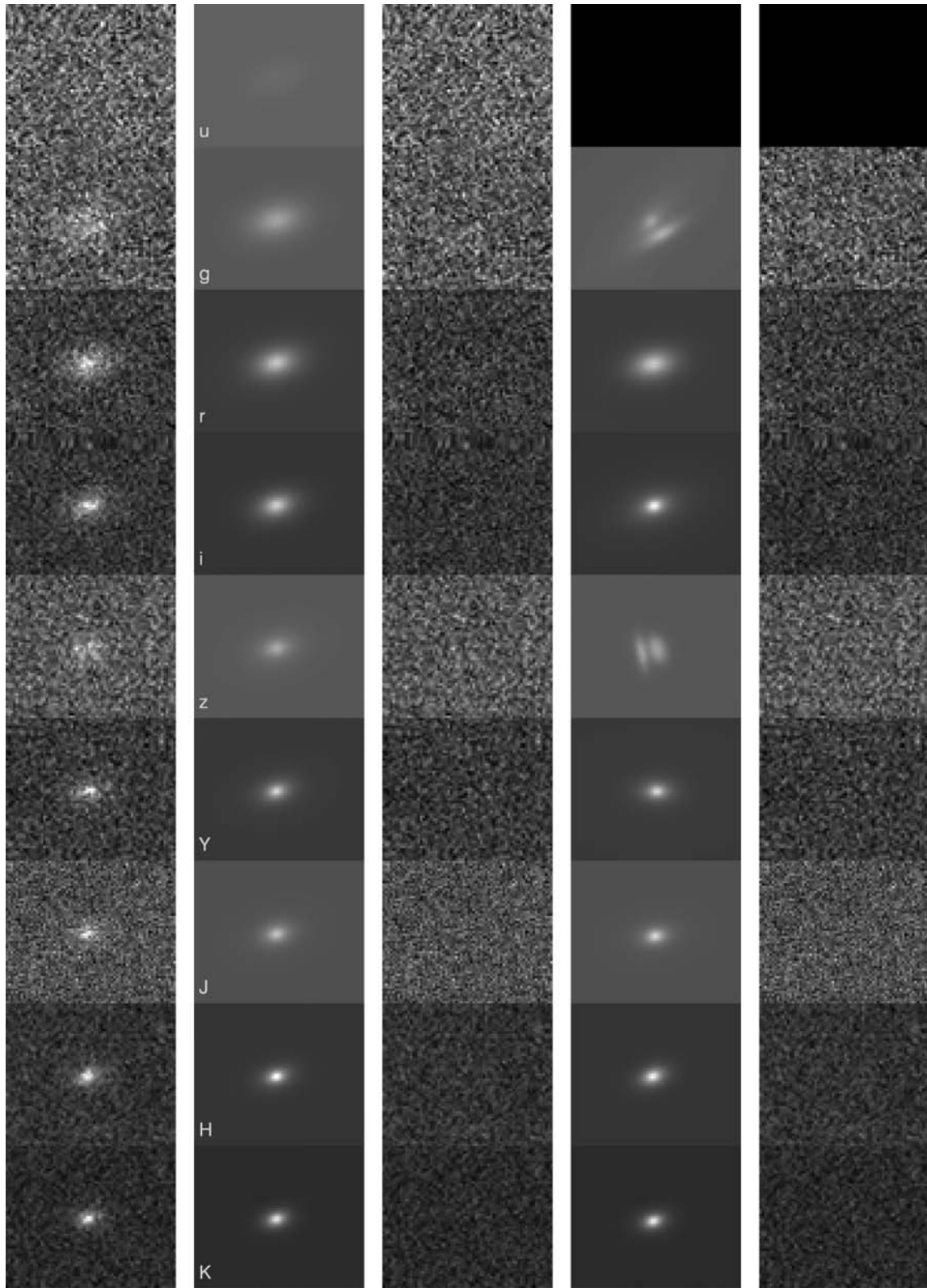
Figure A3. Example real object, similar to Fig. A1: This is a very interesting object, because it becomes immediately apparent why some of the single-band fits failed. In both *g* band and *i* band, the object is split up into two objects that are fit.
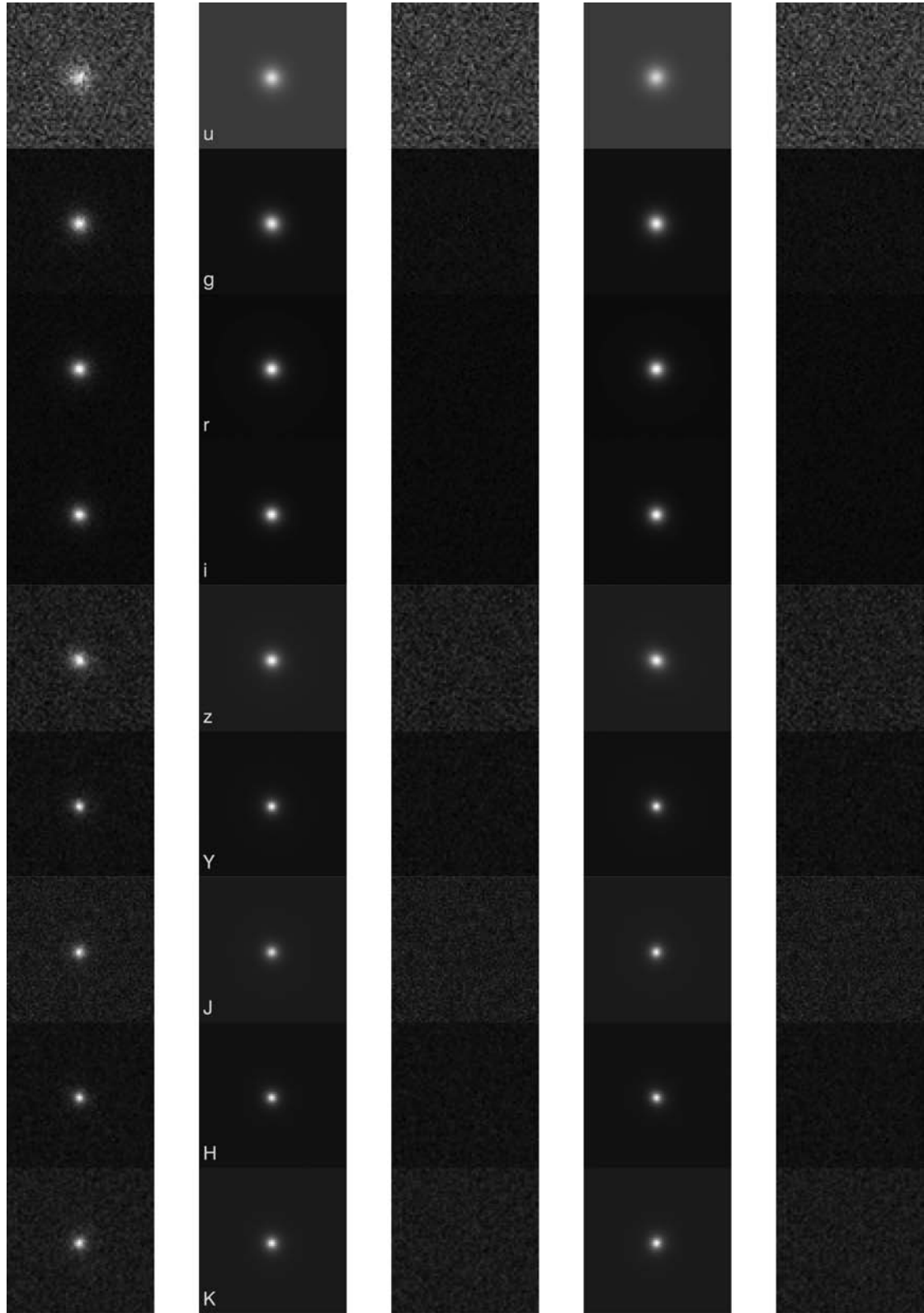
Figure A4. Example simulated object. This object failed to fit in some of the single-band fits. Whereas in the *u*-band data, it was missed in the detection procedure, in both *z* and *J* band, the fit crashed, returning no valid result. Thanks to the multiband detection that is used for the multiband fitting, we can recover parameters for all bands, e.g. creating a complete broad-band SED.
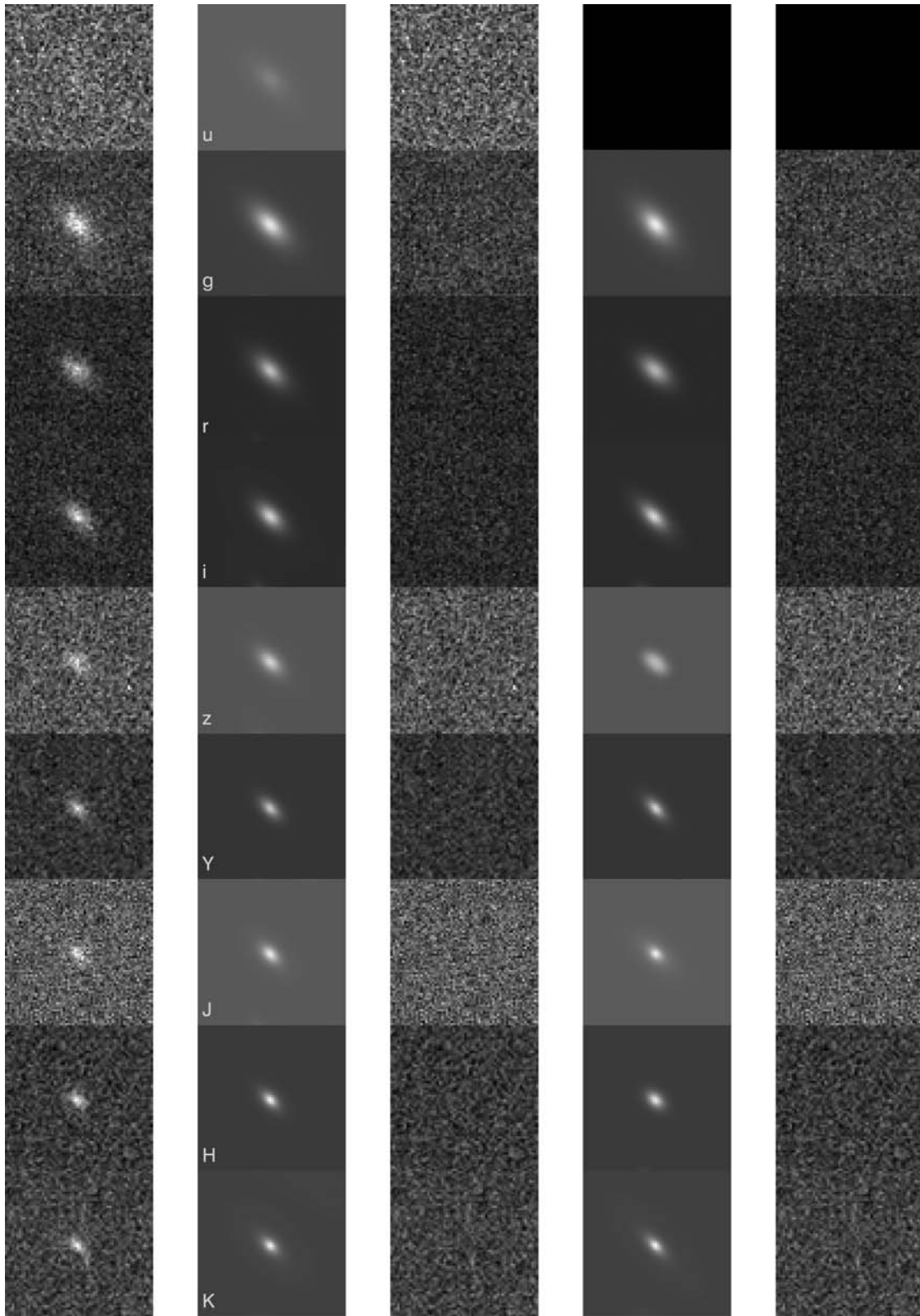
Figure A5. Example simulated object. This object is generally well fitted by both single- and multiband fitting. Only the single-band fitted on the *u*-band image did not return a result, most likely because the object was not detected in the *u*-band image.
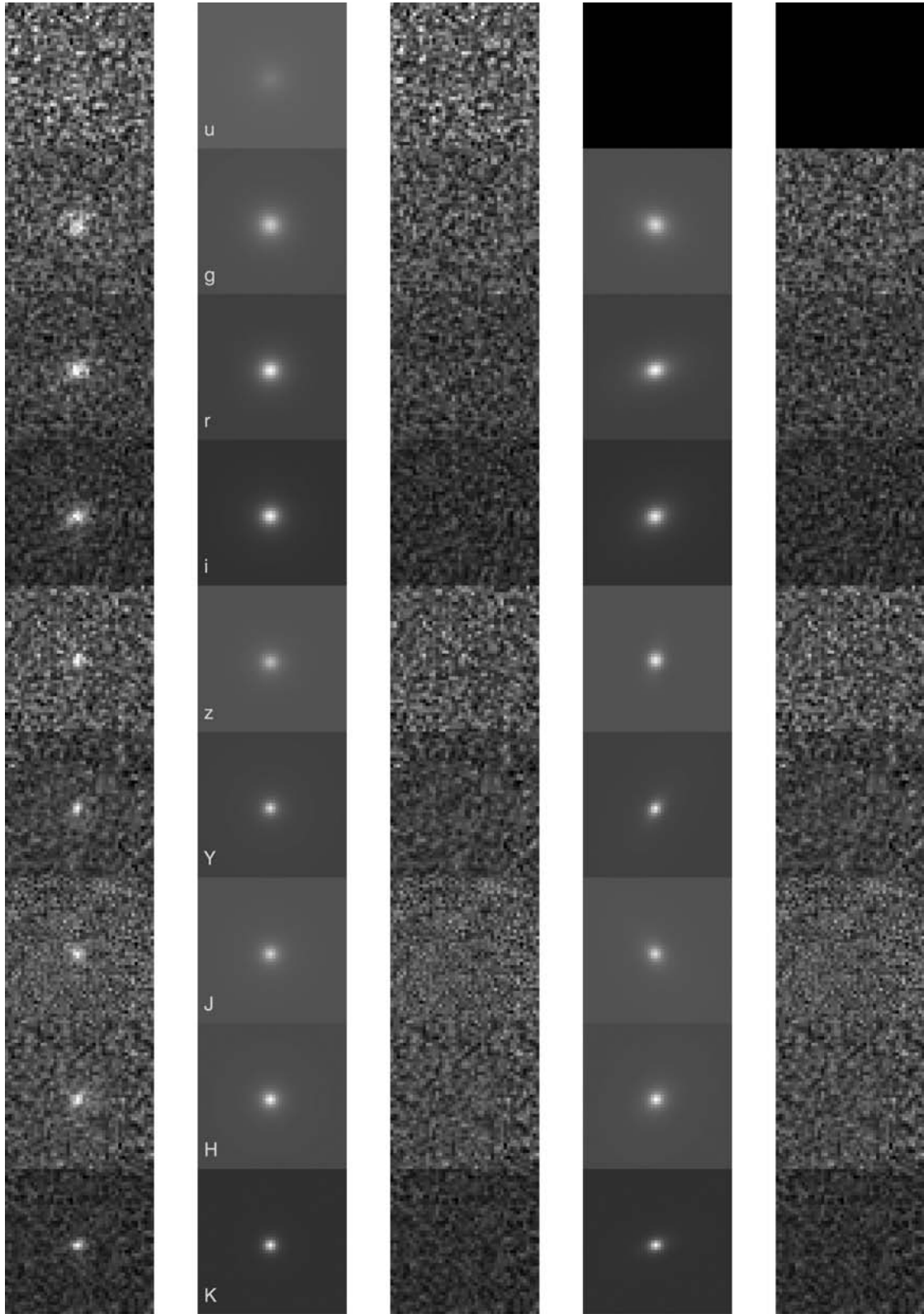
Figure A6. Example simulated object. From left to right: input image, model and residual multiband fit, image, model and residual single-band fit. The black images in the case of single-band fitting indicate where no GALFITM results exist (while ignoring constraints and cleaning of the catalogue).
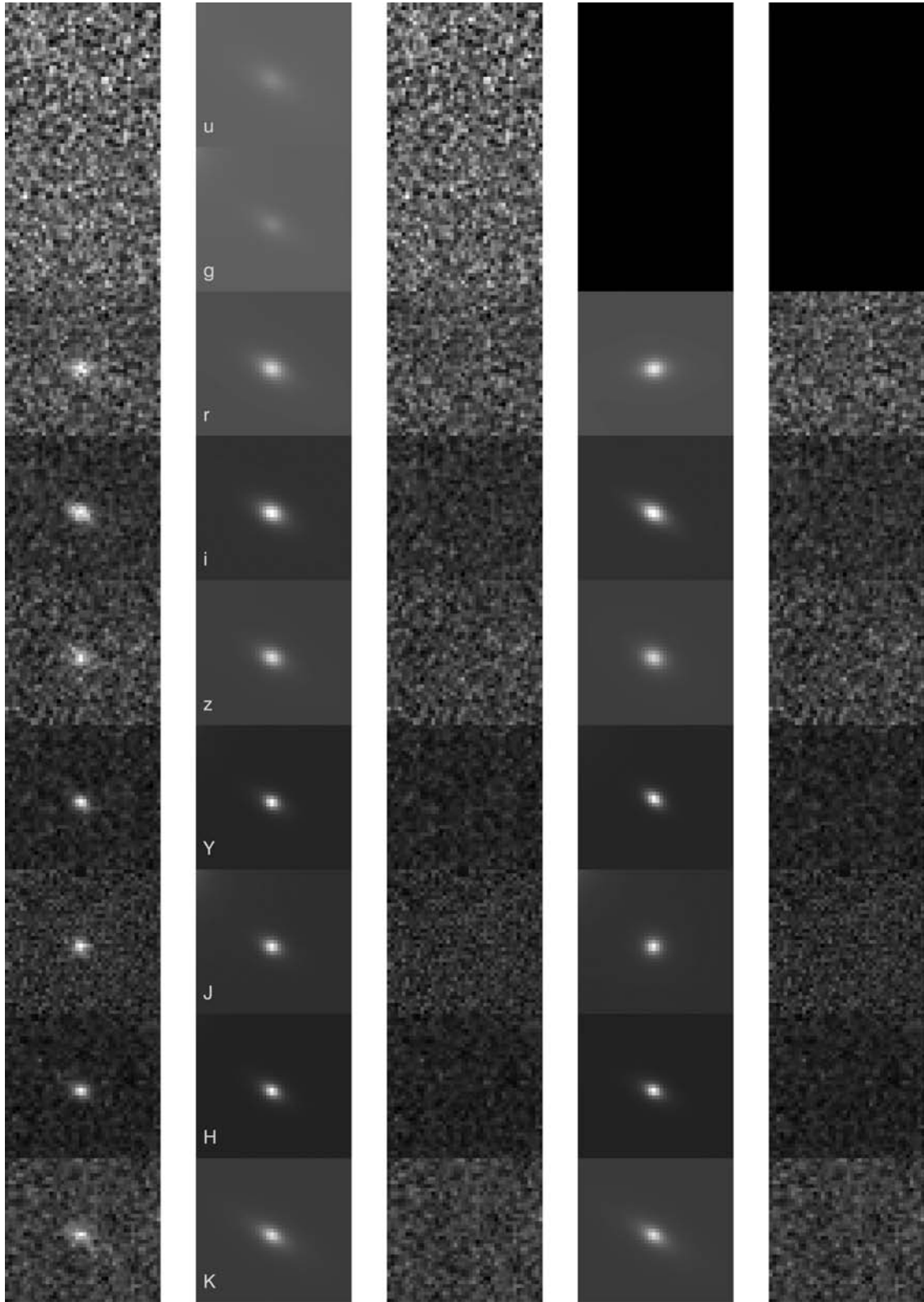
Figure A7. This is an extreme simulated object. It can really only be seen in *Y*- and *J*-band data, but thanks to the multiband capabilities, we can recover a full SED and parameter in all bands on this galaxy. In comparison, single-band fitting only returns one value in the *J*-band fit. Please keep in mind that all examples in this Appendix ignore the cleaning of the catalogue, e.g. showing this example does not mean that this objects would end up in the science catalogue.

This paper has been typeset from a TEX/LATEX file prepared by the author.